Deeply virtual Compton scattering studies at Jefferson Lab

F. Sabatié

CEA Saclay, Irfu/SPhN

Habilitation à Diriger les Recherches

Spécialité : Constituants Elémentaires

Université Blaise Pascal

Soutenance prévue le 2 Novembre 2010 devant le jury composé de :

Dr. Hélène Fonvieille
Dr. Serge Kox
Dr. Jacques Martino
Dr. Bernard Michel (rapporteur)
Dr. Bernard Pire (rapporteur)
Pr. Paul Stoler (rapporteur)

Contents

I. INTRODUCTION

My scientific career started with my Ph.D. which I defended in September 1998 at Saclay. The subject was the study of the nucleon spin structure functions measured in the E154 and E155 experiments. Those two experiments took place at the End Station A of SLAC (Stanford Linear Accelerator Center) at Stanford (CA) USA, where the quest for the understanding of the partonic structure of the nucleon started, with the Nobel experiment by Friedman, Kendall and Taylor [1]. The main goal of E154 and E155 was to measure the spin structure functions of the neutron, proton and deuteron by deep inelastic scattering (DIS) of electrons up to 50 GeV on polarized gaseous or solid targets. By measuring double spin asymmetries of counting rates, one can extract structure functions, from which polarized parton densities can be obtained through a Quantum Chromodynamics (QCD) analysis. A remarkable result is the determination of the spin carried by quarks in the nucleon, which only amounts to about 30% [2]. This rather low and thus unexpected value motivated the next generation of such experiments, trying to solve the spin crisis studying the gluon content of the nucleon (COMPASS, HERMES).

After my thesis in 1998, I did my national civil duty for two years as a post-doctoral fellow at Old Dominion University (VA) USA working at the Jefferson Laboratory on two closely related topics: Real Compton Scattering and Deeply Virtual Compton Scattering. I first helped putting together the Real Compton Scattering (RCS) experiment in Hall A which followed a novel idea from Radyushkin and others [3, 4] that for RCS at wide angles, a factorization scheme allows one to separate a hard perturbative kernel from a soft contribution related to the structure of the nucleon, the subject of our interest. Then, at the end of 1999, I had the opportunity to co-write the very first proposal to measure Deeply Virtual Compton Scattering (DVCS) - $\gamma^* p \to \gamma p$ - in the Hall A of Jefferson Lab. In the hard scattering limit, this process factorizes as well and allows one to study the structure of the nucleon in a very original way, as we will see later on. The proposal was approved with A rating by the Jefferson Lab PAC in 2000 for 600 hours of running time, and the corresponding experiment E00-110 ran in 2004 after a few years of detector and electronics developments.

I was hired at the CEA Saclay DAPNIA/SPhN in the fall of 2000, right after my national civil duty. This staff position corresponded to my interests: the study of hard exclusive

reactions at Jefferson Lab. The first programmed experiment was E1-6 in Hall B, planning to measure the deep electroproduction of ρ^0 and ω vector mesons among other channels, which ran in 2001-2002.

Let us go back to DVCS and why it is a particularily interesting process: barely more than ten years ago, a unifying concept for the description of the nucleon structure was introduced, now commonly known as Generalized Parton Distribution (GPD)[5–9]. These functions contain the usual form factors and parton distributions, but in addition they include correlations between states of different longitudinal and transverse momenta. GPDs can therefore give three-dimensional pictures of the nucleon, providing information such as the transverse spatial distribution as a function of the longitudinal momentum fraction of the quarks. With a complete knowledge of these functions, it is possible to obtain for instance, the high and low-momentum components of the nucleon for different flavors. The holy grail of this type of measurements is to provide enough data to determine the total angular momentum carried by quarks through Ji's sum rule [7]. Deeply Virtual Compton Scattering (DVCS) is the simplest and therefore cleanest process which can be described in terms of GPDs. It is the first reaction which allowed unambiguous extraction of GPDs from data and provided the cornerstone of their exploration at Jefferson Lab.

Four dedicated DVCS experiments have taken data at Jefferson Lab since the first theoretical developments: the Hall A E00-110 experiment I previously mentioned, measured helicity dependent cross sections and provided the best check so far of the Bjorken-type scaling which is expected of DVCS in the factorization regime [10]. As we will see in this document, one can now say with a fair degree of confidence that DVCS measurements at Jefferson Lab energies are indeed relevant to the investigation of the GPDs in the valence region. This experiment was followed in Hall A by a neutron DVCS experiment E03-106, sensitive to different GPDs [11]. The Hall B E01-113 experiment took data 6 months later, and is currently in the final stages of the analysis [12]. The main goal of that experiment was to perform Beam Spin Asymmetry measurements in a large kinematic domain, scanning this observable as a function of x_B, t and Q^2. A secondary goal, which is still ongoing, is to obtain cross sections in the same kinematic region. Finally, the polarized target version of the Hall B experiment, E05-114 has taken data in 2010 [13]. This particular DVCS experiment is more sensitive to the so-called "polarized" GPD.

In addition to these experiments which took data on DVCS, I took responsabilities in writ-

ing two proposals. The first one is E08-021, a 6 GeV proposal to measure DVCS on a transversely polarized target, which is more sensitive to the (light-cone) helicity-flip GPD [14]. The second one is the proposal to redo the unpolarized and longitudinally polarized DVCS experiments of Hall B after the Jefferson Lab 12 GeV upgrade, with better accuracy and larger kinematical coverage [15].

This document will try and summarize the work done in about 10 years on the three 6 GeV DVCS experiments and two proposals I worked and had responsabilities on, after a brief theoretical introduction, mostly to set the notations and concepts used later on. I will then try and give insights on the questions people usually ask in experimental talks about Generalized Parton Distributions : what did we really learn about DVCS and GPDs from this first set of experiments at Jefferson Lab? What do we need to do to perform better experiments in the future? I will then conclude and describe the new directions of Generalized Parton Distribution studies I plan to work on in the next few years.

Finally, I would like to point out that all this work was done in collaboration with many experimental and theory colleagues and could not have been possible without them. My many thanks to all of them, with a special note to my colleagues from France.

II. THEORY AND MOTIVATION

A. Brief overview of Generalized Parton Distributions

Barely more than 10 years ago, Mueller, Ji, Radyushkin and others[5–9, 16] showed that the DVCS reaction $\gamma^* p \to \gamma p$ can, in the Bjorken limit, be factorized into a hard scattering kernel and a non-perturbative part, containing information about the electromagnetic structure of the nucleon: the Generalized Parton Distributions. This factorization of the DVCS reaction is represented in Fig.1, where the virtual photon scatters on a single quark, which almost instantly re-emits a real photon. The quark is then inserted back into the nucleon, which is kept intact. In kinematical terms, this factorization is valid when the virtuality of the incoming photon is large ($Q^2 = -q^2$, with q the virtual photon 4-vector, defines the scale of the probe) but the transfer to the nucleon small compared to this scale ($-t << Q^2$). The soft (quark) structure of the nucleon is parametrized at twist-2 level by four chiral-even GPDs: E, H, $\widetilde{E}$ and $\widetilde{H}$.

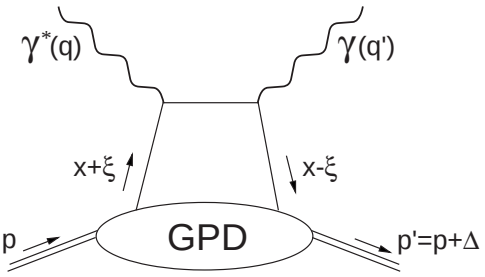

FIG. 1: Handbag diagram to the DVCS process, in the so-called DGLAP region corresponding to $\xi < x < 1$. See text for definition of variables.

All four GPDs depend on 4 variables: x, ξ, t and the hard scale Q^2. x characterizes the average light-cone momentum fraction of the struck quark in the loop (not directly accessible experimentally). ξ is the longitudinal momentum fraction of the transfer to the proton $\Delta = p - p'$ (where p and p' are the initial and recoil proton 4-vectors). It reduces to $\xi = x_B/(2 - x_B)$ in the Bjorken limit of infinite Q^2, with x_B the usual DIS variable defined as $x_B = Q^2/(2p \cdot q)$. Finally, $t = \Delta^2$ is the standard Mandelstam variable representing the momentum transfer between the virtual and real photons (or between the target and the recoil proton).

The scale evolution of the GPDs (Q^2-dependence) has been worked out to next-to-leading order of α_S and beyond [17, 18]. The Fourier transform of GPDs with respect to $\vec{\Delta}_T$ (the transverse component of Δ) gives access to the (transverse) spatial distribution of partons, as a function of x as we will detail later on.

In the forward direction defined by $\xi = t = 0$, the GPDs H and $\widetilde{H}$ reduce to the usual parton distributions $q(x)$ and $\Delta q(x)$:

$$H^q(x, \xi = 0, t = 0) \; = \; q(x)\,, \tag{1}$$

$$\widetilde{H}^q(x, \xi = 0, t = 0) \; = \; \Delta q(x)\,, \tag{2}$$

where q stands for the quark flavor. The first moments of the GPDs and the elastic form factors are related by the following relations:

$$\int_{-1}^{+1} dx H^q(x, \xi, t) \; = \; F_1^q(t)\,, \qquad \int_{-1}^{+1} dx E^q(x, \xi, t) = F_2^q(t)\,, \tag{3}$$

$$\int_{-1}^{+1} dx \widetilde{H}^q(x, \xi, t) \; = \; g_A^q(t)\,, \qquad \int_{-1}^{+1} dx \widetilde{E}^q(x, \xi, t) = h_A^q(t)\,, \tag{4}$$

where F_1^q and F_2^q are the Dirac and Pauli form factors, g_A^q is the axial form factor and h_A^q is

the induced pseudoscalar form factor. Note that the ξ dependence drops out in the integrals.

The second moment of the GPDs is relevant to the nucleon spin structure. It was shown in Ref. [7] that there exists a gauge-invariant decomposition of the nucleon spin:

$$\frac{1}{2} = J_q + J_g \,, \tag{5}$$

where J_q and J_g are respectively the total quark and gluon angular momentum contributions to the nucleon spin. J_q can be decomposed in a spin part $\Delta\Sigma$ and an orbital momentum part L_q as follows:

$$J_q = \frac{1}{2}\Delta\Sigma + L_q \,. \tag{6}$$

The second moment of the GPDs and the total angular momentum carried by quarks are related via Ji's sum rule:

$$\sum_q \frac{1}{2}\int_{-1}^{+1} dx\, x[H^q(x,\xi,t=0) + E^q(x,\xi,t=0)] = J_q \,. \tag{7}$$

Since $\Delta\Sigma$ is constrained in DIS experiments, if one makes enough measurements to extract the second moments of the GPDs, the sum rule will determine the quark orbital momentum contribution to the nucleon spin.

B. DVCS observables to access GPDs

The photon electroproduction $ep \to ep\gamma$ can either occur by radiation along one of the electron lines (Bethe-Heitler) or by emission of a real photon by the nucleon (DVCS) as shown on Figure 2. The total cross section as given by [19] reads:

$$\frac{d\sigma^{ep\to ep\gamma}}{dx_B dy d\Delta^2 d\phi} = \frac{\alpha^3 x_B y}{16\pi^2 Q^2\sqrt{1+\epsilon^2}} \left|\frac{\mathcal{T}}{e^3}\right|^2 \,, \tag{8}$$

where $\epsilon = 2x_B M/Q$, y is the fraction of the electron energy lost in the nucleon rest frame and the ϕ is the angle between the leptonic plane (e,e') and the photonic plane (γ^*,γ) as shown on Figure 3.

The total amplitude $\mathcal{T}$ is the superposition of the BH and DVCS amplitudes:

$$|\mathcal{T}|^2 \;=\; |\mathcal{T}_{BH}|^2 + |\mathcal{T}_{DVCS}|^2 + \mathcal{I} \tag{9}$$

$$\mathcal{I} \;=\; \mathcal{T}^*_{DVCS}\mathcal{T}_{BH} + \mathcal{T}_{DVCS}\mathcal{T}^*_{BH} \,, \tag{10}$$

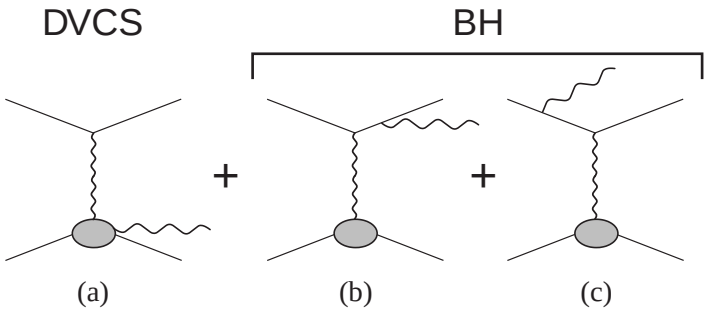

FIG. 2: Diagrams contributing to the electroproduction of a real photon. The DVCS process (a) is shown along with the interfering Bethe-Heitler diagrams (b) and (c).

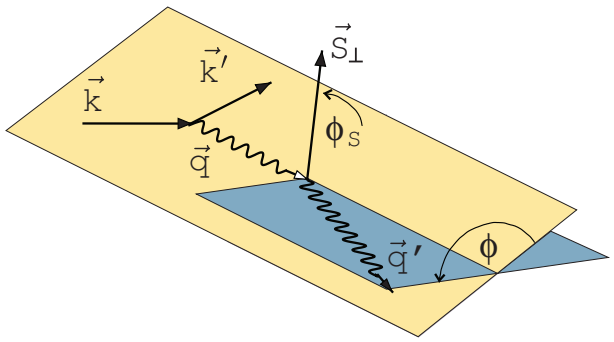

FIG. 3: Kinematics of the photon leptoproduction in the target rest frame, following the Trento notations. The incoming and outgoing leptons define the scattering plane, and the outgoing photon and recoil protons define the hadronic plane. In this reference system, the azimuthal angle of the scattered electron vanishes, while the azimuthal angle between the lepton and recoil proton planes is ϕ.

where $\mathcal{T}_{DVCS}$ and $\mathcal{T}_{BH}$ are the amplitudes for the DVCS and Bethe-Heitler processes, and $\mathcal{I}$ denotes the interference between these amplitudes. The individual contributions to the total $ep \to ep\gamma$ cross section can be written as (up to twist-3 contributions) [19]:

$$|\mathcal{T}_{BH}|^2 = \frac{\Gamma_{BH}(x_B, Q^2, t)}{\mathcal{P}_1(\phi)P_2(\phi)} \left\{ c_0^{BH} + \sum_{n=1}^{2} c_n^{BH} \cos(n\phi) + s_1^{BH} \sin\phi \right\} , \tag{11}$$

$$|\mathcal{T}_{DVCS}|^2 = \Gamma_{DVCS}(x_B, Q^2, t) \left\{ c_0^{DVCS} + \sum_{n=1}^{2} [c_n^{DVCS} \cos(n\phi) + s_n^{DVCS} \sin(n\phi)] \right\} , \tag{12}$$

$$\mathcal{I} = \frac{\Gamma_I(x_B, Q^2, t)}{\mathcal{P}_1(\phi)P_2(\phi)}] \left\{ c_0^I + \sum_{n=1}^{3} [c_n^I \cos(n\phi) + s_n^I \sin(n\phi)] \right\} , \tag{13}$$

where $\Gamma_{BH}, \Gamma_{DVCS}$ and Γ_I are known kinematical prefactors. $\mathcal{P}_1(\phi)$ and $\mathcal{P}_2(\phi)$ come from

the BH electron propagators and can be written as:

$$Q^2\mathcal{P}_1 \;=\; (k-q')^2 = Q^2 + 2k\cdot\Delta\,, \tag{14}$$

$$Q^2\mathcal{P}_2 \;=\; (k-\Delta)^2 = -2k\cdot\Delta + \Delta^2\,. \tag{15}$$

Note that in Eq.11-13, all $\sin(n\phi)$ coefficients depend on the beam helicity λ (they disappear in the unpolarized cross section). It is also worth mentioning that these equations are the result of some approximations, also known as the "BMK" approach, and some hot-fixes are available for refined analysis [20, 21].

Using either a polarized beam or a longitudinally polarized target, two separate quantities can be extracted: the **difference of cross section** for opposite beam helicities or opposite target spin, and the **total cross section**, which can be written respectively as:

$$d\sigma^{\rightarrow} - d\sigma^{\leftarrow} \;=\; 2\cdot\mathcal{T}_{BH}\cdot Im(\mathcal{T}_{DVCS}) + \left[|\mathcal{T}^{\rightarrow}_{DVCS}|^2 - |\mathcal{T}^{\leftarrow}_{DVCS}|^2\right]\,, \tag{16}$$

$$d\sigma^{\rightarrow} + d\sigma^{\leftarrow} \;=\; |T_{BH}|^2 + 2\cdot\mathcal{T}_{BH}\cdot Re(\mathcal{T}_{DVCS}) + |T_{DVCS}|^2\,, \tag{17}$$

where the arrows correspond to either the beam helicity (unpolarized target) or the target spin (unpolarized beam, longitudinally polarized target). At low energy, $|T_{DVCS}|^2$ is predicted to be smaller than other contributions, especially in the cross section difference. In the total cross section however, this term may be sizable at small y values. The data collected so far do not have sufficient statistical accuracy to resolve slight differences in the form of the angular distribution of the DVCS-BH interference and $|T_{DVCS}|^2$ terms. Therefore, we do not keep the $|T_{DVCS}|^2$ term in our discussion. On the other hand, it may be possible to make estimates of the relative magnitude of the $|T_{DVCS}|^2$ term using future accurate data [22]. Neglecting the $|T_{DVCS}|^2$ term, the previous equations now simplify to:

$$d\sigma^{\rightarrow} - d\sigma^{\leftarrow} \;=\; 2\cdot\mathcal{T}_{BH}\cdot Im(\mathcal{T}_{DVCS})\,, \tag{18}$$

$$d\sigma^{\rightarrow} + d\sigma^{\leftarrow} \;=\; |T_{BH}|^2 + 2\cdot\mathcal{T}_{BH}\cdot Re(\mathcal{T}_{DVCS})\,. \tag{19}$$

As we will detail further, depending on whether the beam helicity or target spin is flipped, different GPD contributions enter the cross section difference. From these two natural observables, one can write asymmetries which are experimentally easier to determine than cross sections:

$$A = \frac{d\sigma^{\leftarrow} - d\sigma^{\rightarrow}}{d\sigma^{\leftarrow} + d\sigma^{\rightarrow}} \simeq \Gamma_A(x_B, Q^2, t)\frac{s_1^I\sin\phi + s_2^I\sin(2\phi)}{\kappa c_0^{BH} + c_0^I + (\kappa c_1^{BH} + c_1^I)\cos\phi}\,, \tag{20}$$

where Γ_A and κ are known kinematical prefactors which do not depend on ϕ. The twist-3 contributions have been neglected except in the numerator. If one further neglects higher order harmonics suppressed by $\sqrt{-t}/Q$ or more, we are left with:

$$A \simeq \frac{\Gamma_A}{\kappa} \frac{s_1^I}{c_0^{BH}} \sin\phi\,, \tag{21}$$

where c_0^{BH} is again fully calculable, and s_1^I contains twist-2 GPD information. One should be careful with approximations leading to this expression. When trying to estimate GPDs at the 20% accuracy level or higher, it is reasonable to proceed with these simplified equations at reasonably high Q^2 and low t. However, with the goal of providing accurate GPD measurement at 5% accuracy level or lower, one should not neglect all the other contributions in the final analysis. Moreover (and again), the BMK approximation is known to not hold at low Q^2 and/or high x_B as shown in [20].

At this point, it is natural to introduce the Compton Form Factors (CFF) $\mathcal{H}$, $\widetilde{\mathcal{H}}$, $\mathcal{E}$ and $\widetilde{\mathcal{E}}$ which are the complex counterparts of GPDs and directly relate to the DVCS amplitude at Leading Order of α_S [19]:

$$\begin{aligned}\mathcal{H}(\xi,t) = \sum_q e_q^2 \Bigg\{ & i\pi \left[H^q(\xi,\xi,t) - H^q(-\xi,\xi,t)\right] \\ & + \mathcal{P}\int_{-1}^{+1} dx \left[\frac{1}{\xi - x} - \frac{1}{\xi + x}\right] H^q(x,\xi,t)\Bigg\}\,,\end{aligned} \tag{22}$$

where the sum is made over quark flavors q, e_q being their charge in units of e. Similar expressions can be written for all CFFs/GPDs. In the unpolarized target case, the coefficient s_1^I can now be written as a function of the CFF $\mathcal{H}$, $\widetilde{\mathcal{H}}$ and $\mathcal{E}$:

$$s_{1,unp}^I = y(2-y)\mathrm{Im}(\mathcal{C}_{unp}^I) = y(2-y)\mathrm{Im}\left\{F_1\mathcal{H} + \frac{x_B}{2-x_B}(F_1+F_2)\widetilde{\mathcal{H}} - \frac{t}{4M^2}F_2\mathcal{E}\right\}\,, \tag{23}$$

where the *unp* subscript refers to an unpolarized target and the coefficient $\mathcal{C}_{unp}^I$ is simply $s_{1,unp}^I$ without the kinematical prefactor. In the longitudinally polarized (LP) target case, $s_{1,LP}^I$ can be written as a function of the same CFFs:

$$\begin{aligned}s_{1,LP}^I = (2-2y+y^2)\mathrm{Im}(\mathcal{C}_{LP}^I) \;=\; & (2-2y+y^2)\mathrm{Im}\left\{F_1\widetilde{\mathcal{H}} + \frac{x_B}{2-x_B}(F_1+F_2)\left(\mathcal{H} + \frac{x_B}{2}\mathcal{E}\right)\right. \\ & \left. -\frac{x_B}{2-x_B}\left(\frac{x_B}{2}F_1 + \frac{t}{4M^2}F_2\right)\widetilde{\mathcal{E}}\right\}\,.\end{aligned} \tag{24}$$

Since $s^I_{1,unp}$ and $s^I_{1,LP}$ both depend on the imaginary part of the CFFs, they directly depend on linear combinations of 3 GPDs at the particular kinematical lines $x = \pm\xi$. On the contrary, the real part of the CFFs, and therefore this principal part integral over x of GPDs can only be accessed in a clean way through beam charge asymmetry. The real part of the CFFs also enters the total cross section but their disentanglement is made very complicated by the presence of $\mathcal{T}^2_{DVCS}$ terms which cannot be separated easily and are of the same order of magnitude in the region around $\phi = 180°$ for JLab's typical kinematics. Note that all these considerations are only valid at Leading Order of α_S. Next-to-Leading-Order analysis of experimental data in the valence quark region has not been attempted yet but may be required once the accuracy improves.

The main contribution to $s^I_{1,unp}$ is $F_1\mathcal{H}$ and again, this approximation can be used to give orders of magnitude estimates of $\mathcal{H}$ from data but not to extract the GPD accurately. The main contributions to $s^I_{1,LP}$ come from both $\mathcal{H}$ and $\widetilde{\mathcal{H}}$, whereas the $\widetilde{\mathcal{E}}$ contribution is suppressed.

It becomes obvious that in order to extract GPDs with good accuracy, an extensive program covering a large kinematical domain, with high precision data in both asymmetries and cross section measurements is absolutely necessary. The extraction of GPDs will be done in the same manner as Parton Distribution Functions are extracted from structure function measurements, by means of a global fit of data using adequate GPD parametrizations. This subject is under scrutiny by many people but still requires some work [23–25], we will do a short review of it in section V.

C. Impact parameter interpretation

Generalized Parton Distributions H, $\widetilde{H}$ and E have a physical interpretation in the limiting case $\xi = 0$ and $t \neq 0$ where they can be seen as probability densities since the parton carries the same longitudinal momentum fraction x in the initial and final states and hence the momentum transfer t is purely transverse, *i.e.* $t = -\Delta_\perp$ [26]. Of course, this situation cannot be achieved in DVCS at finite energies because it takes at least some longitudinal momentum transfer in order to convert a virtual photon into a real photon, but it is still relevant as a limiting case. Note that this framework was described early on in a more general perspective by Ralston and Pire [27] where the analogy with holographic

imaging techniques has been pointed out. It was then developped formally by Burkardt, Diehl and others [28–30].

Restricting ourselves to the GPDs H and $\widetilde{H}$ in the limit $\xi = 0$ and $t \neq 0$,

$$H(x,t) \equiv H(x,\xi=0,t) \qquad \text{and} \qquad \widetilde{H}(x,t) \equiv \widetilde{H}(x,\xi=0,t) \tag{25}$$

have a simple physical interpretation as the Fourier transform of impact parameter dependent parton distribution with respect to the impact parameter, in other words :

$$H(x,-\vec{\Delta}_\perp^2) = \int d^2b_\perp q(x,\vec{b}_\perp) e^{-i\vec{b}_\perp\cdot\vec{\Delta}_\perp} \tag{26}$$

$$\widetilde{H}(x,-\vec{\Delta}_\perp^2) = \int d^2b_\perp \Delta q(x,\vec{b}_\perp) e^{-i\vec{b}_\perp\cdot\vec{\Delta}_\perp} \tag{27}$$

where the impact parameter or transverse distance $b \equiv |\vec{b}_\perp|$ is defined from the center of transverse momentum of the nucleon rather than its center of mass. These impact parameter dependent parton distributions $q(x,\vec{b}_\perp)$ provide a set of tomographic images of the nucleon, as illustrated by the cartoon on Figure 4.

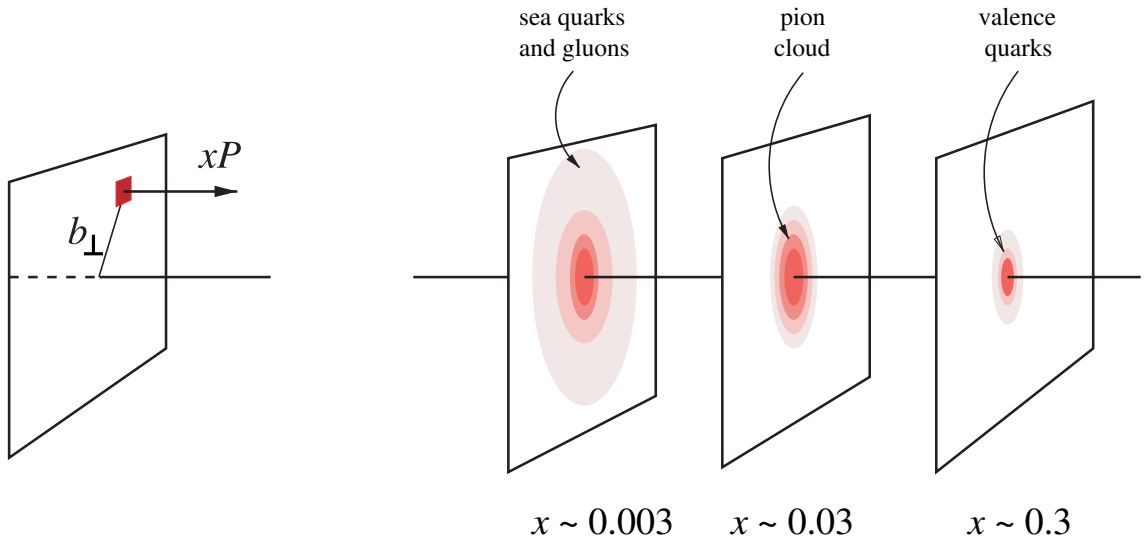

FIG. 4: The Fourier transform of the GPD describes the simultaneous distribution of quarks with respect to longitudinal momentum, xP , and transverse position, $b_\perp$, in the infinite momentum frame. It produces a (1+2) dimensional tomographic image of the quark structure of the nucleon.

Quark density distributions in the transverse plane for different combinations of transverse spin of proton and quark, as predicted by recent GPD lattice calculations [31], are shown

on Figure 5. They demonstrate how the knowledge of GPDs or moments of GPDs can lead to tomographic images of the nucleon through a refined analysis.

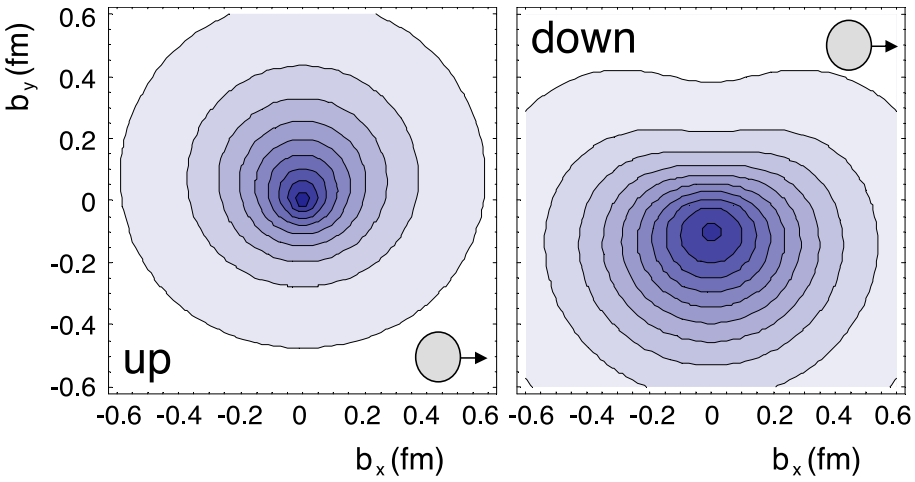

FIG. 5: Density distributions of unpolarized u and d quarks in the transversely polarized nucleon defined by the GPD E, from [31].

D. GPD models

A necessary step towards Generalized Parton Distributions extraction from data consists in using models with parameters to be fit to data. Indeed, GPDs are complicated functions of three variables in addition to Q^2. Moreover, the variable x is usually not accessible except for instance when accessing the imaginary part of Compton Form Factors, sensitive to the GPD at the particular point $x = \xi$.

There exists a number of models to calculate GPDs, among which I would call "nucleon description" models, from the simplest such as the MIT bag [16] or more complicated ones such as quark-soliton chiral models [32, 33] among others. As it turns out, these constrained models are relatively unsuccessful describing both the low and high energy DVCS data, which is not unexpected. They have relatively few degrees of freedom that can be fit to data and GPDs being a fairly general object, describing the nucleon with such general approaches through GPDs is a rather ambitious task. Another completely different class of models are the "GPD description" type of models. Instead of trying to describe the nucleon and then compute the GPDs within this description, they use the approach of trying to parametrize GPDs from basic principles and their constraints directly. There are two important classes

of such models which we will briefly discuss in the following : Double Distribution based models and Dual models[1]. They both have their advantages and disadvantages but clearly do a much better job describing the available DVCS data.

1. Double Distribution models

The first available parametrization of GPDs was achieved using Double Distributions supplemented by a so-called D-term. In this parametrization, one of the strongest contraints on GPDs is trivially achieved : the polynomiality of the Mellin moments of the GPDs, a consequence of Lorentz invariance, means that one should be able to write the Nth Mellin moment of the GPDs H and E as follows :

$$\int_{-1}^{1} x^N H(x,\xi) \;=\; h_0^{(N)} + \xi^2 h_2^{(N)} + ... + \xi^{N+1} h_{N+1}^{(N)}\,, \tag{28}$$

$$\int_{-1}^{1} x^N E(x,\xi) \;=\; e_0^{(N)} + \xi^2 e_2^{(N)} + ... + \xi^{N+1} e_{N+1}^{(N)}\,. \tag{29}$$

Note that the same polynomiality condition also applies to GPDs $\widetilde{H}$ and $\widetilde{E}$ but for simplicity, we only wish to describe the Double Distribution parametrization for H and E. The nucleon being spin 1/2, the highest power coefficient of H and E are equal in value with opposite signs. This polynomiality condition strongly restricts the class of functions for H and E. As it turns out, a Double Distribution satisfies this constraint in an elegant fashion. The GPDs H and E are then obtained as a one-dimensional section of Double Distributions F and K :

$$H(x,\xi) \;=\; \int_{-1}^{1} d\beta \int_{-1+|\beta|}^{1-|\beta|} d\alpha\, \delta(x-\beta-\alpha\xi) F(\beta,\alpha)\,. \tag{30}$$

$$E(x,\xi) \;=\; \int_{-1}^{1} d\beta \int_{-1+|\beta|}^{1-|\beta|} d\alpha\, \delta(x-\beta-\alpha\xi) K(\beta,\alpha)\,. \tag{31}$$

Even though the GPDs H and E in these equations trivially satisfy the polynomiality condition of Eq. 29, they do so by imposing that the highest power coefficient for H and E are equal to zero, *i.e.* $h_{N+1}^{(N)} = e_{N+1}^{(N)} = 0$. This parametrization is therefore incomplete and requires the addition of an extra isoscalar term called the D-term, equal for H and E but of opposite sign and flavor independent. The full expression for H and E is now :

[1] Another more complicated class of models exists [25, 34, 35] and will be briefly discussed in section V. The authors have proven it is equivalent to the Dual representation.

$$H(x,\xi) = \int_{-1}^{1} d\beta \int_{-1+|\beta|}^{1-|\beta|} d\alpha \delta(x-\beta-\alpha\xi) F(\beta,\alpha) + \theta(1-x^2/\xi^2) D(\frac{x}{\xi}) \,. \quad (32)$$

$$E(x,\xi) = \int_{-1}^{1} d\beta \int_{-1+|\beta|}^{1-|\beta|} d\alpha \delta(x-\beta-\alpha\xi) K(\beta,\alpha) - \theta(1-x^2/\xi^2) D(\frac{x}{\xi}) \,. \quad (33)$$

For a parametrization of the Double Distributions, one usually follows Radyushkin's anzatz for the GPD H and writes :

$$F^q(\beta,\alpha) = h(\beta,\alpha) q(\beta) \,, \quad (34)$$

where $q(\beta)$ is the parton distribution function for the quark of flavor q and where $h(\beta,\alpha)$ is a profile function, usually chosen to be :

$$h(\beta,\alpha) = \frac{\Gamma(2b+2)}{2^{2b+1}\Gamma^2(b+1)} \frac{[(1-|\beta|)^2-\alpha^2]^b}{(1-|\beta|)^{2b+1}} \,. \quad (35)$$

where γ is the usual Gamma function. In this last equation, the parameter b characterizes how strong the ξ-dependence is in the GPD H^q. $b \to \infty$ corresponds to a ξ-independent ansatz. Typical values chosen by theorists are close to $b = 1$ for valence and sea quarks [36]. Note that these ansätze are not necessarily correct but practical for computation purposes.

We now turn to the t-dependence, which should be governed mainly by the sum rules of Eqs. 4, through which the first moments of the GPDs are related to the form factors. The simplest t-dependence of GPDs consists in a factorized form : the t-dependent GPD is just the product of the corresponding form factor times the parametrization we just described. For instance, assuming the GPD H for the s quark is zero, this parametrization would read:

$$H^u(x,\xi,t) = H^u(x,\xi) F_1^u(t)/2 \,, \quad (36)$$

$$H^d(x,\xi,t) = H^d(x,\xi) F_1^d(t) \,, \quad (37)$$

$$H^s(x,\xi,t) = 0 \,, \quad (38)$$

Where the $u(d)$ subscript for the Dirac form factor $F_1(t)$ corresponds to its $u(d)$ quark contribution. Such trivial t-dependences have been used in the past in order to make estimates, but clearly do not add any new information about GPDs. A more modern approach is inspired by the quark-soliton model which suggests a Regge-like behavior. More information can be found in the article describing the VGG parametrization [36], used by many

in the community. Figure 6 shows the GPD H for the u valence quarks (top) and total u quarks including sea (bottom) as calculated in [36].

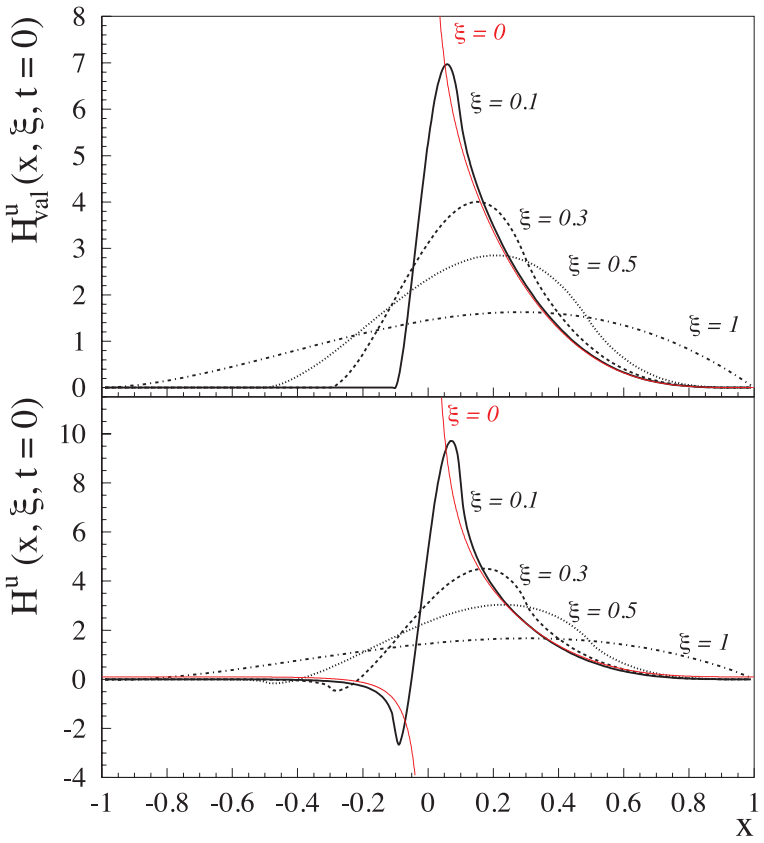

FIG. 6: GPD $H(x, \xi, t = 0)$ as a function of x for different values of ξ, evaluated for the u valence quarks (top) and total u quarks including sea (bottom) using the VGG model as described in [36].

2. *Dual models*

The dual model is based on the decomposition of GPDs in t-channel waves as explained in Ref. [37] and proceeds with a resumation of these partial waves into a series of two-variable functions (in contrast to the double distribution case, where one deals with a single three-variable function). In analogy to the magnetic and electric combinations of Form Factors, the t-channel partial waves are usually described by the combinations of GPDs:

$$H^{(E)} = H + E \qquad \text{and} \qquad H^{(M)} = H + \frac{t}{4M^2} E\,, \tag{39}$$

as suggested in Ref. [38]. In addition, the dual parametrization is introduced for the (charge) singlet and non-singlet combinations of $H^{(E,M)}$. The charge singlet combinations $H_+^{(E,M)}$

which enter DVCS are simply :

$$H_+^{(E,M)} = H^{(E,M)}(x,\xi,t) - H^{(E,M)}(-x,\xi,t)\,. \tag{40}$$

The partial wave decomposition of the electric singlet GPD $H_+^{(E)}(x,\xi,t)$ can be written as the following formal series :

$$H_+^{(E)} = 2\sum_{n=1,odd}^{\infty}\sum_{l=1,even}^{n+1} B_{nl}^E(t)\theta\left(1-\frac{x^2}{\xi^2}\right)\left(1-\frac{x^2}{\xi^2}\right)C_n^{3/2}\left(\frac{x}{\xi}\right)P_l\left(\frac{1}{\xi}\right)\,, \tag{41}$$

where l stands for an orbital momentum l exchange in the t-channel, $C_n^{3/2}$ are Gegenbauer polynomials and P_l are Legendre polynomials. $B_{nl}^E(t)$ is the so-called generalized electric form factor. The magnetic counterpart of Eq. 41 includes an additional factor $1/\xi$ and derivatives of the Legendre polynomial P_l'. The partial wave decomposition of GPDs turns out to be useful in order to write a parametrization of GPDs in terms of forward-like functions Q_k ($k = 0, 2, ...$) defined as the Mellin moments of the generalized form factors as follows :

$$B_{n\,n+1-k}(t) = \int_0^1 dx x^n Q_k(x,t)\,. \tag{42}$$

where k is always an even number. Practically speaking, the Q^2 evolution of this set of functions $Q_k(x,t)$ is governed by the usual singlet DGLAP equation. The lowest moment $Q_0(x,t=0)$ or $Q_0(x)$ for simplicity, is related to the usual (singlet) parton densities :

$$Q_0(x) = (q(x)+\bar{q}(x)) - \frac{x}{2}\int_x^1 \frac{dz}{z^2}(q(z)+\bar{q}(z))\,. \tag{43}$$

As far as the higher moments are concerned however, for instance $Q_2(x)$, their modeling is not uniquely determined as for $Q_0(x)$ and only their Mellin moments are constrained. Theorists usually choose a simple form for $Q_2(x)$, similarly to the forms chosen for standard PDFs when fitting structure function data. The so-called minimal dual model used by some [39] only retains the two first generating functions $Q_0(x)$ and $Q_2(x)$. A fully forward dual model (also called minimalist dual model) may also be used and only uses $Q_0(x)$: it has no free parameter once a set of PDF is chosen.

The DVCS amplitude at the photon level at Leading Order of α_S - which is essentially the Compton Form Factor - reads :

$$\mathcal{H}(\xi,t) = \sum_q e_q^2 \int_0^1 dx H_+^q(x,\xi,t)\left(\frac{1}{x-\xi+i\epsilon}+\frac{1}{x+\xi-i\epsilon}\right)\,, \tag{44}$$

where e_q is the flavor q quark electric charge. This amplitude is actually uniquely determined by the so-called GPD quintessence function $N(x)$ which is defined by the following infinite sum over the generating functions $Q_k(x)$ [40] :

$$N(x,t) = \sum_{k=0,even}^{\infty} x^k Q_k(x,t)\,. \tag{45}$$

One can now write the DVCS amplitude or CFF as follows :

$$\mathcal{H}(\xi,t) = -2\sum_q e_q^2 \int_0^1 \frac{dx}{x} \sum_{k=0,even}^{\infty} x^k Q_k(x,t) \left(\frac{1}{\sqrt{1-\frac{2x}{\xi}+x^2}} + \frac{1}{\sqrt{1+\frac{2x}{\xi}+x^2}} - 2\delta_{k0} \right), \tag{46}$$

where δ_{k0} is the Kronecker delta with $\delta_{k0} = 0$ if $k \neq 0$ and $\delta_{k0} = 1$ if $k = 0$. Using this equation, one can extract the imaginary and real parts of the DVCS amplitude or equivalently the CFF and evaluate the various related DVCS observables such as polarized or unpolarized cross sections or asymmetries. We will show how this type of model can be compared to DVCS data in section V.

III. DEEPLY VIRTUAL COMPTON SCATTERING EXPERIMENTS AT 6 GEV

The theoretical grounds for Generalized Parton Distributions and how to access them using Deeply Virtual Compton Scattering were set in 1998. Within two years, a lot of thoughts and work were put into imagining how to make such DVCS experiments in Jefferson Lab, with beam energy not higher than 6 GeV and the requirement to be fully exclusive, *i.e.* ensure that the electron, photon and proton were the only products of the reaction. This resulted in a dedicated proposal to Jefferson Lab PAC18 to measure DVCS on the proton in Hall A, which was conditionally approved, the condition being that it was proven that an electromagnetic calorimeter could sustain high singles rate and remain efficient and stable despite the resulting radiation damage. A short test run confirmed it was indeed doable and it took 4 years to put together the experimental equipment in order to make this state-of-the-art measurement. A proposal to measure DVCS on the neutron in Hall A using an augmented apparatus was accepted by PAC24 shortly after, the idea was to run the neutron experiment right after the proton one to limit installation time. In Hall B, the CLAS collaboration proposed to study DVCS through the measurement of beam spin asymmetries in a large kinematical domain, which was accepted by PAC20 of Jefferson Lab.

In the meantime, it was natural to use old electroproduction data to look for DVCS events and both the HERMES and the Jefferson Lab CLAS collaborations published interesting - though statistically limited - analysis.

In the following sections, we will first take a look at the Hall B non-dedicated data which first gave a hint that the handbag approximation was likely reasonable to describe DVCS at Jefferson Lab kinematics. We will then describe the dedicated DVCS experiments we performed at Jefferson Lab Halls A and B. Finally, I will describe the last 6 GeV proposal to study DVCS with a transversely polarized target in Hall B.

A. Jefferson Lab Hall B non-dedicated analysis

The data was taken from the CLAS/E1C experiment which ran in march 1999. The experiment measured the scattering of 4.25 GeV longitudinally polarized electrons off a 5 cm-long liquid hydrogen target. The data sample corresponds to an integrated luminosity of 1.4 fb^{-1}. The goal of the analysis was to extract the Beam Spin Asymmetry (BSA) in

the photon electroproduction reaction. The BSA is simply defined theoretically by the ratio of the difference of cross sections for opposite electron helicity to the total cross section. Experimentally, it is estimated using the following formula:

$$A = \frac{1}{P_{beam}} \frac{\frac{N^+}{Q^+} - \frac{N^-}{Q^-}}{\frac{N^+}{Q^+} + \frac{N^-}{Q^-}}\,, \tag{47}$$

where $N^{+(-)}$ and $Q^{+(-)}$ are respectively the number of $\vec{e}p \to ep\gamma$ events with positive (negative) helicity and the associated beam charge, and P_{beam} the beam polarization, on average 65% during this experiment.

For this experiment, since $< x_B >$=0.19 and $< Q^2 >$= 1.25 GeV^2, the virtual photon direction was on average 5° around the beam line. If one is only interested at low $|t|$ events, say < 0.5 GeV^2, the DVCS photon would be emitted most of the time at lower than 15°, *i.e.* out of the CLAS acceptance for neutral particles. Selecting true triple coincidence events was impossible due to low statistics. The only possibility was to select $ep \to epX$ events and use a missing mass method to pinpoint the missing photon.

However, this type of analysis is made extremely delicate in the kinematics of interest. The main physics background to $ep \to ep\gamma$ is $ep \to ep\pi^0$ with a subsequent asymmetric decay of the π^0 into two photons. If the low energy photon remains undetected (under threshold or outside of the acceptance), the resulting missing mass is fairly close to 0, resulting in a broadened photon peak rather than a separate peak, as shown on Figure 7. Moreover, the π^0 cross section is not expected much smaller than the photon one, this background cannot be neglected.

The idea is therefore to fit the observed peak at ∼0 missing mass with 2 Gaussian contributions for photon and π^0 plus a smooth polynomial background underneath, representing more complicated processes, typically with extra emitted pion(s). The location and width of the Gaussians were measured from pure photon and π^0 samples in specially selected kinematics. An example of such a fit is presented on Figure 8 for a typical bin. This fit was performed for each bin in the variable ϕ, integrated over the range Q^2 from 1 to 1.75 GeV^2 and $-t$ from 0.1 to 0.3 GeV^2. The asymmetry was computed using counts for γ events in the missing mass fit for each helicity, as written in Eq. 47. It is shown on Figure 9 as published in [41].

As explained in the first chapter, this result may be fitted by the functional form $\alpha \sin\phi + \beta \sin 2\phi$ omitting any ϕ dependence of the total cross section except the one induced

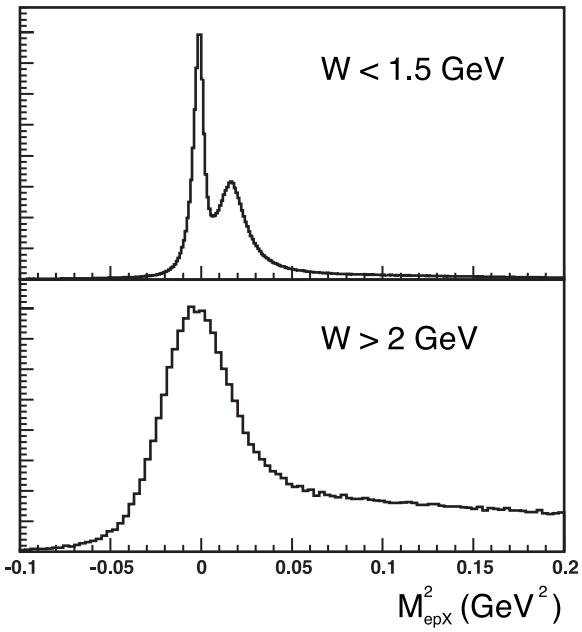

FIG. 7: Missing mass squared distributions for $ep \to epX$ events in CLAS for $W < 1.5$ GeV (top) and $W > 2$ GeV (bottom). The peaks for missing γ and π^0 are no longer separated at high W.

by the Bethe-Heitler electron propagators as written in Eq. 15, which cancels out if one only considers the interference and Bethe-Heitler contributions to the polarized cross sections. The result of the fit gives $\alpha = 0.202 \pm 0.041$ and $\beta = 0.024 \pm 0.030$. The vanishing β was the first hint, but certainly not a proof, that the handbag diagram may be the dominant contribution to DVCS even at Q^2 as low as 1.5 GeV^2 in this x_B region. The data are also compared with the VGG model [36] with different assumptions but no tuning of the parameters. This Double Distribution model tends to over-estimate the data by 20 to 30% in this observable.

These data along with similar results from HERMES confirmed that it was sensible to run dedicated experiments to measure Deeply Virtual Compton Scattering and possibly get information about Generalized Parton Distributions. The theoretical grounds for GPDs are rather strong and straightforward, however they assume that the factorization regime is reached in order to extract GPDs reliably. This factorization is essential to GPDs study especially at Jefferson Lab with moderate energy, it needs to be carefully checked.

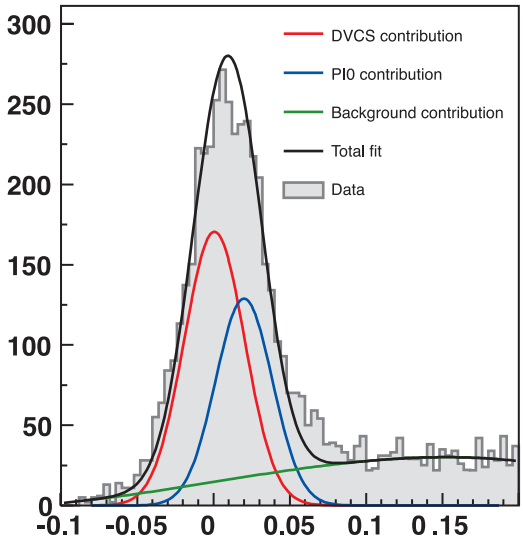

FIG. 8: Missing mass squared distribution of the (e, p, X) system, integrated in the range of ϕ from 70 to 110°. The black line is the fit to the sum of two Gaussians centered at the γ (red Gaussian) and π^0 (blue Gaussian) masses respectively plus a third order polynomial distribution (green curve).

B. Jefferson Lab Hall A experiment E00-110: DVCS on the proton

The E00-110 experiment was proposed in 2000 and actually ran in the fall of 2004 in the Hall A of Jefferson Lab. Its main purpose was to perform a test of the factorization in the DVCS process by performing a Q^2 scan at fixed x_B of the cross section difference for opposite electron helicities.

As mentioned before, DVCS experiments share the same difficulties wherever they are located:

- the DVCS cross section is small. This is a problem because the GPDs are buried as principal part integrals in the DVCS amplitude. However, as pointed out early in the theoretical developments [42], the fact that the DVCS and Bethe-Heitler processes share the same initial and final states and therefore interfere comes as a tremendous help : since the BH amplitude is large, purely real, and depends only on Form Factors, the DVCS amplitude is actually accessible in the interference term using polarization observables such as asymmetries or better yet, cross section differences. While the BH amplifies the DVCS amplitude, the photon electroproduction cross section is still small

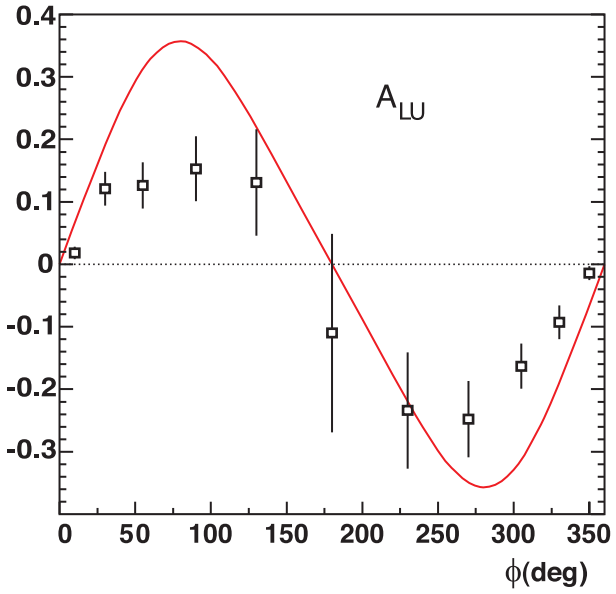

FIG. 9: ϕ dependence of the beam spin asymmetry A_{LU}. The curve is a Double Distribution model calculation according to Ref. [36].

and one either needs a high luminosity or high acceptance in order to yield statistically significant results.

- the factorization necessary to interpret observables in terms of GPDs requires high Q^2 and low-t. At low energy, this means that most of the interesting data will be forward in the lab reference frame. Moreover, in electron scattering, the forward region is dominated by Møller scattering which has a huge cross section at low angles.

- as pointed out already in section III A, exclusivity is necessary in order to get reliable results. It can either be ensured by the detection of the 3-particle final state or by the detection of two out of the three particles and the missing mass technique, assuming the resolutions are good enough. The E00-110 experiment made the initial choice to detect the three particles in the final states. This required a large out-of-plane acceptance for the proton at forward angles, in a fairly limited space.

1. Experimental setup

The E00-110 experiment was conceived with a few key elements in mind, especially regarding the above-mentioned issues. The factorization of DVCS needed to be checked before

any satisfactory studies of GPDs could even begin. In order to do so, we proposed a Q^2 scan at fixed x_B of the cross section difference for opposite electron helicities. The Q^2-dependence of the $\sin\phi$ and $\sin 2\phi$ can be checked against predictions. Also the $\sin\phi$ (twist-2) contribution should dominate over the $\sin 2\phi$ one.

In order to counter the small size of the cross section, this experiment used a fairly high luminosity in Hall A of Jefferson Lab, running at 10^{37} cm^{-2}s^{-1}, which corresponds to 2.5 μA of electron beam on a 15 cm-long liquid hydrogen target. The scattered electron was detected in the Hall A left High Resolution Spectrometer (HRS), which provides a very good momentum resolution $\delta p/p = 2 \cdot 10^{-4}$ and a fair angular resolution of 2 mrad in the horizontal plane. This pinpoints the electron kinematics and therefore the electron scattering plane as well as two out of the four non-trivial variables of the reaction: x_B and Q^2. The emitted photon was detected in an electromagnetic calorimeter covering ~ 0.1 sr, located at about 1 m from the target and centered in the direction of the virtual photon. Indeed, the spectrometer's acceptance is rather small and only selects virtual photons in a small solid angle or ~ 3 msr, as shown on Figure 10. The photon direction (two angles) with respect to the virtual photon direction (determined using the electron kinematics) is enough to fix the remaining two variables of the reaction: t and ϕ. The measurement of its energy is an extra handle on the exclusivity. The recoil proton was detected in the so-called Proton Array, a set of 100 blocks of plastic scintillator in a ring configuration around the virtual photon direction. This geometry was selected in order to have a simple azimuthal symmetry around the virtual photon direction, which is a key element for a smooth ϕ acceptance. The general setup of the experiment is shown on Figure 11.

High Resolution Spectrometer

The left spectrometer in Hall A consists in 4 superconducting magnets in the configuration QQDQ. In the E00-110 experiment, the left HRS was used to detect the scattered electron and therefore define the virtual photon kinematics in an accurate way. The main components of the detector stack are as follows: A set of two scintillator planes called S1 and S2m giving very fast and good timing signals; a vertical drift chamber for track reconstruction; a gas Cerenkov counter for π/e discrimination; a pion rejector composed of Lead glass block which is used in addition to the Cerenkov detector to select a clean sample of electrons.

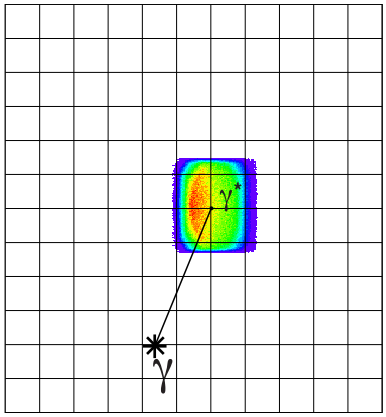

FIG. 10: Virtual photon acceptance at the front face of the electromagnetic calorimeter. The variable t is linked with the distance between the "impact" of the virtual photon and the real photon. The angle ϕ is simply given by the azimuthal angle of the photon with respect to the virtual photon direction.

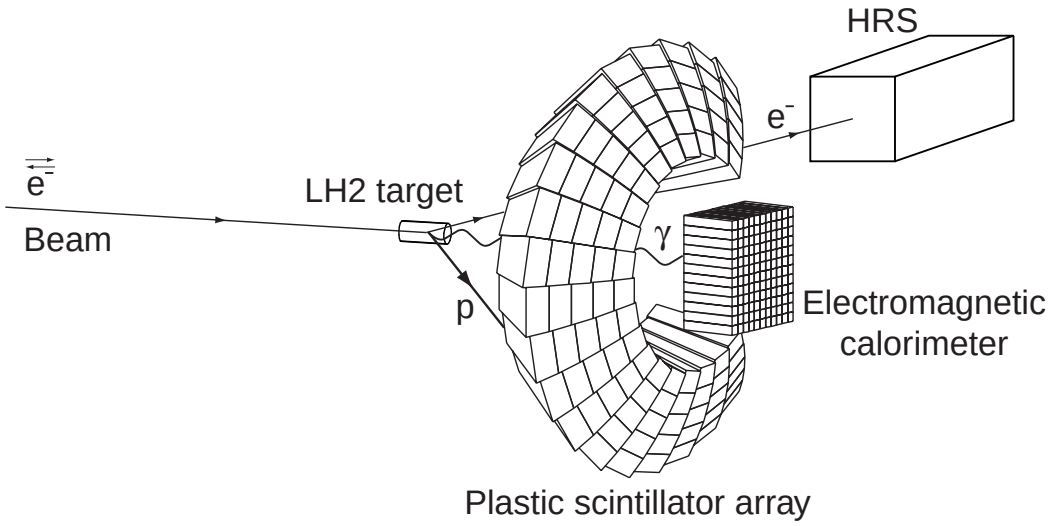

FIG. 11: Setup of the E00-110 experiment in Hall A of Jefferson Lab.

As mentioned below, a fast signal from S2m was used as a level 0 trigger for the rest of the electronics. It is useful to recall the angular acceptance of the left HRS for electrons : ±30 mrad horizontal and ±60 mrad vertical.

High performance Electromagnetic Calorimeter

One of the key elements of this experiment was a dedicated Cerenkov light electromagnetic calorimeter, consisting of a 11×12 array of lead fluoride 3×3×18.6 cm^3 blocks. The size of the blocks is adapted to the radiation length and Moliere radius of PbF_2 so that a shower is almost completely contained in a cluster of 9 blocks, both longitudinally and transversally. Each block was equipped with Hamamatsu R7700 fine-mesh photomultiplier tubes (PMT). During the experiment, the relative gain of the PMTs were monitored using a set of LEDs. However, the large luminosity the experiment ran at induced radiation damage very near the front face of the blocks. Since the LED light was injected in the front face, this method proved very unreliable to measure the real gain variation related to high energy photon showers. Indeed, the Cerenkov light is mostly produced deeper in the crystal, avoiding the damaged area. Figure 12 shows some shower profiles for different incoming particles, especially an electron of typical energy for our electromagnetic background and multi-GeV showers typical of DVCS photons. The calibration coefficients were actually monitored using over-constrained physics processes such as elastic scattering (before and after the experiment), π^0 and π^- electroproductions. Overall, these coefficients were known for any given time at the 1%-level.

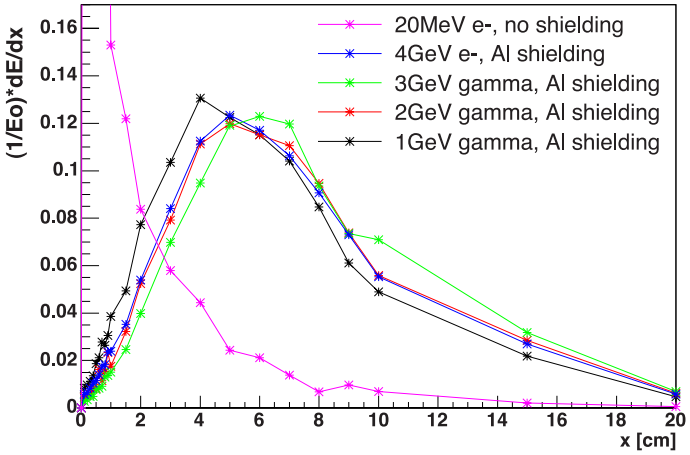

FIG. 12: Shower profiles as simulated by GEANT3.21 for different photon energies and shielding configurations described in the legend. In particular, low energy electrons deposit most of their energy very close to the front face of the calorimeter whereas high energy photons have a shower profile peaking at about 5 cm inside the calorimeter.

Proton Array

In order to detect the full exclusive final state, a recoil detector was built in order to tag the DVCS proton. The main difficulties of such a detector is that it needs to detect low-momentum protons in a large solid angle, fairly close to the beam line, with as high an efficiency as possible. The recoil proton direction could be inferred by the information from the HRS and the calorimeter, therefore one could check in the Proton Array if the proton was actually at the right position. The PA subtended a solid angle (relative to the nominal direction of the virtual photon) of $18^\circ < \theta_{\gamma^* p} < 38^\circ$ and $45^\circ < \phi_{\gamma^* p} < 315^\circ$, arranged in 5 rings of 20 detectors as shown on Figure 11. The scintillator blocks were 30 cm-long and equipped with Photonis XP2972 PMTs. The 90° cut-off in $\phi_{\gamma^* p}$ allows for the exit-beam pipe in the kinematic setting where the detector stack is the closest to the beamline.

Electronics

The E00-110 experiment was designed with open detectors at low angles (the blocks of the calorimeter closest to the beam line were at 6.5°) with limited shielding running at high luminosity. High singles rates up to 10 MHz were expected and also measured in a test run during the design phase. In this environment, regular ADCs even with a reduced gate are strongly affected by pile-ups. We therefore chose to use digitizing electronics for all the electronics channels of the dedicated detectors (calorimeter and Proton Array), namely a custom 6U 16 VME (A24/D32) module sampling system based on the Analog Ring Sampler (ARS) CMOS ASIC developed at Saclay [43, 44].

The ARS uses the concept of analog memories to sample data at a clock rate of 1 GHz: it consists in a circular array of 128 capacitors on which the incoming signal is continuously switched. Every 1 ns, the ARS points the signal to the next capacitors, eventually over-writing itself after 128 ns. When a trigger is issued, the array is frozen and the previous 128 ns are stored in the capacitors during 500 ns, after which the capacitor discharge may alter the data. A "Valid" signal has to be issued within this time frame in order to start encoding the data using 12-bit Flash ADCs. Each ARS ASIC contains four channels, and four ARS ASICs were implemented onto each VME board for a total of 16 channels per board. Figure 13 shows a typical calorimeter signal as a function of time read-out by the ARS system.

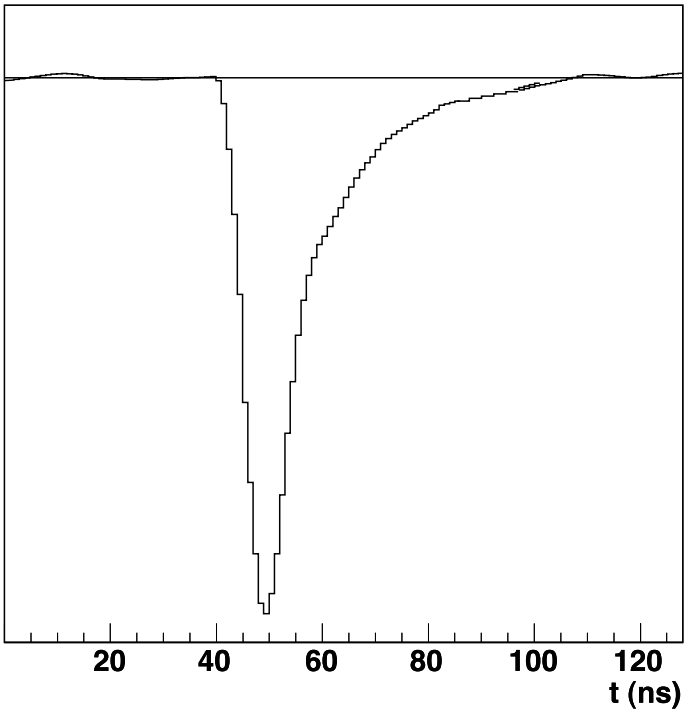

FIG. 13: Typical calorimeter pulse recorded by the ARS system.

Trigger scheme

The trigger system of a multi-detector experiment using state-of-the-art digitizing electronics such as E00-110 is rather involved. Firstly, ARS by design require the use of two trigger signals: a fast "Stop" signal needs to freeze the capacitor state of a potential candidate and a "Valid" signal which will start the encoding stage. The timing is set by the "Stop" signal, which has to be fast enough so that it is compatible with reasonable delay length for the detector cables as well as the 500 ns maximum delay before loosing the information in the ARS. The fastest and cleanest timing signal we could get was the signal from the S2m scintillator paddles in the left HRS. It is therefore a negatively charged particle which gave the ARS "Stop" signal.

Even though ARS represent a considerable advantage for this type of experiment it has an obvious drawback: the amount of data to transfer is about a hundred times higher than with regular ADCs due to the time sampling. For the 232 ARS channels of the E00-110 experiment, the event size is $232\times128\times16/8\sim$60kB.

Even though this document's purpose is not to give specific details about the analysis of a DVCS experiment, it is enlightning to describe the key steps involved with exclusive processes data analysis. It will not only help to understand the systematic uncertainties associated with such measurement, but it will also be quite useful in order to design and analyze future experiments.

The E00-110 data analysis involves several important steps : spectrometer analysis, calorimeter analysis, proton array analysis and putting all this together in a cross section computation.

Spectrometer Analysis

The scattered electron of the photon elecproduction process is detected in the left HRS of Hall A. Since the detection of this electron is the least difficult part of the experimental setup, it needs to bring the least complications to the data analysis. In this respect, the main goal of the spectrometer analysis is to get a clean electron 4-vector, within a well defined and flat acceptance.

The spectrometer selects negatively charged particles because of its magnetic polarity. In order to identify electrons from pions, the signal from the CO_2 Cerenkov detector is used. The separation is almost perfect in our momentum range, yielding a purity of 99% for an efficiency of 99.8%. Note that 99% of the 1% electrons which turn out to be pions will be rejected by further exclusivity cuts in our analysis.

Once the identification is done, the Lorentz vector for the electron is easy to build using the measured momentum and angles. Note that the spectrometer was already well calibrated and surveyed from past measurements in Hall A and did not require further studies during the experiment. In order to extract reliable cross sections, it is essential to define an accurate (and as flat as possible) acceptance area. This is especially important since particles at the acceptance edge might be poorly reconstructed and suffer larger systematic uncertainties. The acceptance function of such a spectrometer is a complicated function of the track angles, momentum and vertex location. It may be defined by both the apertures of the different magnetic elements but also, of course, their transport matrices. It is unwise to cut on vertex variables to define the acceptance as they become completely correlated because of

the tracking through the spectrometer. An acceptance function depending on only one parameter, called a R-function, can be built in order to place a 4-dimensional cut much more efficently, effectively cutting "edges" on all vertex variables at once. Figure 14 shows the effect of the R-function cut on the vertex angles of the track, defining a clean acceptance region.

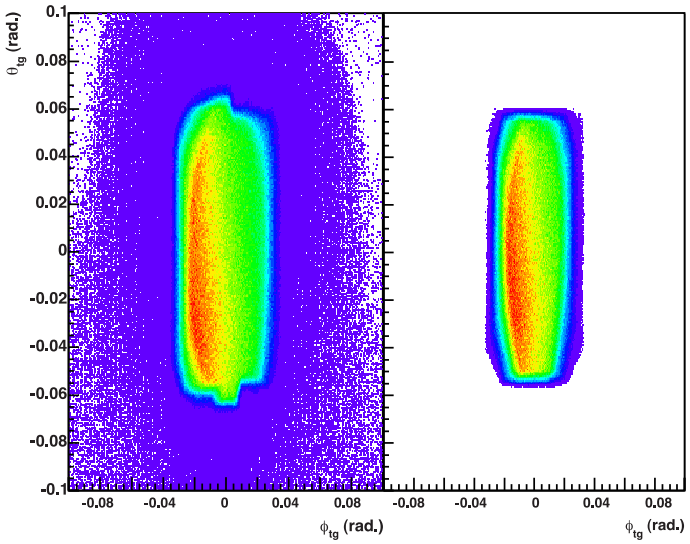

FIG. 14: Effect of the R-function cut in the plane (θ, ϕ) at the target.

Since the rate in the spectrometer is relatively small, more than one track events are suppressed very early in the analysis stage, and corrected for a global inefficiency of 8 to 15% (depending on the spectrometer angle) later on. Finally, in order to get a pure liquid hydrogen sample, excluding the target aluminum walls, only 13.5 cm of the 15 cm cell were used in the data analysis. For the cross section normalization, the luminosity was of course calculated using this value.

This spectrometer analysis allowed us to have a clean sample of electrons, in a well-defined acceptance region in x_B and Q^2, at the expense of a reasonable statistical loss from identification, acceptance, multi-track and target cuts.

Calorimeter Analysis

The analysis of calorimeter data is a lot more tricky than the spectrometer. Moreover, it is extremely important to have the best possible information about the outgoing photon in the DVCS process, since it is typically a 2-3 GeV photon carrying a large fraction of

the available energy. The quality of the calibration and the resulting energy resolution are therefore critical in order to perform a good selection of exclusive events.

Let us recall the calorimeter was located at approximately 1 m from the target center, with blocks at angles as low as 6° for the high Q^2 kinematics. In these conditions, the singles rate in low-angle blocks can reach values so high that regular ADCs with a typical 100 ns gate would integrate most of the time a pile-up pulse in addition to the pulse of interest, worsening the energy resolution dramatically. The ARS system described previously allowed for a multi-pulse analysis of the digitized output of the photomultipliers, essentially recovering most of the performance of the calorimeter. The high rate in the low-angle blocks also induced radiation damage, mostly (but not completely) located at the front face of the calorimeter block.

We performed elastic H(e,e'$_{calo}$ p$_{HRS}$) calibrations at three points during the experiment, and noticed that the light output of the calorimeter blocks decreased by up to 20%, correlated with the distance from the beamline. The calibration coefficients were adjusted in between calibration assuming the signal attenuation is linear with the received dose. The calibration was then verified and slightly adjusted using other channels such as the π^0 electroproduction. The resulting resolution on the π^0 mass from the two detected photons can be seen on Figure 15. The calorimeter calibration after all these steps was known at the 1%-level whereas the energy resolution estimated using elastic scattering was 2.4% at 4.2 GeV.

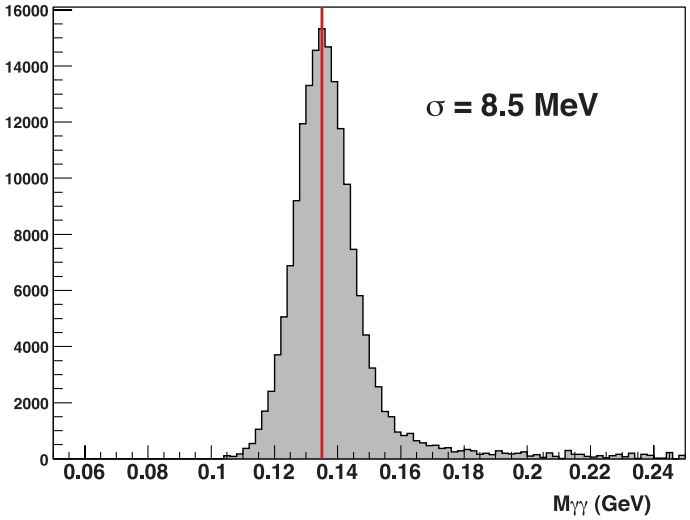

FIG. 15: Invariant mass of the two-photon events detected in the calorimeter after final calorimeter calibration. A fit to a gaussian results in $\sigma = 8.5$ MeV for all π^0 energies.

Proton Array Analysis

The Proton Array was used as a "check" detector : the DVCS process is already over-constrained detecting the scattered electron and the outgoing photon. The idea is to assume the DVCS reaction and using the four-momenta of the electron and photon, guess the location of the DVCS proton inside the Proton Array. Then, all we need to do is check that there is actually a hit in the Proton Array in the right block(s), in time with the rest of the event. In that sense, only a crude energy calibration is needed for the proton array, in order to gain-match all the channels, fix the threshold and be able to reproduce it in the simulation later on. Note that using the Proton Array to tag the recoil proton in the definition of a DVCS event reduces the statistics by a significant amount, especially at low-t and ϕ around 180°.

As far as the analysis is concerned, the proton array suffers some of the same problems the calorimeter does : some blocks are located at low angle with respect to the beamline. Even though radiation damage to the scintillator blocks themselves is not an issue, the high amount of light produced constantly affects the photomultiplier tubes and their gain changed for some of the most exposed blocks. For physics analysis, a waveform analysis of the PMT signals was used as well, but in a much worse environment compared to the calorimeter. Indeed, except for protons stopping inside the Proton Array, the energy deposit was not a large signal compared to noise, as was the case for the calorimeter. Figure 16 shows a typical signal recorded in the ARS for a DVCS process in a 128 ns window. The "good" pulse is the one peaking around 60 ns. Obviously, the efficiency of the proton reconstruction is lower than in the case of the calorimeter, about 85% for most of the Proton Array, except for blocks very close to the beam line. The amount of random hits which may mimick a DVCS proton, *i.e.* contamination, depends on the block location, but is typically of the order 5%.

DVCS event selection

Once a good electron is selected using the spectrometer data, events with only one photon (one cluster of calorimeter blocks) are used in order to build a missing mass spectrum shown on Figure 17 (top). Assuming the event is a DVCS event, the recoil proton trajectory is infered and events with a corresponding proton in the Proton Array are selected. This corresponds to the events on Figure 17 (bottom). It is compared with the missing mass

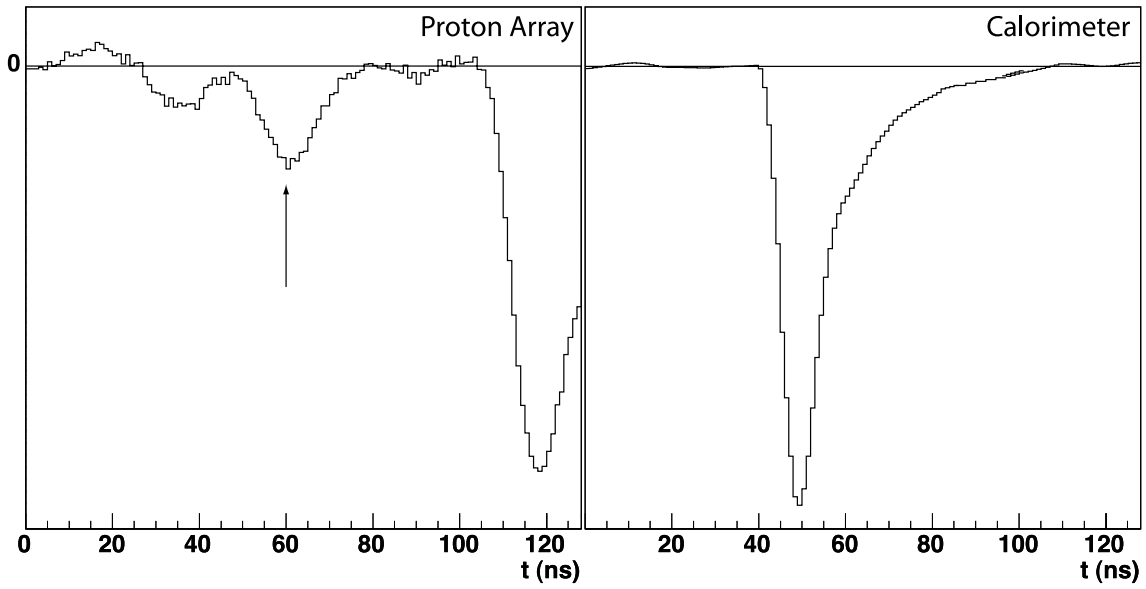

FIG. 16: Typical signal recorded in the ARS for a DVCS process for the proton (left) and the photon (right) in a 128 ns window. For the proton ARS waveform, an arrow points to the signal in time with the HRS and the calorimeter.

distribution using a Monte Carlo simulation of our setup with DVCS events, and we find a solid agreement up to $M^2_{e\gamma X} \sim 1.5$ GeV^2. At this point, one could simply use this very clean data sample in order to extract DVCS cross sections. However, going back to the $e\gamma X$ sample, it is instructive to estimate the background coming from non-exclusive events under the missing mass peak. In order to do so, we used the left part of the $e\gamma p$ missing mass spectrum (before much of the contamination occurs) and fitted the $e\gamma X$ missing mass, leaving only the normalization as a free parameter, as show on Figure 18. The vertical line shows the location of $M^2_{e\gamma X} = (M_p + M_\pi)^2$, which is, barring any resolution effects, where the contamination from non-exclusive events starts. Integrating the difference of the $e\gamma X$ sample with the scaled $e\gamma p$ sample, one finds a contamination of $\sim 2\%$ only, while improving the statistics from the pure $e\gamma p$ sample by almost a factor 5! Even though it was obvious that a careful estimation of the residual contamination under the proton peak was necessary, it became clear that we had much to gain and little to lose using the full $e\gamma X$ sample and not requiring a recoil proton in the analysis. Moreover, the acceptance calculation by Monte-Carlo would be much simpler since less cuts and less knowledge of the apparatus are required in this case, largely compensating the increase in systematic error due to background subtraction.

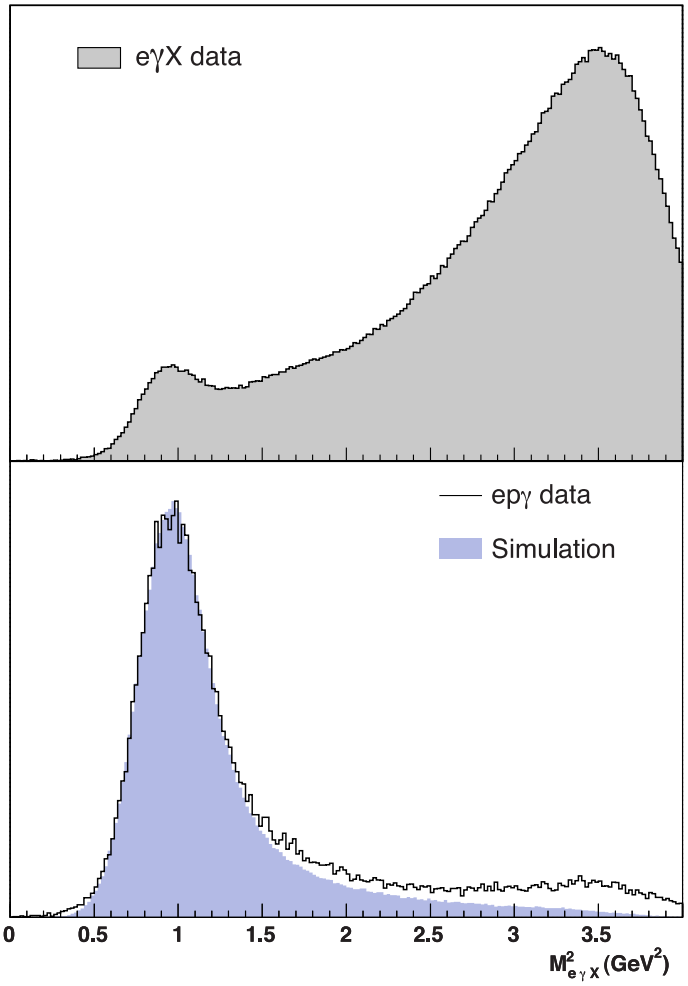

FIG. 17: (top) Missing mass spectrum for all $e\gamma X$ events. (bottom) Same events but with a corresponding proton in the proton array at the right time and position (black histogram) compared to Monte Carlo expectation (blue-filled histogram). This demonstrates a solid agreement up to $M^2_{e\gamma X} \sim 1.5$ GeV^2.

Neutral Pion Background

The main competing channel for DVCS is the electroproduction of π^0 where the π^0 decay is very asymmetric, which is essentially not distinguishable. This background therefore needs to be subtracted. Note that in this respect, it is essential to keep the $M^2_{e\gamma X}$ cut small to limit the number of π^0 events sneaking under the peak.

The estimation of the π^0 contamination is rather simple: firstly, we count the number of π^0 events with two photons detected in the calorimeter, by using two-cluster events. Then we simply infer the number of one-photon-detected π^0 events using a very simple simulation

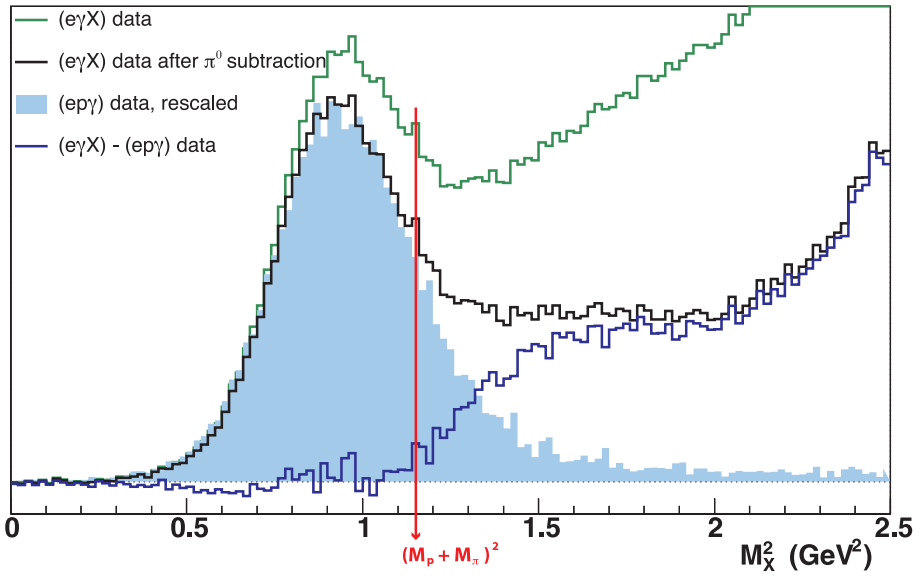

FIG. 18: Close-up view of the full $e\gamma X$ data sample (green histogram). The black histogram corresponds to the same events after π^0 subtraction. It is compared to the blue-filled histogram, rescaled from Figure 17. The remaining background is shown as the dark blue histogram. The vertical line shows the location of $M^2_{e\gamma X} = (M_p + M_\pi)^2$, which is, barring any resolution effects, where the contamination from non-exclusive events starts. Integrating the difference of the $e\gamma X$ sample with the scaled $e\gamma p$ sample, one finds a contamination of $\sim 2\%$.

since π^0 decay is isotropic. In a sense, the simulation estimates the ratio of acceptance between one-photon and two-photon π^0 events, and the number of π^0 decaying into two photons in our data gives us the normalization. There are two complications to this method: Firstly, the energy of the π^0 photons is obviously lower than for DVCS photons. Since the threshold for the calorimeter was rather high, we lost part of the π^0 events this way. However, the energy distribution of the two π^0 photons is flat in the laboratory frame and we can estimate the number of photons lost in between the DVCS threshold and the corresponding π^0 threshold. Secondly, edge effects for π^0 happen twice as much as for DVCS, since there are two photons: indeed, either of the two photons can get close to the edge and be cut out of the analysis, which tends to under-estimate the contamination. This systematic error was evaluated using a full Monte-Carlo simulation. Moreover, the subtraction procedure was double checked using π^0 cross sections measured in the same experiment and a full GEANT simulation of the detector setup.

Cross sections

In order to extract cross sections from the number of DVCS counts (already corrected for detection and cut efficiencies as well as π^0 contamination), one needs to know the solid angle (or acceptance) and the integrated luminosity over the course of the experiment. The average cross section in a bin in (x_B, Q^2, t, ϕ) is then simply the ratio of the number of counts in that bin divided by the bin phase space (the integration of the solid angle over the experimental apparatus) times the integrated luminosity. In the specific case of the DVCS, the general structure of the cross section as a function of the kinematic variables was known beforehand using the formulae in [19]: linear combinations of GPDs enter the cross section, weighted by known kinematical factors. It is therefore possible to include all the kinematical factors in the phase space integration in order to avoid averaging rapidly varying functions of the kinematic variables. We can summarize this in the following equation:

$$N_i = \mathcal{L} \int_i \Gamma(x_B, Q^2, t, \phi) \mathcal{F}(GPDs) d\Omega = \mathcal{L} \left\langle \mathcal{F}(GPDs) \right\rangle \int_i \Gamma(x_B, Q^2, t, \phi) d\Omega \,, \qquad (48)$$

with N_i the number of counts in bin i, $\mathcal{L}$ the integrated luminosity, $\Gamma(x_B, Q^2, t, \phi)$ the kinematical factor in front of the linear combination of GPDs $\mathcal{F}(GPDs)$. The last integral is evaluated using a Monte Carlo simulation based on GEANT 3.21, specifically written for this experiment.

The external radiative effects on the incident electron and internal real radiative effects at the vertex are treated in the equivalent radiator approximation [45, 46]. Internal pre-radiation as well as post-radiation are modeled by generating an event-by-event energy loss following the prescriptions in [45, 46]. External post-radiation by the scattered electron is modeled within our GEANT 3.21 Monte-Carlo, up to the spectrometer window.

Two types of observables were extracted at the highest Q^2=2.3 GeV^2: the difference of cross sections for opposite helicities and the total cross section, both shown on Figure 19 (left). In addition, the difference of cross sections for opposite helicities were extracted from the two other Q^2 settings at 1.5 GeV^2 and 1.9 GeV^2. The associated systematic errors were evaluated to be 5 to 6% depending on the observable, dominated by the acceptance evaluation, the background subtraction and the beam polarization uncertainties in the case of the cross section difference. The Q^2 dependence of the imaginary part of the linear combination of Compton Form Factors $\mathcal{C}^I_{unp} \equiv \mathcal{C}^I$ (defined in section II, Eq. 23) was extracted from the difference of cross sections at the three Q^2 settings and is shown on Figure 19 (right).

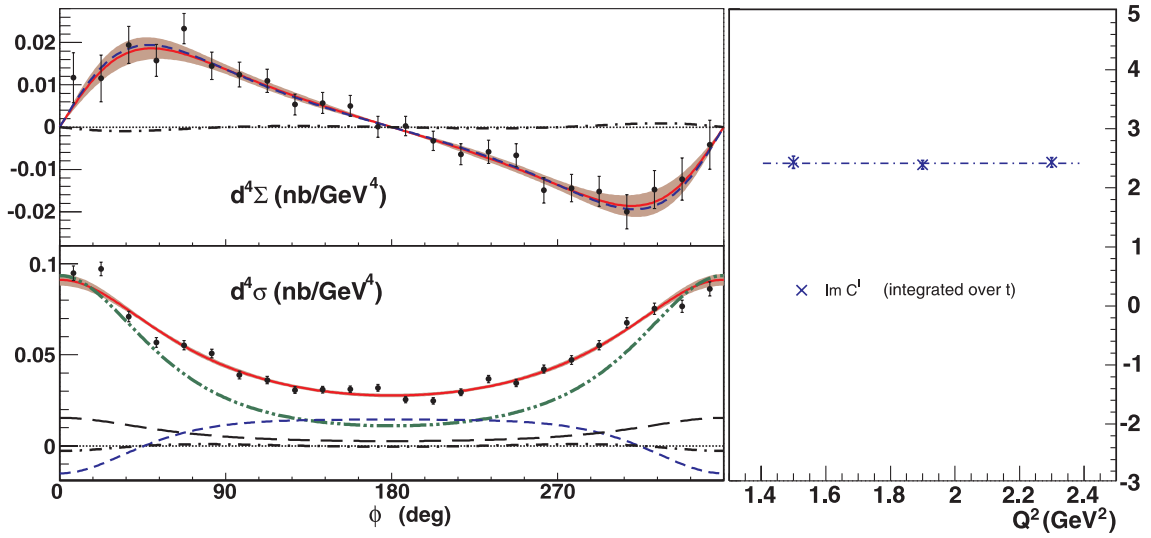

FIG. 19: (left) Data and fit to the cross section difference (top) and total cross section (bottom), as a function of ϕ, both for the high Q^2 bin. Error bars show statistical uncertainties only. Solid lines show total fits with one-σ statistical error bands. The green dot-dot-dashed line is the $|\mathrm{BH}|^2$ contribution. The short-dashed lines are the fitted imaginary parts (top plot) and real parts (bottom plot) of $\mathcal{C}^I$, respectively. (right) Extracted coefficient $\mathrm{Im}\mathcal{C}^I$ in blue as a function of Q^2. The absence of Q^2-dependence is expected if the handbag process is dominant for this observable.

The main conclusion, as written in our Physics Review Letters article [47], is that there is no observed Q^2 dependence of the extracted combination of GPDs (at $x = \xi$) within our statistical and systematic error bars, including the expected logarithmic Q^2 dependence coming from QCD evolution. The conclusion has to be moderated by the rather small lever arm in Q^2 but is still significant at these low-Q^2 values. Moreover, the extraction of $\mathcal{C}^I$ is dependent on the harmonic analysis done in [19], which is now known to have some approximations which may affect the result [20]. However, it was checked that since the lever-arm in Q^2 is only of about 1 GeV^2, the conclusion about the scaling in DVCS is still valid as all the data points move by about the same amount, and the relative flatness of the dependence remains.

The total cross section is more difficult to interpret as the parametrization does not allow to disentangle between the interference and DVCS^2 terms. A future experiment in Hall A at different energies will take data in the end of 2010 and will try to disentangle the different terms in the total cross section [22].

C. Jefferson Lab Hall A experiment E03-106: DVCS on the neutron

A study of DVCS on the neutron was proposed shortly after the proton DVCS experiment in Hall A [11] and actually ran in 2004, following the E00-110 proton experiment. The main interest is actually not the obvious flavor content difference between proton and neutron targets but comes from the fact that the GPDs are weighted very differently in the two cases: whereas for the proton case, the Compton Form Factor $\mathcal{H}$ dominates $\mathcal{C}^I$ which is extracted from the cross section difference, it is replaced in the neutron case by the Compton Form Factor $\mathcal{E}$. Considering the GPDs E and H enter on equal footing in Ji's sum rule, it strongly justifies this study of neutron DVCS even though the experiment is even more difficult than the proton DVCS. The neutron experiment is more time consuming than for the proton, and we only ran one kinematical point, at Q^2 =1.9 GeV^2, $x_B = 0.36$ and t from -0.5 GeV^2 to t_{min}.

1. Experimental Apparatus

The neutron experiment was very similar to the proton E00-110 : it used the same spectrometer, calorimeter and proton array. The target was replaced by a liquid deuterium target of the same 15 cm length, acting as a quasi-free neutron target. An additional detector called the "tagger" was put in front of the proton array, as shown on Figure 20. The initial idea was that two layers of thin scintillator counters would be able to see protons but would be insensitive to neutrons and could therefore discriminate between the proton and neutron DVCS that occur in the deuterium target. As it turned out however, this tagger was not used in the final data analysis for different reasons: Firstly, it suffered the same problem the calorimeter and the proton array had in the proton experiment : Especially at low angles with respect to the beamline, the background rate was so high that it was both fairly difficult to get the counters to work properly and tricky to analyze, even using the 1 GHz sampling

system to isolate the good pulse. Indeed, the scintillators were only 2 cm thick and the gain needed to be limited because of the low energy background rate. This resulted in a signal to noise ratio which was worse than for the Proton Array, making a further pulse shape analysis inefficient. Secondly, the observable itself, the cross section difference for opposite electron helicities, was very small, actually compatible with zero within our statistical error bars as will be shown later. This is both due to the fact that the cross section itself is lower by about a factor 3 (the Bethe-Heitler is reduced due to neutron form factor) compared to proton DVCS and there is a cancellation of the u and d quark contribution to the cross section difference. The neutron efficiency of the proton array was only of the order 20%, not to mention its use reduced the acceptance of the recoil particle by a significant amount. It was necessary to increase the statistics of this experiment as much as possible and therefore an analysis without the Tagger and the Proton Array was attempted.

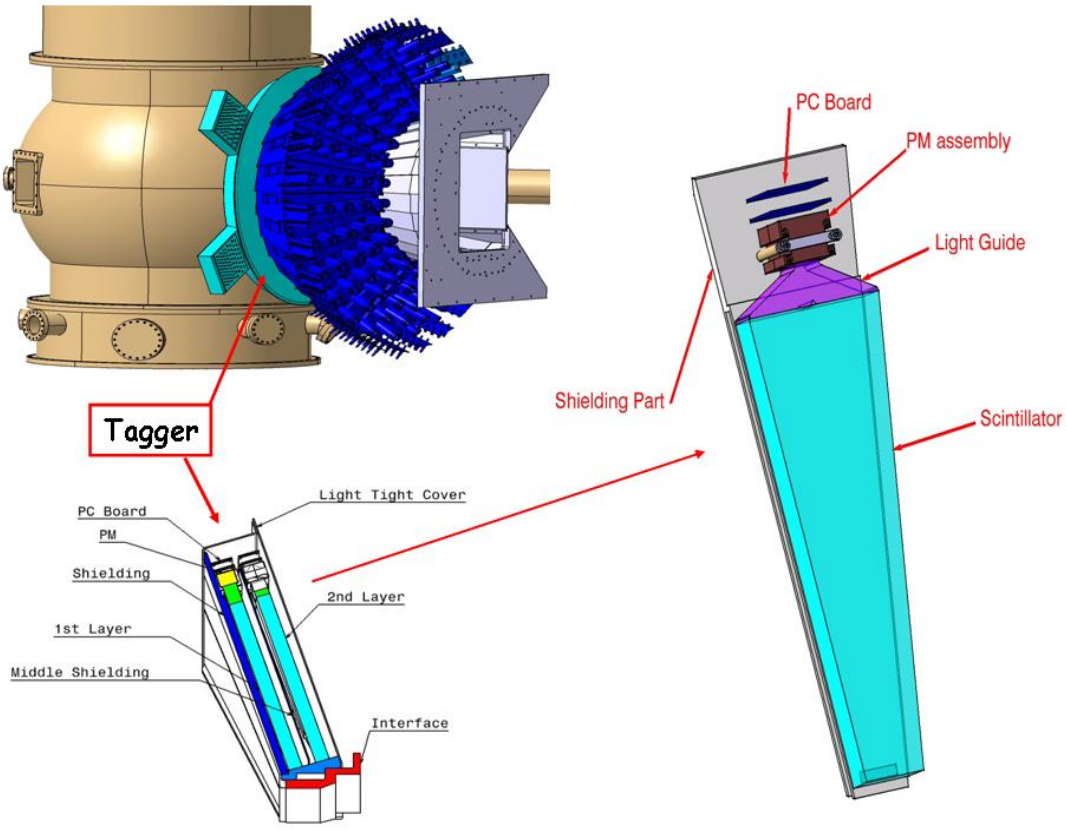

FIG. 20: Schematic showing the Proton Array and Tagger detectors in their data taking position against the target scattering chamber, with a close-up views of the individual tagger units.

2. Data analysis

Again, the detector analysis as well as the DVCS event selection follow closely what was done for the proton experiment and will not be detailed here. As stated before, even though the experiment was capable of doing triple coincidence analysis of neutron DVCS, it was soon given up because of statistical issues. The analysis was performed using the fact that we had run a proton DVCS experiment at specifically the same kinematical setting before. Within the impulse approximation, valid at these low transfered momenta, the photon electroproduction cross section on deuterium may be decomposed into quasi-elastic proton and neutron DVCS and elastic deuteron DVCS. In order to extract the neutron DVCS from the sum of all these processes, we subtract the normalized proton DVCS counts from the deuterium counts, effectively leaving only the sum of the quasi-elastic neutron and deuteron DVCS events.

The helicity signal S_h is defined as follows :

$$S_h = \int_0^{\pi} (N^+ - N^-) dx_B dQ^2 dt d\phi - \int_{\pi}^{2\pi} (N^+ - N^-) dx_B dQ^2 dt d\phi \tag{49}$$

It corresponds to the count difference for opposite helicities integrated on all kinematical variables except for ϕ, where the expected anti-symmetry around π is taken into account. The helicity signals for the deuterium and proton data are shown on Figure 21 (top) as a function of missing mass squared, which is calculated in both the proton and deuterium cases using the mass of the proton. For elastic deuteron events, the missing mass is therefore systematically shifted by $\Delta M^2_{e\gamma X} \simeq -t/2$. Once the proton data are subtracted from the deuteron data sample, the residual helicity signal shown on Figure 21 (bottom) is compatible with zero, indicating a small contribution of the neutron and deuteron DVCS.

3. GPD analysis

Following a method similar to the proton DVCS analysis, the data are analyzed using a simulation of both deuteron and neutron DVCS. In order to disentangle both contributions, and contrary to the proton case, the data are binned not only in ϕ but also in missing mass squared $M^2_{e\gamma X}$ since the deuteron and proton events are slightly shifted as explained before. Figure 22 shows the resulting values for $\mathrm{Im}\mathcal{C}^I$, for both the deuteron (top) and neutron (bottom). As expected, both combinations show extremely small values, which is actually

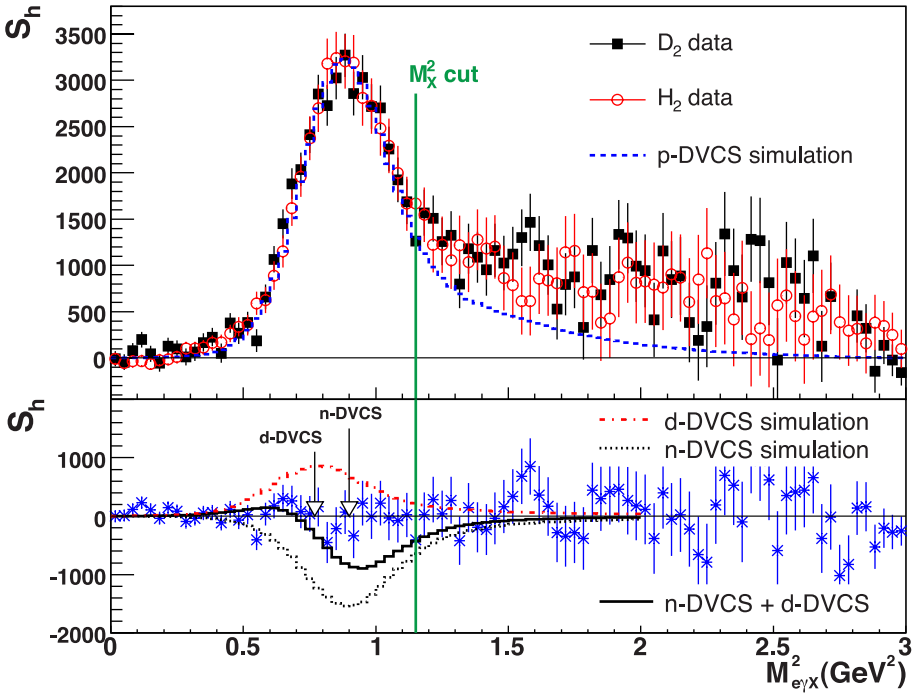

FIG. 21: (top) Helicity signal S_h for D_2 and H_2 targets (smeared for Fermi momentum and scaled to match Deuterium). (bottom) Residual helicity signal after H_2 subtraction from D_2 data sample. The M_X^2 cut is indicated by the green line. Simulation curves integrated over the experimental acceptance are shown to illustrate the respective sensitivity to neutron and deuteron DVCS.

expected by models [36, 48–50]. Note that the VGG model, even though it is known to fail at reproducing asymmetries or cross sections at better than 30-40% accuracy, has the interesting feature to parameterize the GPD E with the u and d quark contributions to the proton angular momentum J_u and J_d. It is therefore possible to fit the neutron DVCS data with VGG using J_u and J_d as free parameters and check if the neutron DVCS has indeed some potential with respect to constraints on the GPD E and therefore to Ji's sum rule. The resulting constraint is actually a linear combination of J_u and J_d shown on Figure 23.

The neutron E03-106 experiment was not entirely satisfactory: detecting the neutron in this noisy environment turned out to be impossible and forced us to subtract the hydrogen data from deuterium data in order to extract the neutron and deuteron information. The systematic errors are obviously increased since we used data from experiments which did not run at the same time, complicated by the fact that the calorimeter calibration changed with the received dose. As an exploratory experiment however, it gave us a lot of ideas and experience in order to design future experiments.

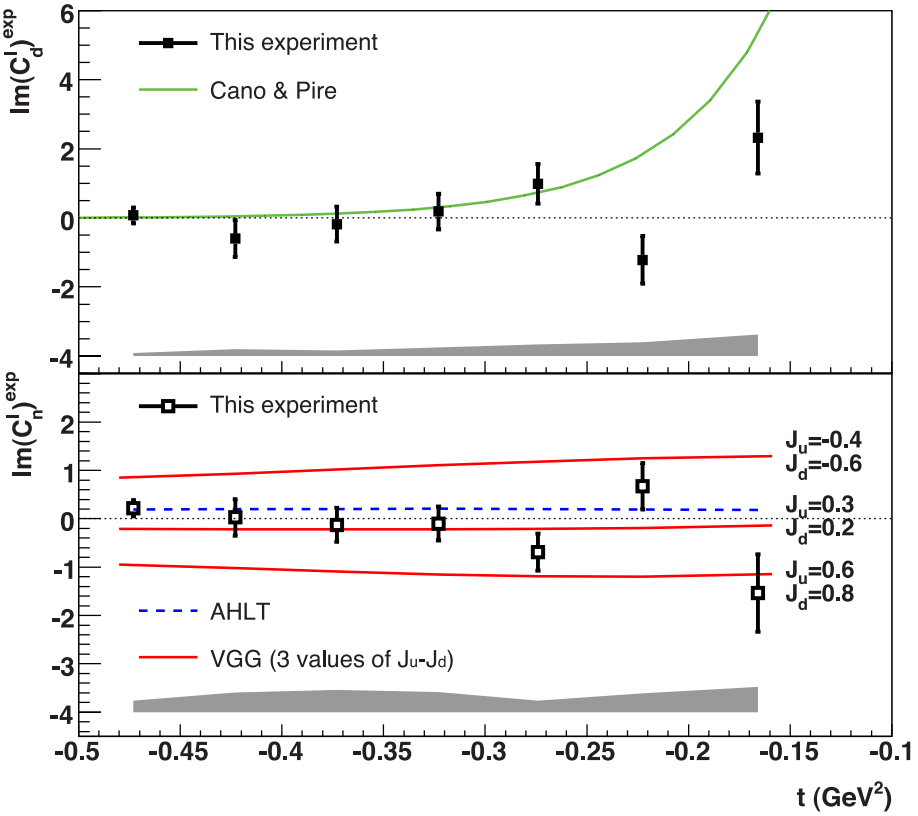

FIG. 22: t dependence of the extracted $\sin\phi$ moments for coherent d-DVCS (top) and n-DVCS (bottom). The curves show model predictions [36, 48–50]. Error bars show statistical errors whereas the systematic uncertainties are indicated by the shaded bands.

D. Jefferson Lab Hall B experiment E01-113: DVCS proton Beam Spin Asymmetries

E01-113 was the first dedicated Deeply Virtual Compton Scattering experiment in Hall B. It took place in the spring of 2005, using a 5.77 GeV polarized electron beam on a 2.5 cm liquid hydrogen target and detecting the photon electroproduction final state using the CLAS spectrometer, augmented by a forward calorimeter. The purpose of the experiment was to measure the DVCS Beam Spin Asymmetry (BSA) in a wide kinematical range, detecting the three final-state particles for full exclusivity.

The main limitation of the large acceptance spectrometer CLAS in Hall B for DVCS was the occupancy in the first region of drift chambers, and therefore the amount of beam current one was able to put on the target. With an operating luminosity of 2×10^{34} cm^{-2}s^{-1}, a record was set for the CLAS spectrometer, pushing the limit of what was possible to

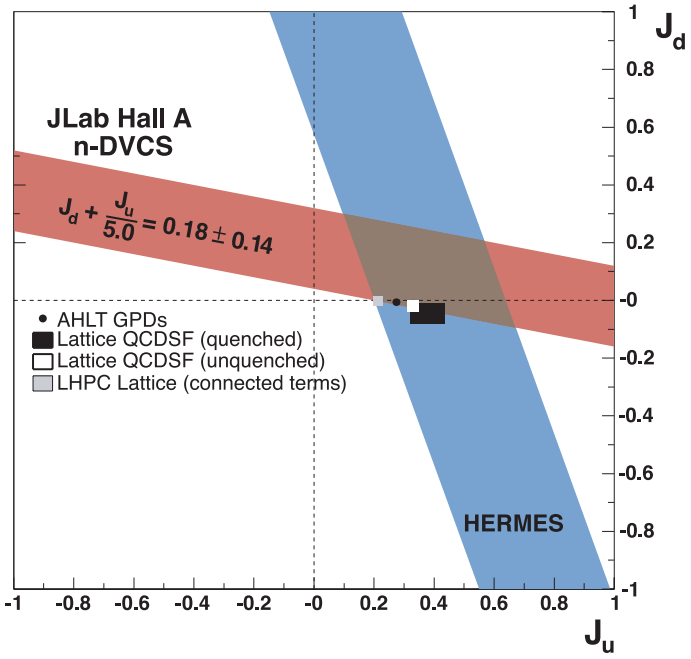

FIG. 23: Illustration of the experimental constraint on J_u and J_d, the total u and d quark angular momenta. A similar constraint from transversaly polarized target DVCS data comes from HERMES [51]. Several Lattice QCD calculations are also shown [52, 53]

achieve with such a spectrometer.

A secondary objective of the E01-113 experiment was the measurement of photon electroproduction cross sections. However, this proves to be a very ambitious project since CLAS is not designed for precision measurements. Indeed, the large acceptance is actually a limitation since it is close to impossible to select flat acceptance regions when a detector is large and segmented such as CLAS. Moreover, for total cross sections, it is necessary to subtract a large Bethe-Heitler contribution to get access to the DVCS and interference terms, which have much smaller cross sections. It is therefore vital to have statistical and systematic error bars of the order 5% or less in order to get reliable information once the subtraction procedure is done. The difference of cross sections has even a smaller magnitude, and requires at least the same accuracy.

Currently, there have been two CLAS articles published on Beam Spin Asymmetries of photon electroproduction and π^0 electroproduction in the deep virtual region [54, 55]. The analysis is still ongoing for cross section analysis, five years after the data taking, which illustrates how tricky such an analysis is with CLAS.

1. Experimental setup

The main component of the E01-113 experimental setup in Hall B was its spectrometer CLAS, consisting in 3 regions of drift chambers arranged in six sectors, the natural division of the superconducting toroidal magnet. The particle ID is accomplished using Time-of-Flight detectors (TOF) which provide a very accurate timing, as well as a gaz Cerenkov detector for electron-pion discrimination. An electromagnetic calorimeter (EC) is used both as an additional mean of electron-pion discrimination but also for neutral particle identification and energy or time measurement. A cut view of the CLAS detector is shown on Figure 24.

This standard CLAS setup was augmented with an inner calorimeter (IC) located 55 cm downstream from the target in order to detect photons in the few GeV range between 4.5 and 15° with respect to the beam direction. This calorimeter was built of 424 tapered $PbWO_4$ crystals, 16 cm long and 2.1 cm^2 cross section, read-out with avalanche photodiodes associated with low-noise preamplifiers. The gain was monitored all along the run using a LED system distributed at the front face of each crystal using optical fibers. Energy resolutions of about 4.5% for 1 GeV photons and angular resolutions of 4 mrad were routinely achieved. In order to protect this calorimeter from Møller background at these very low angles, a specificially-designed superconducting solenoid was used to trap the Møller electrons around the beam axis, while permitting the detection of recoil protons up to 60°. This new configuration of the CLAS detector is illustrated on Figure 25.

2. Data analysis

Electron selection

The electron identification relies on the drift chambers for the momentum analysis, and the TOF, the Cerenkov counter and the EC for particle id. Here follows a brief description of the cuts used in the analysis :

- A good track with charge $q = -1$ in the Drift Chambers, which passed the track-based tracking requirements (all the hits have to be in time), with a minimal momentum of 800 MeV/c mostly to avoid large radiative events. Moreover, the track needs to originate from the target, and be sufficiently far from the edge of the acceptance. This last set of cuts is called fiducial cuts and are mostly geometrical cuts around the

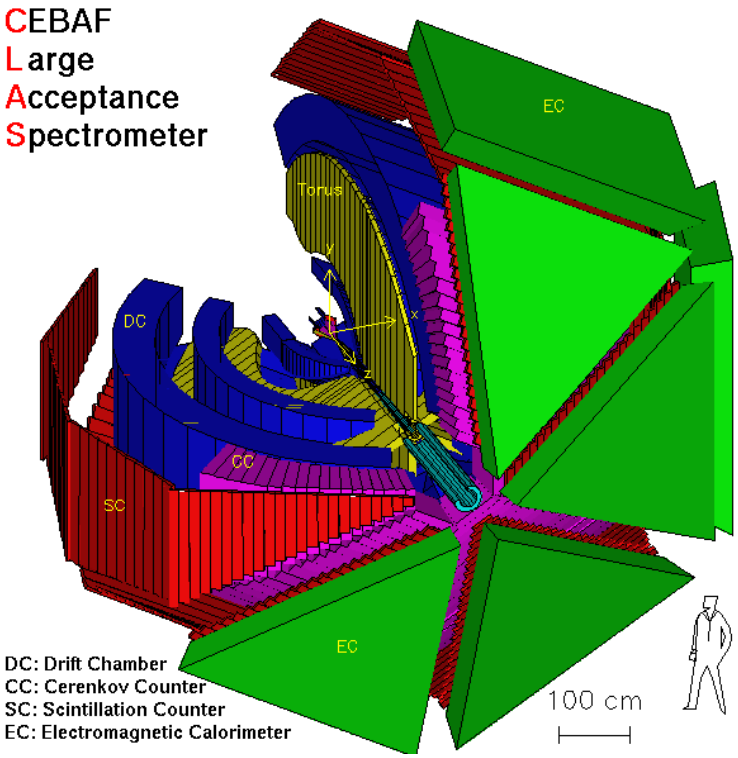

FIG. 24: Cut view of the CLAS spectrometer showing the various detectors around the torus, from the target out : Drift Chambers (DC), Cerenkov Counters (CC), Scintillation Counters (SC) and Electromagnetic Calorimeter (EC).

detector's edge, for each sector.

- In order to discriminate between electrons and pions, a cut on the minimum number of Cerenkov photons is applied, about 3 to 4 times lower than the maximum probable value of 9 photon-electrons, resulting in a high efficiency keeping a high purity.

- To get an even better purity of electron events, the EC is used in two ways : firstly, a minimum energy cut on the inner section of the EC is used, since minimum ionizing particles such as pions are only expected to leave about 30 MeV in it, whereas electrons deposit much more energy. Secondly, using the EC and the DC information, one can build the quantity E_{tot}/p which should be as a first approximation the sampling fraction of the calorimeter when the particle deposited all its energy in the calorimeter (about 0.25, since most of the calorimeter is actually lead, *i.e.* a passive material). For pions, which do not deposit all their energy in the calorimeter, this ratio is lower. As it turns out, the ratio E_{tot}/p is dependent on the momentum of the particle and a

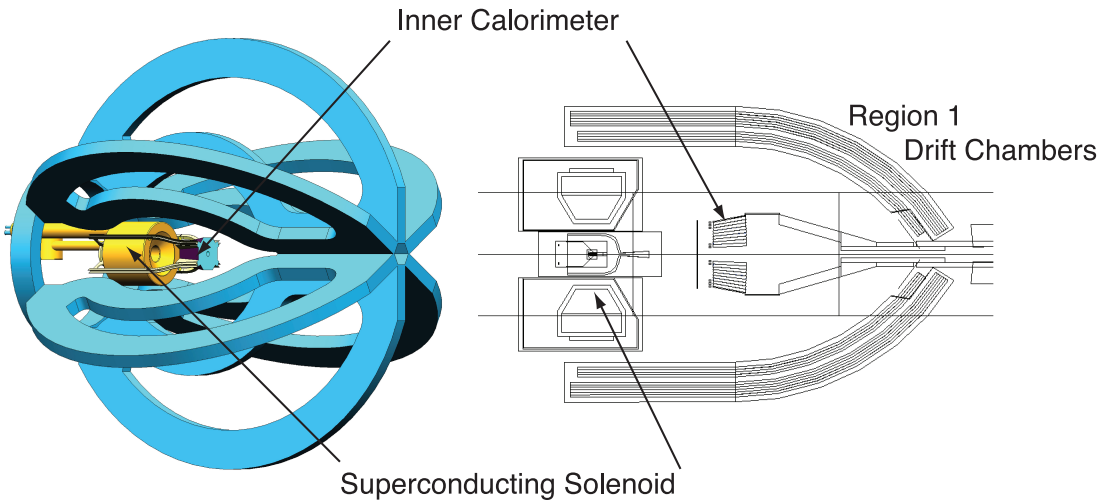

FIG. 25: (left) Artistic view of the CLAS torus in blue with the new solenoid in yellow. Attached to the solenoid is the new inner calorimeter. (right) Cut view of the target area, showing the solenoid coild surounding the target and the inner calorimeter 55 cm downstream of the target. The region 1 drift chambers are also shown around the inner calorimeter.

slightly more involved fitting procedure is needed to define the ideal cut, as shown on Figure 26.

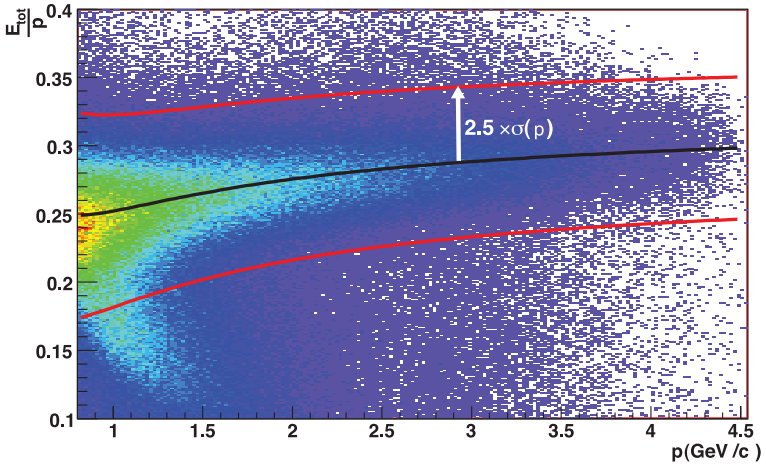

FIG. 26: E_{tot}/p vs. p for all sectors. The black line is a fit to a pure electron sample defined with other detectors. A cut of 2.5σ around this fit is applied to define good electrons (red lines).

Proton selection

The proton idenfication is somewhat simpler than for electrons, since the identification only relies on the Time-of-Flight counters. Here follows a brief description of the cuts used in the analysis :

- A good track with charge $q = +1$ in the Drift Chambers, which passed the track-based tracking requirements (all the hits have to be in time). Moreover, the track needs to originate from the target, and be sufficiently far from the edge of the acceptance. This last set of fiducial cuts is not the same as for the electrons since the positive charge of the protons changes the acceptance slightly. In addition, the effect of the solenoidal field is much more pronounced for protons.

- In order to discriminate between protons and pions, the β of the candidate protons is calculated in two ways : firstly, using the momentum information from the drift chambers and assuming the particle is a proton, $\beta_1 = \frac{p}{\sqrt{p^2+M_N^2}}$. Secondly, using the length of the trajectory evaluated using the drift chambers and the time of the track measured in the TOF counters, $\beta_2 = \frac{l_{track}}{c \cdot t_{track}}$. The difference $\Delta\beta = \beta_1 - \beta_2$ is shown on Figure 27 as a function of p. The pion population is clearly separated from the proton population at low p, which is our region of interest for DVCS. A simple cut $\Delta\beta < 0.05$ allows one to select a highly efficient and pure sample of protons.

Photon selection

Photons are identified both in the usual CLAS electromagnetic calorimeter EC and the inner calorimeter IC. Photons are required to have an energy of at least 150 MeV to be considered in this analysis. The identifications of photons is different for IC and EC. Indeed, IC has no possibility to make any type of identification, therefore any cluster of blocks hit is considered to be a photon in the IC. Only a geometrical cut to avoid the edge of the IC acceptance is used in order to avoid events for which the shower would spread out of the calorimeter and to avoid a large pile-up probability in the inner part, close to the beam.

In the EC however, one can use more information to select a pure sample of photons :

- A $q = 0$ track with no hits in the drift chambers and TOF and a hit in the EC is a candidate neutron or photon.

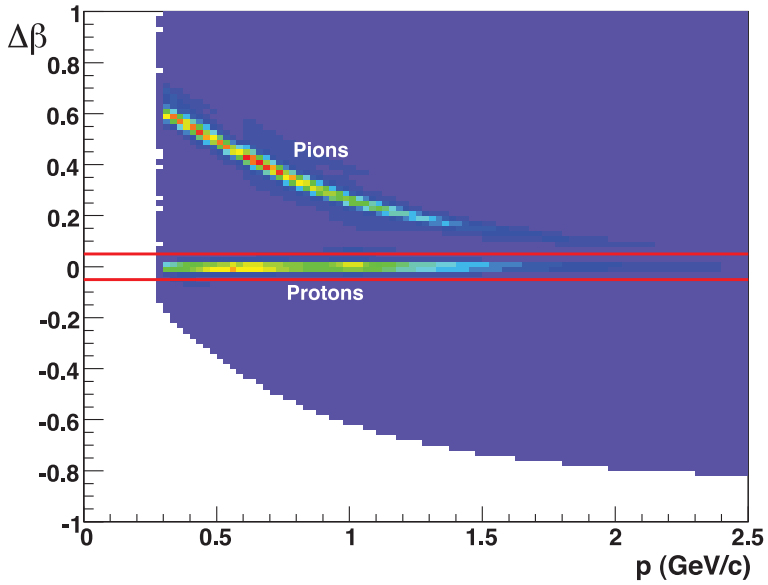

FIG. 27: Difference in the β of positively charged tracks between their estimation using the track length and the Time-of-Flight and their estimation using their measured momentum and assuming they are protons. The events around $\Delta\beta = 0$ correspond to the true protons. The pions accumulate at higher $\Delta\beta$.

- Geometrical cuts around the edges of the calorimeter are also used in the EC, to avoid loosing part of the shower energy because the particle would hit too close to the sensitive area.

- The β of the neutral particle is then calculated using its time-of-flight to the EC. A cut of $\beta > 0.95$ is used to select a clean sample of photons. Note that this cut optimizes the purity in exchange for a small loss in efficiency.

DVCS event selection

In order to select photon electroproduction events, a good electron, proton and photon (IC or EC) above 1 GeV are selected, as described above. There are no restrictions on the presence of more charged particles, although, in order to limit the π^0 contamination, no other photons above 150 MeV may be present in the event. In addition, kinematic cuts are used to select the deep inelastic scattering region for the electron kinematic : $Q^2 > 1$ GeV^2 and $W^2 > 4$ GeV^2.

The exclusivity of the reaction is ensured firstly by the requirement of having the needed

three particles in the final state. However, since there are no explicit cuts on the presence of more particles and it is always possible that a particle is not detected in the CLAS detector anyway, it is necessary to perform so-called exclusivity cuts. In the electroproduction process $ep \to ep\gamma$, there is in our case $3 \times 4 = 12$ measured variables corresponding to the three final state particles. However, one needs to subtract 4 constraints on the energy-momentum conservation and 3 known masses for the identified particles, leaving 5 independent variables. The observable being independent of the overall azimuth of the scattering plane, this actually leaves 4 variables to select exclusive $ep \to ep\gamma$ events. This analysis used five quantities, two of them being highly correlated :

- Considering any extra particle(s) X in the reaction $ep \to ep\gamma X$, we require the transverse momentum of X, $P_{X\perp}$ to be small : $P_{X\perp} < 90$ MeV/c for IC and 150 MeV/c for EC.

- The angle between the detected photon and the expected angle of the photon infered from the electron and proton kinematics $\theta_{\gamma X'}$ should also be small : $\theta_{\gamma X'} < 1.2°$ for IC and 2.7° for EC.

- The γ^*, γ and p vectors should be on the same plane, it is therefore possible to define a coplanarity angle φ, which again, should be small : $|\varphi| < 1.5°$ for IC and 3° for EC.

The value of the cut depends on the resolution of the detected particles, and since the photon is used for all cuts and the EC and IC have very different resolutions, it is necessary to proceed with different cuts depending whether the photon is in the IC or the EC. The distribution in these 3 variables as well as the missing energy E_X are shown on Figure 28 in the case of the photon detected in IC, before and after cuts. A study on the missing energy showed that a final cut on $E_X < 300$ MeV for the IC and 500 MeV for the EC was optimized as far as efficiency and purity are concerned.

In any case, just like the Hall A experiment, an evaluation of the π^0 background was performed using the same kind of procedure : firstly, evaluate with data the number of 2-photon-detected π^0s and then calculate the acceptance ratio whether one detects one or two photons of the π^0 decay. Then it is possible to infer the number of 1-photon-detected π^0's which can mimick the $ep \to ep\gamma$ process. The number of π^0 that one has to subtract

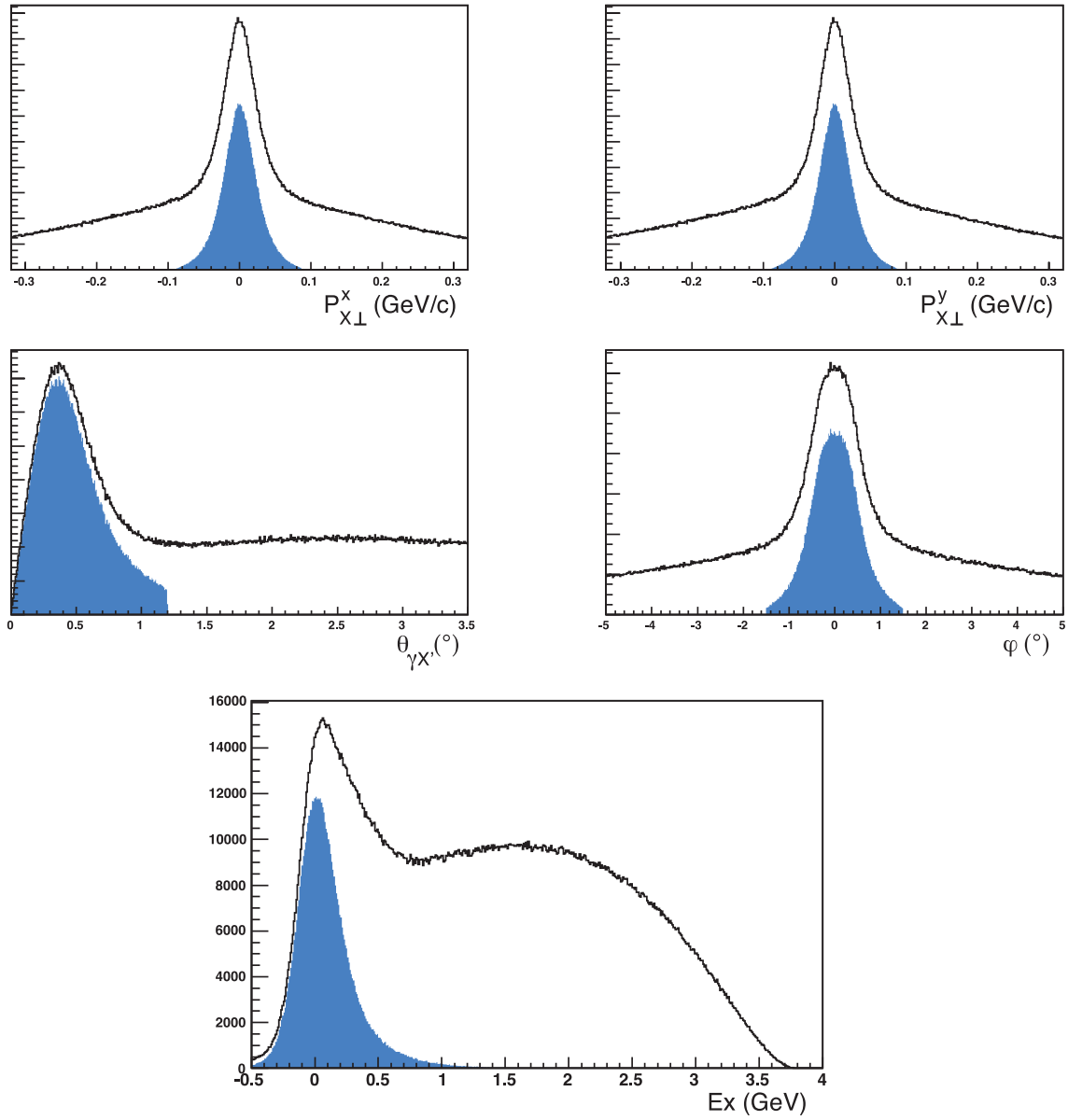

FIG. 28: Effects of the cuts described in the text on the selection of the photon electroproduction events. The black histograms are before cuts, the blue-filled histograms are after cuts. (top) Missing transverse momentum, x and y components. (middle) Cone and coplanarity angles as defined in the text. (bottom) Missing energy.

to our photon electroproduction sample is on average 10%, and sometimes goes over 20% at high t.

Beam spin asymmetries

Once corrected for the beam polarization and π^0 contamination, a sample of data on asymmetries as a function of ϕ is shown on Figure 29 for a few bins in (x_b, Q^2, t), along with a fit of the form $\frac{a \sin\phi}{b + c\cos\phi}$ and an estimation using the VGG double distribution model [36]. Including more terms of the harmonic expansion from [19] was not necessary to obtain good quality fits, as expected. The parameter a in the fit is the best estimate of the asymmetry at 90° and is represented in Figure 30 for all (x, Q^2) bins as a function of $-t$. Model predictions using Double-distribution VGG model with twist-2 only contribution or including limited twist-3 terms are shown on the same figure (blue solid and dashed curves). They tend to over-estimate the data especially at low values of t for small x_B and Q^2. A meson-exchange description [56] was also attempted for a few bins (black dashed lines) and seems to be in fair agreement with the data.

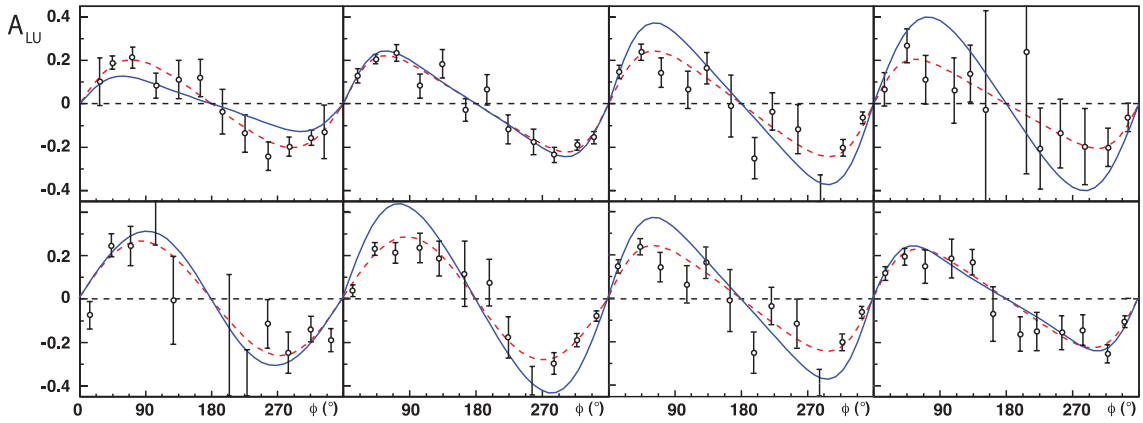

FIG. 29: Beam Spin Asymmetries as a function of ϕ for 8 selected (x_B, Q^2, t) bins. Top plots, are at fixed $< -t >$=0.5 GeV^2 and (x_B, Q^2) from left to right : (0.169, 1.36), (0.242, 1.78), (0.340, 2.25), (0.430, 2.77). Bottom plots are at fixed $< x_B >$= 0.35 and $< Q^2 >$= 2.5 GeV^2 with $< -t >$ from left to right : 0.015, 0.3, 0.5, 0.8 GeV^2. A fit of the form $\frac{a \sin\phi}{b + c\cos\phi}$ is shown as a red dashed curve. An estimation using VGG [36] is also shown as a blue curve.

Similarly to the Hall A data, a GPD extraction has been attempted later on by several groups and we will present a summary of this work in the next chapter.

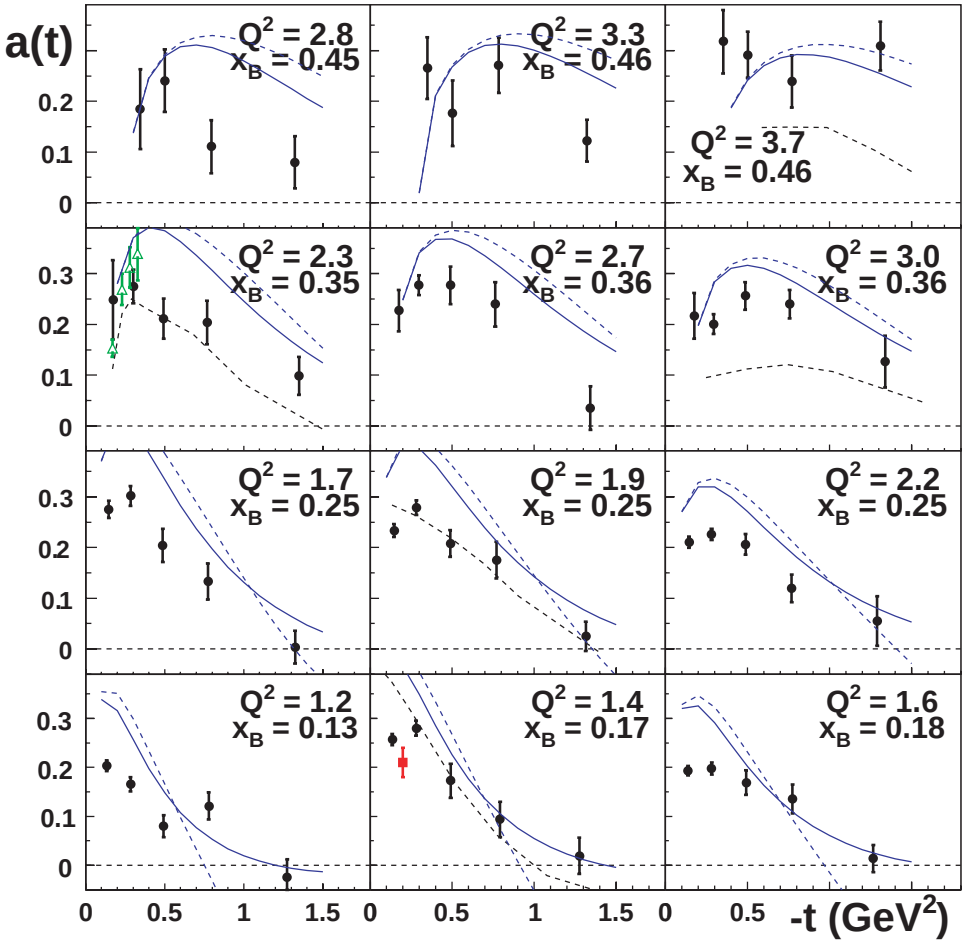

FIG. 30: Beam spin asymmetry at 90° (corresponding to the fit parameter a explained in the text) as a function of $-t$ for all (x_B, Q^2) bins (black circles). Data from Hall A turned into an asymmetry is shown as green triangles in a bin with similar kinematics, showing a reasonable agreement. The early measurement from CLAS described in the previous section is shown as a red square in the bin corresponding to the average kinematics. The phase space for this early measurement corresponds to the fully integrated CLAS acceptance, unlike the newer measurement, which probably explains the small disagreement. The VGG estimation is shown for twist-2 only (solid blue curve) or including some kinematical twist-3 contribution (dashed blue curve). The meson-exchange description from Laget was also attempted for a few bins (black dashed lines) and seems to be in fair agreement with the data

E. Transverse target DVCS : A 6 GeV proposal

The last 6 GeV experiment was proposed and accepted with rating A at PAC33 at Jefferson Lab, hopefully running in 2011 in Hall B. The idea is to study the spin azimuthal asymmetries in Deeply Virtual Compton Scattering using the CEBAF 6 GeV polarized electron beam, a transversely polarized HD-Ice target, and of course CLAS for the detection of the final state particles. The main focus of the experiment will be the measurement of the Transverse Target Single Spin Asymmetry (TTSA) in the reaction $ep^{\uparrow} \to ep\gamma$. Azimuthal moments in the cross section depend on different combinations of Generalized Parton Distributions and provide access to the elusive GPD E and the contributions of u and d quarks to the total orbital angular momentum, potentially in a much easier way than using quasi-free neutrons as in the Hall A E03-106 experiment. The expected asymmetries from the leading-order calculations are in the range of 20 to 40%, depending on the kinematics and on the GPD model used. The Q^2, x_B, and t dependences of the DVCS amplitude will be studied in a wide range of kinematics. In addition, transverse spin dependent double spin asymmetries (TDSA) for $\vec{e}p^{\uparrow} \to ep\gamma$ will be measured simultaneously, giving access to the real part of the target spin dependent DVCS amplitude.

1. Introduction

For this specific experiment, one needs to go back to some phenomenological description of the observables since only the longitudinal case was described in the theoretical introduction.

Target spin asymmetry

The Transverse Target Spin Asymmetry, or TTSA, arising from interference of DVCS and Bethe-Heitler is sensitive to twist-2 GPDs and its azimuthal dependence is given by a combination of different harmonics of ϕ and ϕ_S (see Fig.3), giving access to imaginary and real parts of corresponding Compton Form Factors $\mathcal{H}, E, \widetilde{\mathcal{H}}, \widetilde{\mathcal{E}}$ (CFFs). The separation of the different combinations of azimuthal moments in ϕ and ϕ_S appearing in the cross section requires a 2-dimensional analysis of moments in the ϕ and ϕ_S plane. This makes the transverse target data analysis very different from simple $\sin\phi$ moment extractions used for Single Spin Asymmetry studies in DVCS with unpolarized and longitudinally polarized

targets. Different observable asymmetries proposed to access GPDs include $A_{\mathrm{UT_x}}(\phi)$ and $A_{\mathrm{UT_y}}(\phi)$ (VGG [57]) or $A_{\mathrm{UT}}^{\sin(\phi_S-\phi)cos(\phi)}$ and $A_{\mathrm{UT}}^{\sin(\phi_S-\phi)\sin(\phi)}$ (BMK [19]) which are in first approximation linear functions of CFFs with a dominant contribution from Im$\mathcal{H}$ and Im$\mathcal{E}$, and from Im$\widetilde{\mathcal{E}}$ and Im$\widetilde{\mathcal{H}}$, respectively, along the lines $x = \pm\xi$ [58].

Two different sets of parameterizations were used to make predictions for expected effects. In order to constrain the GPDs, the transverse polarization component of the interference term, $\mathcal{I}_{TP}$, has to be singled out. This can be accomplished by forming the transverse (T) target-spin asymmetry with unpolarized (U) beam:

$$\begin{aligned} A_{UT}(\phi_S-\phi) = & \frac{d\sigma(\phi_S-\phi)-d\sigma(\phi_S-\phi+\pi)}{d\sigma(\phi_S-\phi)+d\sigma(\phi_S-\phi+\pi)} \\ \simeq & \quad A_{UT}^{\sin(\phi_S-\phi)\cos\phi}\cdot\sin(\phi_S-\phi)\cos\phi \\ & +A_{UT}^{\cos(\phi_S-\phi)\sin\phi}\cdot\cos(\phi_S-\phi)\sin\phi. \end{aligned} \tag{50}$$

The projections for $A_{UT}^{\sin(\phi_S-\phi)\cos\phi}$ and $A_{UT}^{\cos(\phi_S-\phi)\sin\phi}$ are calculated for different values of the total angular momentum J_u. Since the contributions of u and d quark are proportional to the corresponding squared charge, the d quark contribution is suppressed.

Variations in the parameter settings for the GPD E become manifest in $A_{UT}^{\sin(\phi_S-\phi)\cos\phi}$ while $A_{UT}^{\cos(\phi_S-\phi)\sin\phi}$ shows only minor modifications. In projection plots for simplicity the symbol A_{UT} is used for $A_{UT}^{\sin(\phi_S-\phi)\cos\phi}$ defined as:

$$A_{UT}^{\sin(\phi_S-\phi)\cos\phi} = \frac{1}{\pi}\int_0^{2\pi} d\phi\cos\phi A_{UT}^{\sin(\phi_S-\phi)}(\phi). \tag{51}$$

Figures 31 and 32 show the asymmetry for proton, neutron targets respectively, plotted as a function of contributions of u and d quarks to the orbital angular momentum (J_u, J_d) calculated using the Dual parameterization of GPDs H and E from Ref. [39].

Using both Regge and factorized ansätze, the asymmetries are calculated for different possible cases. Calculations show very significant variations of azimuthal distributions on the values of J_u and J_d. Within these model calculations $A_{UT}^{\sin(\phi_S-\phi)\cos\phi}$ turns out to be sizable even when the calculation is done for $E^q = 0$. Thus a solid knowledge about the GPD H^u is needed in order to constrain J_u. The model parameters for the GPD H^u, can be well constrained by the dedicated DVCS measurements at CLAS and Hall A, using an unpolarized and longitudinally polarized hydrogen targets. Since in addition the profile parameters are assumed to be the same for the GPD E^u, the only remaining free parameter

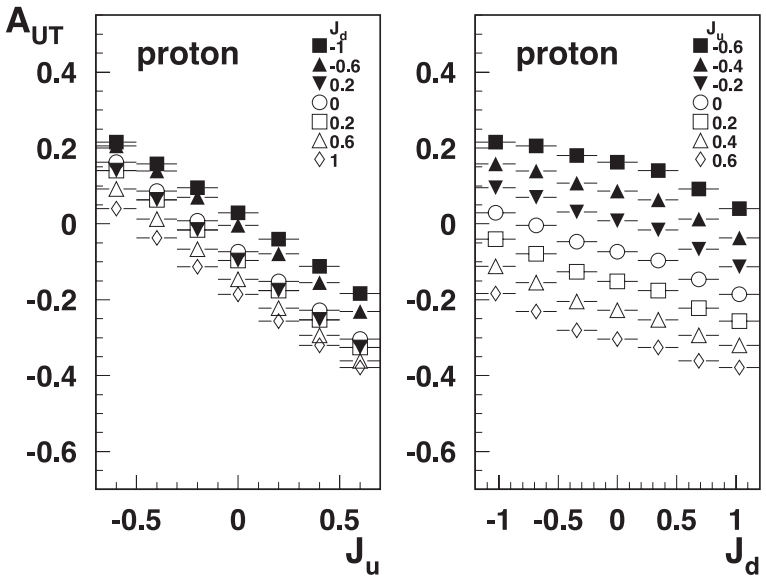

FIG. 31: The $A_{UT}^{\cos\phi}$ for a proton target for different values of J_u and J_d ($x = 0.35$,$Q^2 = 2.5$, $t = -0.55$).

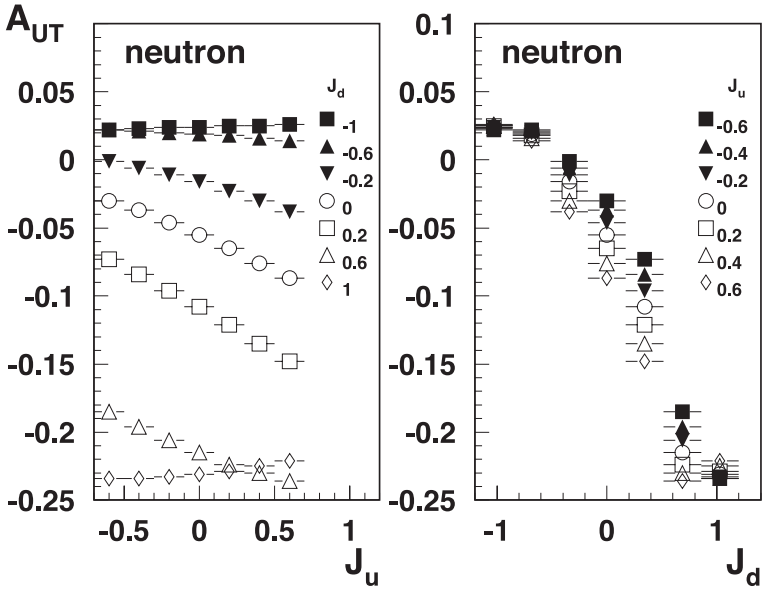

FIG. 32: The $A_{UT}^{\cos\phi}$ for a neutron target for different values of J_u and J_d ($x = 0.35$,$Q^2 = 2.0$, $t = -0.55$).

is J_u. Hence the projected measurement of $A_{UT}^{\sin(\phi_S-\phi)\cos\phi}$ has a clear potential to constrain J_u, as can be seen from Figures 31 - 32.

At our typical kinematics ($x_B \approx 0.3$), A_{UT} has sensitivity to all four GPDs and therefore, combined with unpolarized and longitudinally polarized DVCS asymmetries will provide a

complete set of measurements to extract different contributions.

The projection curves for CLAS running with a transversely polarized target have been calculated assuming a luminosity of $5 \times 10^{33}\text{cm}^{-2}\text{s}^{-1}$, with a HD-Ice target polarization of 75% for hydrogen and 25% for deuterium with 25 days of data taking.

DVCS Transverse Target Spin Asymmetry measurements in addition to Beam Spin Asymmetries from unpolarized target [54] and longitudinally polarized Target Spin Asymmetry measurements will provide a large set of data needed for the extraction of CFFs and corresponding GPDs. A_{UT} is especially sensitive to the GPD E, and as such will constrain any extraction of the angular momentum J.

Double spin asymmetry

With the use of a polarized electron beam, this experiment will also determine the double spin asymmetry A_{LT}. Certain moments of the TTSA will provide also access to real part of CFFs, the double spin asymmetries, however provide more variety of observables sensitive to the real part of corresponding CFFs. At twist-2 level, this observable takes the form:

$$A_{\text{LT}}(\phi) \sim \frac{c_{0,\text{TP}}^{\text{BH}} + c_{0,\text{TP}}^{\mathcal{I}} + (c_{1,\text{TP}}^{\text{BH}} + c_{1,\text{TP}}^{\mathcal{I}})\cos(\phi) + (s_{1,\text{TP}}^{\text{BH}} + s_{1,\text{TP}}^{\mathcal{I}})\sin(\phi)}{c_{0,\text{unp}}^{\text{BH}} + ...} \tag{52}$$

As in the case of A_{UT}, more interesting object is the $\sin(\phi_S - \phi)$ moment of the asymmetry $A_{LT}^{\sin(\phi_S-\phi)}(\phi)$ defined as,

$$A_{LT}^{\sin(\phi_S-\phi)\sin\phi} = \frac{1}{\pi}\int_0^{2\pi} d\phi \sin\phi A_{LT}^{\sin(\phi_S-\phi)}(\phi) \tag{53}$$

The A_{LT} (used for simplicity in projection plots) exhibits a measurable sensitivity to Re$\mathcal{H}$ and Re$\mathcal{E}$. Measurements with both beam and target polarized provides a unique possibility to access real parts of CFFs through measurements of spin asymmetries.

The polarized electron beam is also needed for the measurement of the target polarization through $\vec{e}p^{\uparrow}$ elastic scattering. Unlike A_{LU}, the Bethe-Heitler process alone can generate a double spin asymmetry A_{LT}.

2. Experimental Setup

The CLAS spectrometer will be used in its standard configuration, but with a transversely polarized target and a mini-torus for low-energy Møller deflection, which prevents the use

of the inner calorimeter for this experiment.

The strong holding fields accompanying transversely polarized target employing dynamical polarization methods can deflect the electron beam and create challenging background conditions. A magnetic chicane is typically being installed upstream of the target and arranged in such a way that the target's magnetic field bends the electron beam back on axis [59]. However, bremsstrahlung created in the target material will be peaked along the direction of the incoming electrons, which will then be at several degrees to the detector axis depending on the holding field.

Generally, one can arrange to have either the electron beam or the target bremsstrahlung centered at 0°, but not both. A transversely polarized target in a frozen-spin state, such as the HD-Ice target, requires only small holding fields, and greatly mitigates such background problems. Problems associated with beam deflection are virtually eliminated by the small holding fields and this potentially allows the target to be located even in the center of the detector, thus dramatically increasing the acceptance. In addition, the HD-Ice target has almost no dilution compared to standard solid state targets. The HD-ice target and its cryostat which will be inserted inside the mini-torus and CLAS are shown on Figure 33. A typical DVCS event using CLAS and the HD-ice target as shown on Figure 34 (left). The right figure shows the effect of the mini-torus on the Møller background.

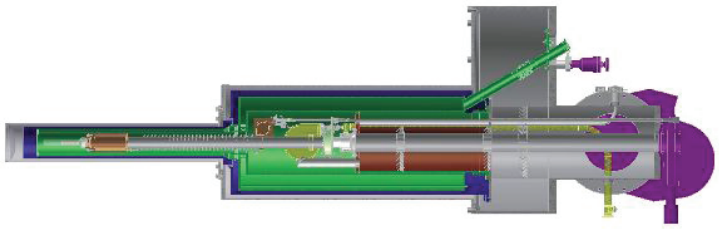

FIG. 33: CAD view of the HD-ice target cryostat which will be inserted inside CLAS.

The composition for a 4 cm HD-Ice target is shown in Table III E 2. The only unpolarizable nucleons are associated with the target cell and these can be sampled and subtracted in conventionally empty-cell measurements. At the same time, the low-Z results in a long radiation length and comparatively few bremsstrahlung photons.

The HD-Ice target was developed at LEGS in Brookhaven and now migrated from BNL to JLab. It has been used quite successfully in photon beam experiments. The factors

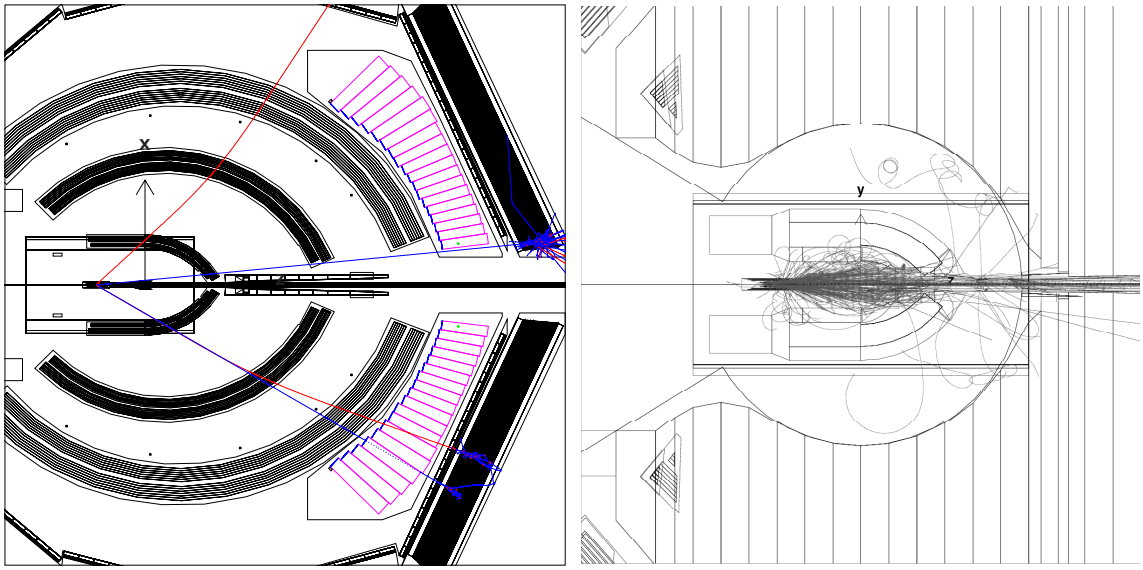

FIG. 34: CLAS setup with HD-Ice target positioned at -70 cm. Minitorus positioned at -50 cm. A single DVCS event shown in CLAS (left) and Møller electrons in the field of the minitorus (right)

Material	gm/cm^2	mass fraction (%)
HD	0.735	77%
Al	0.155	16%
C_2ClF_3	0.065	7%

TABLE I: List of HD-Ice material.

affecting target polarization are complex and intertwined; a direct test of the performance of polarized HD with electrons is essential and is planned during the course of the E06-101 run [60] in 2011.

3. Data analysis principle

The event selection will be similar as the one described for the previous 6 GeV experiment except for the absence of the inner calorimeter. While the electron and proton detection efficiencies are fairly large, the $ep\gamma$ events will be fully reconstructed only $\sim 30\%$ of cases, which would severely limit the statistical accuracy of our measurement. The epX provides the largest sample and is used in most of the projected results later on. The $ep\gamma$ provides the cleanest sample and will be used to check the epX extraction and contamination.

In any case, even though the missing mass resolution achieved in CLAS with HD-Ice target will be significantly better that for dedicated DVCS experiment using the solenoid magnet or the polarized target magnet, it will not be sufficient to separate $ep\gamma$ and $ep\pi^0$ final states event-by-event as shown before on Figure 7. A simulation will be used to estimate the contamination from π^0. Three different samples of events, epX, $ep\gamma$ and $ep\gamma\gamma$ will be analyzed to separate exclusive $ep\pi^0$ events from DVCS events. It was demonstrated that DVCS asymmetries extracted from the CLAS E1-F and E1-6 data sets ($E_{\rm beam} \approx 5.7$GeV) where only epX events were detected, were consistent both with $ep\gamma$ events from the same data sets and also with $ep\gamma$ data set from the dedicated DVCS experiment described in the previous chapter, where all 3 final state particles were detected.

4. Projected results

The measurements with transversely polarized target offer a variety of observables sensitive to different combinations of GPDs. The wide phase space coverage of CLAS will allow us to separate observables in different bins of the relevant kinematic variable. We will only show part of the expected results. The corresponding projections based on 25 days of HD data taking are shown on Figure 35 for the proton TTSA and on Figure 36 for the proton and neutron TDSA, for a few different values of the total quark angular momenta J_u and J_d.

High precision data over a large phase space will allow us to constrain the Compton Form Factors and therefore the GPDs, especially the GPD E, in a unique way. The extraction procedure for the quark angular momenta will not be based on the model-dependent fits to data as done for E03-106 and shown for illustration and estimation in our projected results here. We actually expect that the global fit procedures which are emerging, outlined in section V, will be able to fit this set of transversely polarized data with the rest of the world data and extract the J_q's in a much less model-dependent way.

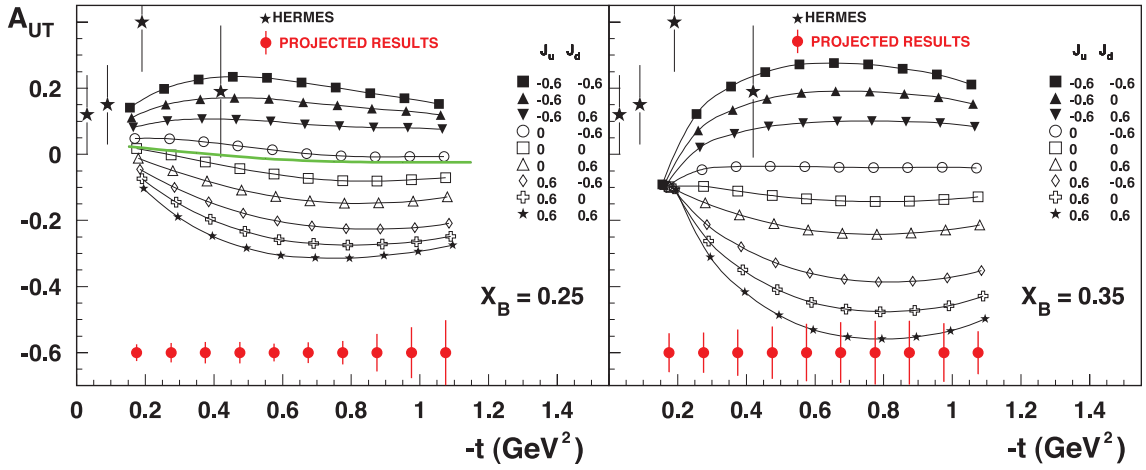

FIG. 35: Expected DVCS TTSA amplitudes $A_{UT}^{\sin(\phi-\phi_S)\cos\phi}$ as a function of $-t$, as predicted by the dual parameterization for GPDs H and E [39] ($\widetilde{\mathcal{H}} = \widetilde{\mathcal{E}} = 0$). The projected statistical error for 25 days with hydrogen polarization 75% (2 bins in x_B and Q^2) is shown in red. The green solid line on the left plot corresponds to the case E=0. The systematic error is expected to not exceed the statistical one.

IV. DVCS AT 11 GEV WITH CLAS12

The upgrade of the CEBAF electron accelerator to 12 GeV is a unique opportunity to extend the DVCS measurements performed at 6 GeV in a much larger kinematical domain, especially providing higher average Q^2 data at any x_B bin. This accelerator upgrade is highly cost-effective as it will re-use many of CEBAF6 components, adding only 10 cryo-modules and refurbishing the old ones to bring the energy to the desired level. The tunnels of the recirculating arcs were initially designed to accomodate 24 GeV beam, well above the requirements for 12 GeV so only the magnets and their power supplies need to be upgraded. The 5-pass beam accounts to about 11 GeV and will be brought to the three old experimental Halls A, B and C, whereas an extra half-pass will provide the new Hall D with up to 12 GeV electrons. All the old experimental halls will also be upgraded to accomodate the higher beam energy. Overall, the upgrade of Jefferson Lab will cost 310 million dollars and will be completed in 2014, according to schedule.

In Hall B, the CEBAF Large Acceptance Spectrometer (CLAS), which was designed to study multi-particle, exclusive reactions with its combination of large acceptance and moderate momentum resolution, will be upgraded to CLAS12 and officially optimized for

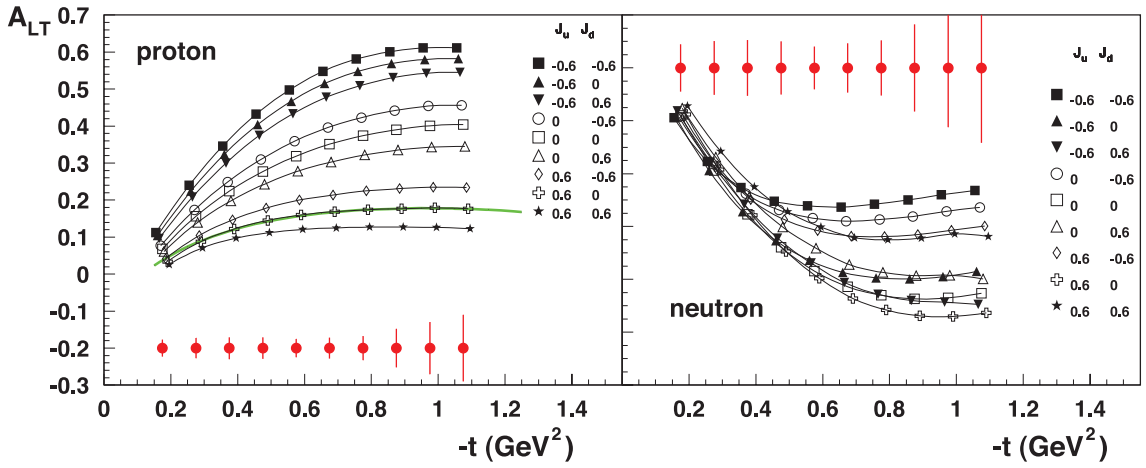

FIG. 36: Expected DVCS TDSA amplitudes A_{LT} as a function of t, as predicted by the dual parameterization for GPDs H and E [39]. The projected statistical error for transversely polarized hydrogen (left) and neutron (right), assuming 75% hydrogen polarization and 25% deuteron polarization. The green solid line on the left plot corresponds to the case E=0. The systematic error is expected to not exceed the statistical one.

studying exclusive and semi-inclusive reactions, emphasizing the investigation of Generalized Parton Distributions and Transverse Momentum Dependent Parton Distributions at higher energy. It will also be used for selected valence quark structure studies involving neutron "tagging" or polarized targets capable of supporting only very low beam current. Most importantly, the maximum luminosity will be upgraded from 10^{34} to more than 10^{35} cm^{-2}s^{-1} .

The Jefferson Lab PAC started calling for proposals rather early on in order to select a few high-profile experiments to be run as soon as the accelerator and the experimental halls would be ready. Our proposal to measure DVCS and access GPDs with polarized and unpolarized targets at 11 GeV beam was accepted by the PAC30 as one of the key experiments to be run when the upgrade is complete.

In the following sections, I will briefly describe the upgrades planned on the spectrometer and the physics output expected from these experiments. The physics motivation is actually common with the 6 GeV DVCS experiment which was already discussed earlier in this document. Finally, I will describe the event selection and analysis as well as projected results.

A. CLAS12

CLAS12 makes use of many existing detector components. Major new components include the superconducting torus coils that cover only the forward angle range, a new gas Cerenkov counter for electron/pion separation, additions to the electromagnetic calorimeters for better π^0 separation, and the central detector, which is a completely new piece of equipement. A schematic of CLAS12 is presented on Figure 37.

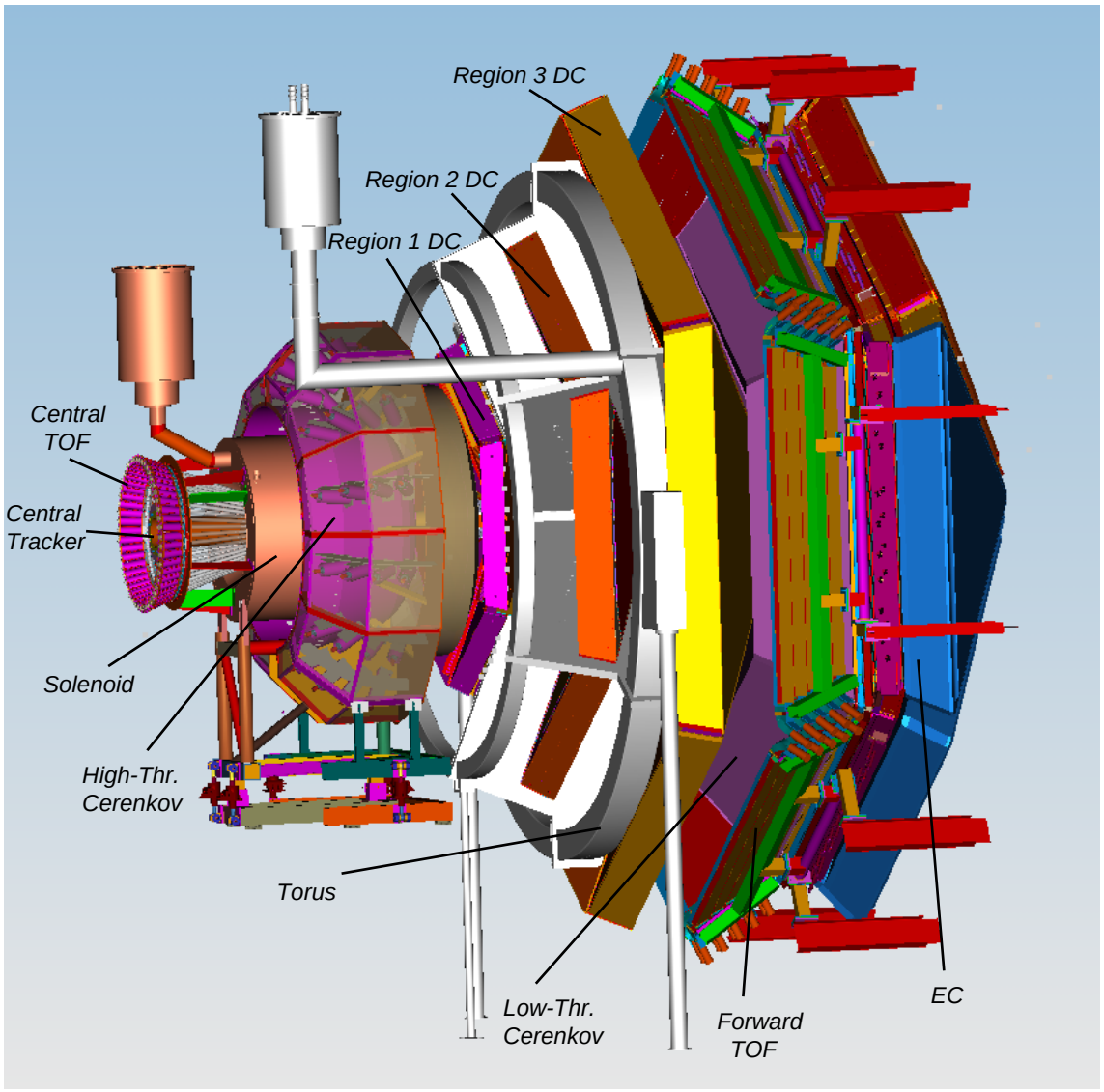

FIG. 37: Schematic of the CLAS12 spectrometer showing the various components.

The Forward detector

The forward detector system will use several of the existing components: the low threshold gas Cerenkov counters, all electromagnetic calorimeters, and the time-of-flight scintillators. New components include the high threshold Cerenkov counter, the torus magnet, and the forward drift chambers, which will cover an angle range from 5 to 40°. The large drift chambers in CLAS will be replaced by smaller ones that will cover the smaller angular range. Two of the existing detector systems, the time-of-flight system and the electromagnetic calorimeter system, need some upgrading to allow measurement of high momentum forward going particles. A pre-shower detector will be inserted in front of the existing CLAS electromagnetic calorimeters to allow high energy photon detection and separation of single photons from π^0 events. Improved particle identification will be accomplished by several means: the timing resolution of the scintillation counters will be improved by adding an additional layer of scintillators with 1/3 of the width of the existing layer and by using PMTs with better timing characteristics. The Inner Calorimeter used during the 6 GeV DVCS experiment can be re-used, but its location may not be closer than 1.75 m away from the target as shown on Figure 38 because of the high threshold Cerenkov counter, and therefore reduces its angle coverage and its use. Alternatively, one may consider using the IC closer to the target and removing the Cerenkov counter. This would be at the expense of electron/pion separation at high momentum and has not been studied in the proposal.

The Central detector

The Central Detector is built around a compact superconducting solenoid magnet, which has a triple function: it provides magnetic shielding of all tracking detectors from charged electromagnetic background, mostly Møller electrons and particles from secondary interactions. It provides the magnetic field for the momentum analysis of charged particles at large angles, and it provides the very uniform 5 T field needed for the operation of a dynamically polarized solid state target. The Central Detector will detect charged particles from 35 to 125°. Three layers of silicon strip sensors plus three layers of cylindrical Micromegas detectors will provide momentum analysis [61]. Particle identification is achieved by the combination of momentum analysis and time-of-flight measurements in the scintillation counters. A schematic of the central detector is shown on Figure 39.

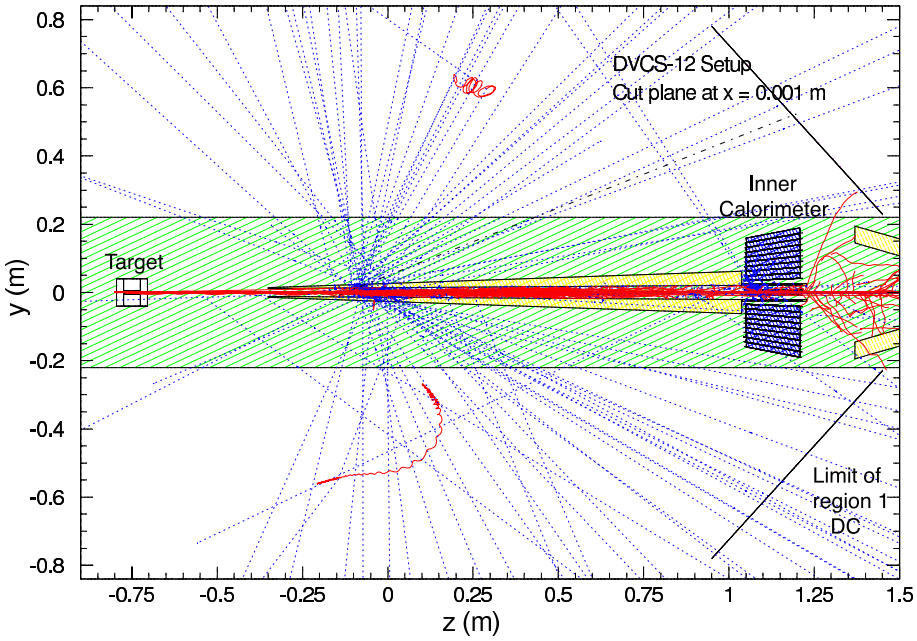

FIG. 38: Cut view of the target area along with the Inner Calorimeter (IC) and its shielding. Electron scattering events and in particular, the effect of Møller scattering on the IC and the shielding optimization can be studied through such simulations.

The beamline and targets

Most of the existing beamline components will be re-used without changes. As for targets, the liquid hydrogen target used for the unpolarized target part of the proposal (and many others) will also stay the same as for the 6 GeV running. However, the experiment to measure the longitudinal target spin asymmetry described in this document requires the use of a polarized solid state target, which is a part of the CLAS12 base equipment and described in the next section.

B. The polarized NH_3 target

The target will be polarized via the method of Dynamic Nuclear Polarization (DNP) which is a well established technique that has been used extensively in nuclear and particle physics experiments, including the ones performed in Hall B of Jefferson Lab. This technique typically achieves proton polarization of $80 - 90\%$. The nucleons in the target will be polarized longitudinally either parallel or anti-parallel to the electron beam direction.

The main systems required for realization of DNP are the superconducting magnet to pro-

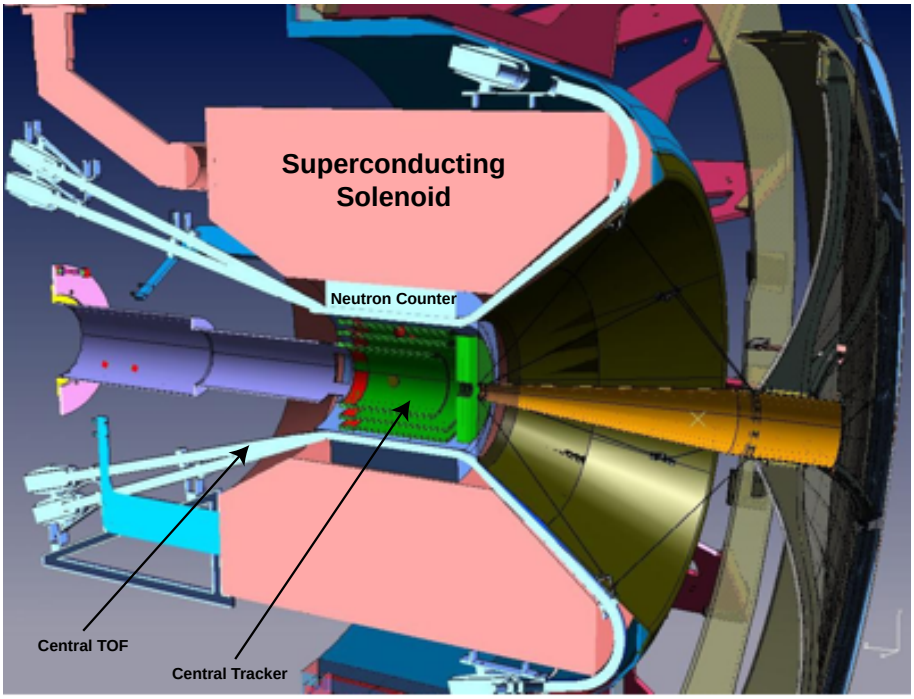

FIG. 39: Central Detector of CLAS12, composed of its central tracker. Only the Micromegas trackers are shown in this schematic but three double-layers of Silicon Vertex Trackers are also present between the target and the Micromegas trackers.

vide a strong (5 T) field, a ^{4}He evaporation refrigerator to maintain target material at $\sim$1 K, a target insert which will house the target material and some additional instrumentation, a microwave system to transfer the polarization to nucleon spins and a Nuclear Magnetic Resonance (NMR) system to determine the state of polarization. In CLAS12 the polarizing magnetic field will be provided by the superconducting solenoid of the central detector. This will allow us to use the polarized target without introducing any obstructions on the paths of the particles produced at the interaction point. It will also allow us to make a full use of the central detector, allowing for a wide coverage for particle detection, in particular the recoil nucleon for DVCS.

The target cryostat will house the evaporation refrigerator, the target insert and some instrumentation necessary for the microwave and NMR operations. The cryostat needs to be designed to allow its operation in a warm bore magnetic field. A conceptual design of the target cryostat is shown on Fig 40.

Other detector components will also be installed in the magnet bore, so that the central tracker will surround the target. The minimum outer diameter in the present design of

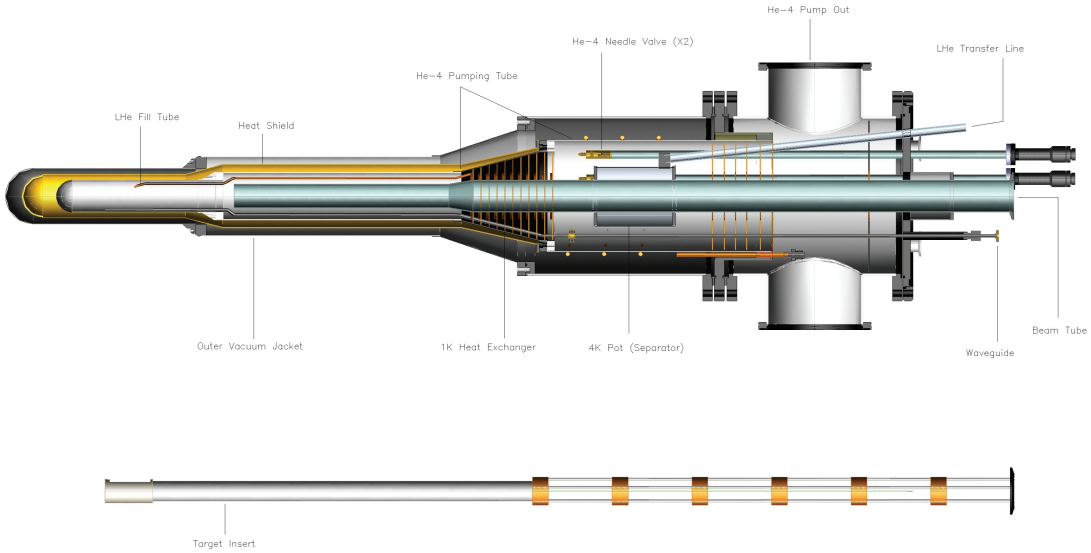

FIG. 40: A schematic drawing of the polarized solid target cryostat and the target insert for CLAS12.

evaporation chamber is 10 cm, which in the current state of design of the central tracker composed of Silicon and Micromegas layers, imposes strong contraints on the space left for 6 such detectors. This "target" volume will contain the outer vacuum space, heat shield and the evaporation chamber. The target material will be placed in a cell within a cup, with both containers made of hydrogen-free plastic. The cup will be attached to a thin aluminum structure that can be inserted through the beam tube. The schematic of the insert is shown on the bottom of Fig. 40.

Ammonia will be used as target material with the electron beam and CLAS12. This target offers high polarization, good resistance to radiation damage, and a relatively high ratio of polarizable nucleons per total number of nucleons. Ammonia can accumulate charges of $\sim 10^{15}$ electrons/cm^2 before showing signs of deterioration. Accumulated radiation damage can be mostly restored through the annealing process, in which target material is heated to temperatures of $80 - 90$ K for short periods of time. The interesting parameters of frozen ammonia are listed in Table II.

In order to determine the effective dilution factor D_{eff}, it will be necessary to collect data on the unpolarized material. A thin carbon target could be placed downstream in the same target cup for this purpose.

The target polarization will be monitored during the run via the NMR system in the field

Target Diameter	up to 30 mm
Target Length	up to 100 mm
Density	0.917 g/cm^3
Dilution Factor	3/18
Packing Factor	$\sim$ 0.62

TABLE II: Some parameters of the NH_3 targets.

of the solenoid magnet. The calibration of the proton NMR can be done by measurements of polarization in thermal equilibrium, taken with the polarizing magnet.

C. Event selection and data analysis

The event identification in CLAS12 will be accomplished in a similar way to our 6 GeV experiment E01-113 described earlier, using charged particle tracking in the torus and solenoid magnetic fields and time-of-flight systems in both forward and central detectors. Electrons will be separated from pions using the high-threshold Čerenkov counter and the forward electromagnetic calorimeter (EC). Protons will be identified using time-of-flight (SC/CTOF) and path length plus measured momentum (DC/central tracker). Photons will be detected in both the inner calorimeter (IC) and EC. As with the low energy data, only events with $W > 2$ GeV will be selected to avoid significant contributions from excitations of nucleon resonances.

One of the main problems encountered in the previous analyses of DVCS data is the background from π^0 production events, where π^0 decays into two photons and only one of them is detected. The relative amount of the π^0 contamination is expected to be small at lower values of $|t|$, and to increase with $|t|$.

In order to select single photon production events, we will once again detect all three particles in the final state, and require that there are no extra photons in the detector. Kinematical consistency cuts, such as missing energy/momentum cuts will be applied, similar to those used in E01-113 and described before. To estimate the effectiveness of these methods at 12 GeV beam energy a large number of single photon and π^0 events were simulated. The output of the event generator were processed with a fast Monte-Carlo program,

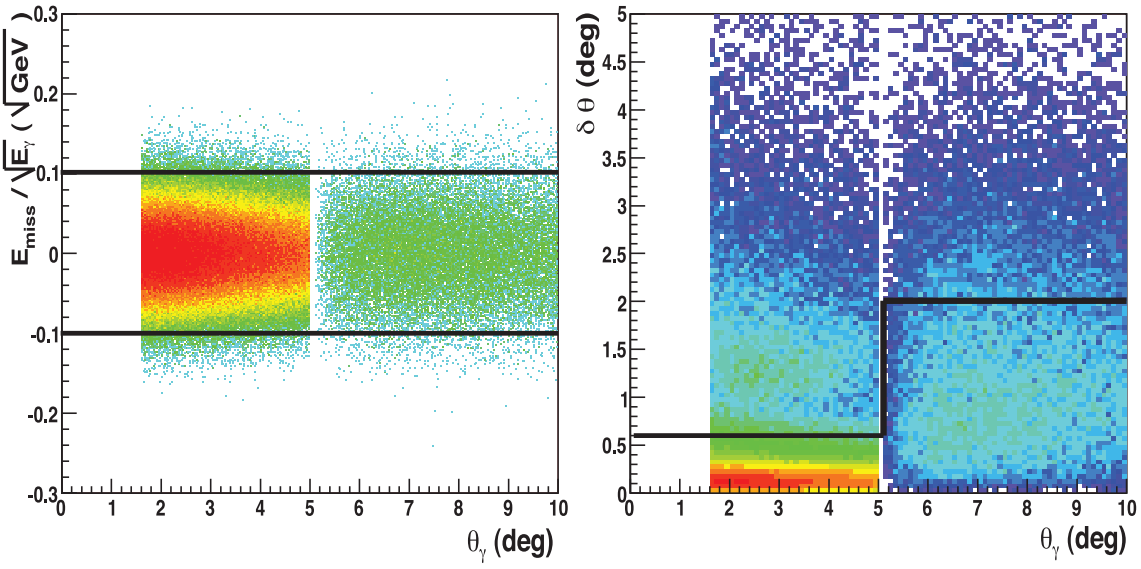

FIG. 41: Missing energy versus photon angle in the laboratory frame (left), and the angle between expected difference of photon and the angle of the detected photons versus photon angle (right). In each plot, the two loci correspond to IC and EC polar angle coverage. The black lines show the cuts applied to reduce pion contamination.

which simulates the response of the CLAS12 detector but doesn't include all the details. A cut on missing energy over measured photon energy $E_{miss} < 0.1\sqrt{E_\gamma}$, shown in Fig. 41, will allow for very few pion events in the data set without causing a large reduction of $ep \to ep\gamma$ events. Additionally, selecting only events within 0.6° and 2° cone around the expected direction of the photon, detected in IC or EC respectively, (see Fig. 41), will further reduce the single π^0 background. Using Monte-Carlo simulations we estimated that these two cuts will reduce the π^0 background on average by a factor of 10, while the number of the photon production events will decrease by approximately 20%. The simulations also indicate that after these cuts the pion contamination in some bins at $-t = 0.7$ can be up to 50% of the total number of events, while at small values of $-t = 0.1$ GeV^2 it is of the order of 1%. Note that even if the π^0 electroproduction did not produce asymmetries, the measured values would be diluted by the background events.

The strategy for accounting for the contribution of the remaining π^0 events into the spin asymmetries is to evaluate the amount of π^0 contamination, and subtract their contribution to the measured asymmetry. In the first step the π^0 yields and spin asymmetries will be measured using $\pi^0 \to \gamma\gamma$ decays, where both photons are detected in CLAS12. In the next

step, using Monte-Carlo simulations to calculate the acceptance ratio between 1-γ-detected and 2-γ-detected π^0 events, we can infer the number of π^0 production events in the (e, p, γ) data sample. This method is completely analog to the one used in the data analysis of the 6 GeV experiment. A similar technique was used with simulated events at 11 GeV electron beam energy, and the results are illustrated in Fig. 42. Note that the (Q^2, x_B, $-t$) bin shown on this figure is one of the worst cases of π^0 contaminations. The red circles show the target-spin asymmetries for pure DVCS/Bethe-Heitler event sample from the model [19] incorporated in the event generator [62] which was used in this study. After mixing in 26% of single π^0 electroproduction events the asymmetries are distorted, shown with green triangles. After accounting for these events by evaluating the single photon asymmetry in the π^0 data sample, and subtracting it from the "measured" asymmetry, we obtain the blue squares - the corrected values of the asymmetry, which are close to the original single photon asymmetry. The difference between the blue squares and the red circles indicate the expected uncertainties from the described procedure.

D. Projected results

The CLAS12 acceptance for $ep \to ep\gamma$ reaction was estimated using Monte-Carlo simulations. The event generator used to estimate the acceptance for the DVCS experiment is based on the GPD formalism described in Ref. [19]. Single photon electroproduction events at the beam energy 11 GeV were simulated in the $2 < Q^2 < 10$ GeV^2 range. These events were processed using our Fast Monte-Carlo code to simulate the CLAS12 detector response. This program represents a set of cuts in the coordinate and momentum space to represent the areas of the detector acceptance where the detection efficiency is expected to be close to unity. These cuts are combined with parameterizations of the detector response from various components of CLAS12. The efficiency of the active detector volumes is considered to be one.

CLAS12 is expected to run at a luminosity of $\mathcal{L} = 10^{35}$ cm^{-2}s^{-1}. The acceptance in (x_B, Q^2) might not always reduce to a simple rectangle depending on the considered bin, because of the limitation in the electron scattering angles, maximum energy and the requirement $W > 2$ GeV to exclude resonances from this study. The model used for the photon electroproduction cross section σ is a modified version of the VGG model [63], with

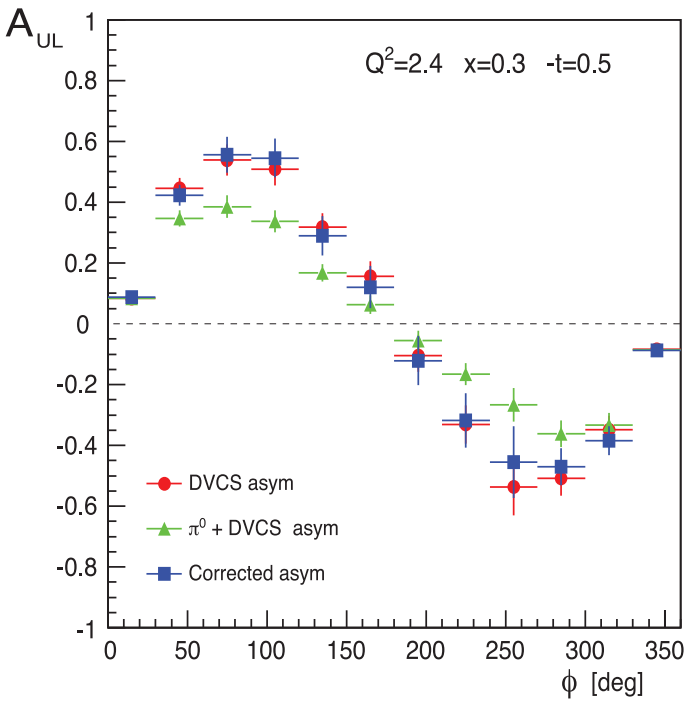

FIG. 42: Simulated target spin asymmetries for pure single photon data sample (red circles), data sample contaminated with π^0 events (green triangles), and asymmetries after subtracting π^0 contribution (blue squares). Error bars on these plot show the statistical uncertainties defined by the number of simulated events. This kinematic bin selected for this plot represents one of the highest possible π^0 contamination in our data sample.

a Regge-inspired ξ-dependence. The acceptance ranges from 0.1 to 0.5 depending on which bin is considered. As usual CLAS12 itself has a strong azimuthal angle dependence which translates directly in modulations in ϕ. Finally, the counting rates have been estimated for 80 days of 85%-polarized beam on target.

Figure 43 shows the binning in (x_B, Q^2) used to present the generated pseudo data. This binning is arbitrary and as is clearly seen on the figure, does not take into account very low-x_B and high-x_B/high-Q^2 data, which is also of interest.

1. Beam Spin Asymmetry

Figure 44 shows the Beam Spin Asymmetry for the proposed (x_B, Q^2, t) bins. In addition there are 20 bins in ϕ and the results are integrated over ϕ_e. Note that $-t$ as high as 2 GeV^2 were generated, and high t are mostly contained in the last t bin which is therefore quite

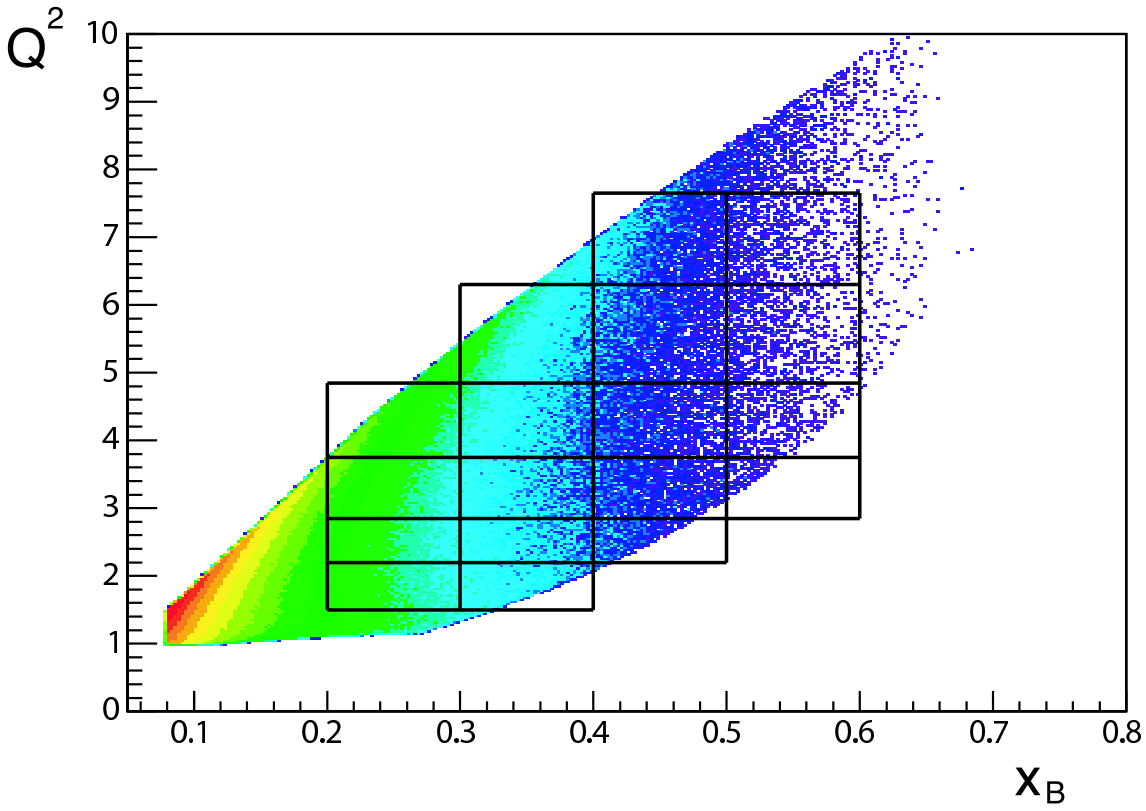

FIG. 43: Kinematical domain in (x_B, Q^2) of 11 GeV running with CLAS, with the conditions that $W > 2$ GeV to exclude resonance region. Also shown is the binning in x_B and Q^2 used to evaluate counting rates in this section.

wide. The error bars are purely statistical. The $\sin\phi$ harmonic extracted from this data will have a statistical error from 1% at low x_B and "low" Q^2 (lower left corner of the plot) up to 10% at the highest x_B and t (right section of the plot), which are of the same order of the planned systematic uncertainty of about 5% average.

Figure 45 is a detail of particular bins in our pseudo data sample, showing the statistical accuracy of the planned measurement along with different scenarios for a GPD model. The level of precision this proposal plans to achieve will be decisive for putting strong contraints on GPD parametrizations.

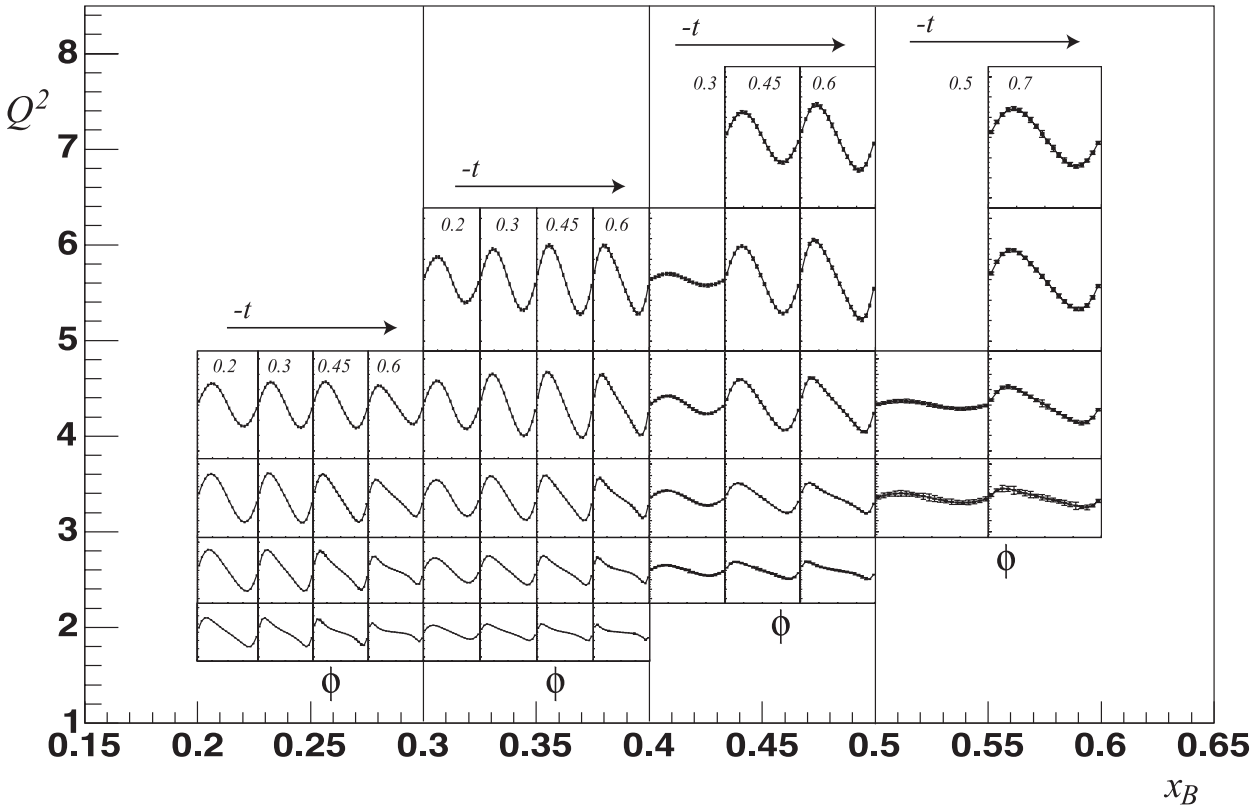

FIG. 44: Kinematical coverage of the beam spin asymmetry as a function of (x_B, Q^2, t). The outer horizontal scale corresponds to the x_B range, divided into 4 bins. The outer vertical scale represents the Q^2 range. Each individual histogram is the BSA (plotted between -0.7 and 0.7 in ordinate) as a function of ϕ (between 0 and 2π) for a given t-bin. The average value of $-t$ in the bin is shown in the upper part of each histogram. Only statistical errors are shown. Relative statistical accuracy on the $\sin\phi$ harmonic extends from 1% in the lower left section of this figure to 10% in the upper right section assuming 80 days of running at 10^{35} cm^{-2}s^{-1} luminosity.

2. Target Spin Asymmetry

The experimental target spin asymmetry is calculated as the ratio:

$$A_{UL} \equiv \frac{1}{P_T F} \frac{N^+ - N^-}{N^+ + N^-}, \tag{54}$$

where N^+ and N^- are the numbers of counts in each bin for positive and negative polarization of the target, P_T and F are the target polarization and dilution factor for the event sample, respectively. The effective polarization of the target will be extracted by measuring the double spin asymmetry from elastic electron scattering. The full simulations of this

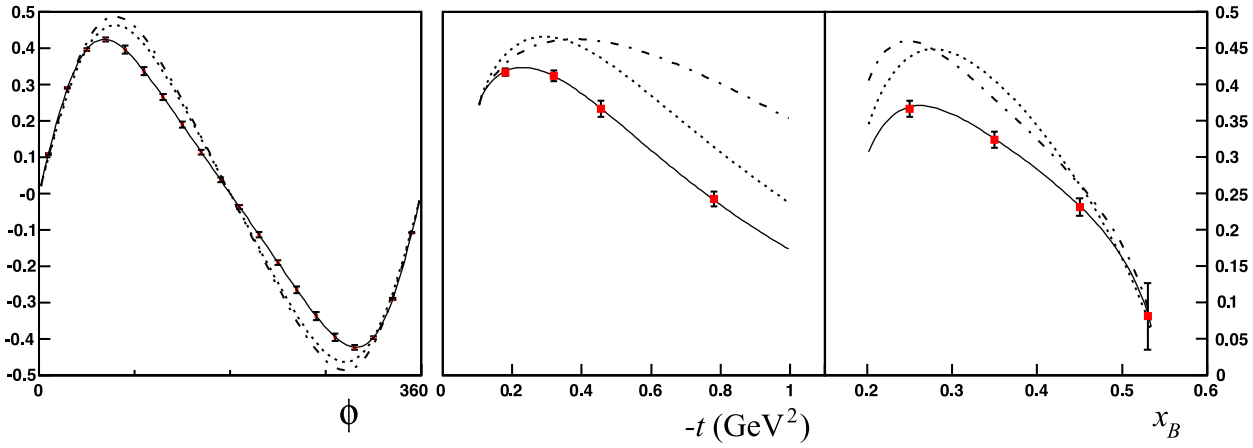

FIG. 45: On all figures: points in red represent projected data with statistical error bars. Lines are models with different input parameters, none of which includes twist-3 contributions: The full line is a model with a Regge-type t-dependence and D-term. The dotted line includes the Regge-type t-dependence but has no D-term. The dash-dotted line has the D-term but the t dependence only comes from form factors. Left figure: Beam spin asymmetry as a function of ϕ for $< x_B >= 0.2$, $< Q^2 >= 3.3$ GeV^2 and $< -t >= 0.45$ GeV^2. Middle figure: BSA as a function of $-t$ for $< x_B >= 0.2$, $< Q^2 >= 3.3$ GeV^2 and $\phi = 90°$. Right figure: BSA as a function of x_B for $t = 0.45$ GeV^2, $< Q^2 >= 3.3$ GeV^2 and $\phi = 90°$.

method with CLAS12 detector yield uncertainty on the product of beam and target polarizations $P_e \cdot P_T$ of about 1%. Therefore, the uncertainty on the target polarization will be dominated by the precision of the Møller polarimeter, which is estimated to be about 2%.

One of the main sources of the background events is the single photon production from the unpolarized nuclei in the target material. Such events will not produce target spin asymmetries, and therefore will only reduce the measured asymmetry by a dilution effect. This kind of background can be reduced using missing energy cuts, assuming an electron scattering process from a free proton. Due to Fermi-motion in the nuclei, the distribution of the components of the missing momentum are smeared around zero, and such a cut will significantly reduce the background from the nuclear target. A similar technique has been successfully used in the analysis of CLAS data [64], where a 2° cut was applied to the difference between expected angle for the photon and the measured photon. Data taken with a solid ^{12}C target will allow us to determine the dilution factor using a technique described in Ref. [64].

For the polarized target running, we assumed $\mathcal{L} = 2 \times 10^{35}$ cm^{-2} sec^{-1} instantaneous luminosity and a total number of 100 days of beam time on polarized ammonia. The factor of 2 increase for luminosity with respect to unpolarized runs can be achieved considering that nuclear targets, like NH_3, contain half the Møller scattering targets compared to liquid hydrogen, which is the limiting factor. The target polarization in this estimate was assumed to be $\sim 80\%$ which has been achieved routinely before.

The target spin asymmetries as a function of ϕ are shown on Figure 46. The values for the target asymmetries are calculated using a model which reasonably describes the existing CLAS data [57]. Clearly the statistical errors are small at small x_B, and the expected relative statistical uncertainty for $A_{UL}^{\sin\phi}$ is $\frac{\sigma_A}{A} \sim 2\%$. The statistical errors become larger in the high x_B region $x_b > 0.4$, and the expected relative uncertainty for extracted $A_{UL}^{\sin\phi}$ is $\frac{\sigma_A}{A} \sim 10\%$. Sample plots showing the sensitivity of the target-beam asymmetry measurement to $\widetilde{H}$ are presented in Fig. 47. The ϕ dependence of the target spin asymmetry at $Q^2 = 4.1$ GeV^2, $x_B = 0.36$ and $-t = 0.52$ GeV^2 is shown on Figure 47 (a). The black points show the values from Ref. [57] using CTEQ6 PDFs [65] with the projected statistical errors for the proposed measurement. The red solid curve is obtained using MRST02 PDFs [66] with $E = \widetilde{E} = 0$, and for the blue dashed curve $\widetilde{H}$ is set to zero as well. Figures 47 (b) and (c) show the $-t$ and x_B dependences of the $\sin\phi$ moments extracted by fitting the ϕ dependent histograms for target beam asymmetry with a function of the form $f(\phi) = \alpha \sin\phi + \beta \sin 2\phi + \gamma$. The error bars in these plots are defined by the statistical uncertainties in the corresponding ϕ dependent histograms. At the lower values of $-t$ and x_B the errors will be dominated by the systematics, while at higher $-t$ and x_B the statistical and systematic errors are expected to be of the same magnitude. The difference between the red solid curve and blue dashed curve is due to $\widetilde{H}$.

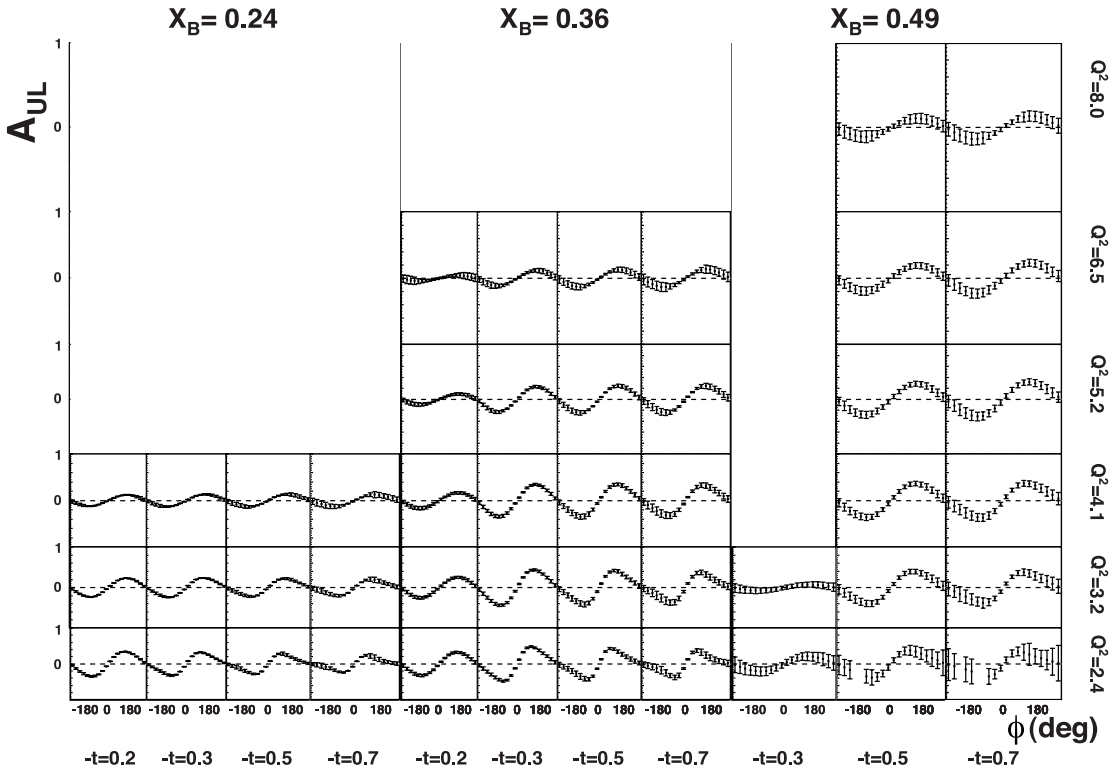

FIG. 46: Projected target spin asymmetry versus ϕ for different Q^2 and x_B and $-t$ values.The error bars represent the projected statistical uncertainties for the target spin asymmetry using the Monte-Carlo simulation. The asymmetry values are from Ref. [57].

V. WHAT DID WE LEARN FROM 6 GEV EXPERIMENTS ?

A. Is 6 GeV enough to gain insights on the proton structure through DVCS measurements?

Before arguing what type of GPD parametrization is more adequate to describe the DVCS data, it is essential to check if one is actually sensitive to the handbag diagram in the 6 GeV measurements performed at Jefferson Lab. In other words, the possibility to study GPDs through the virtual Compton diagram relies on the factorization theorem, similarly to the extraction of PDFs from DIS data. The factorization proof is actually very similar in both cases, and uses the fact that the incoming photon virtuality is large at fixed x_B and t. To

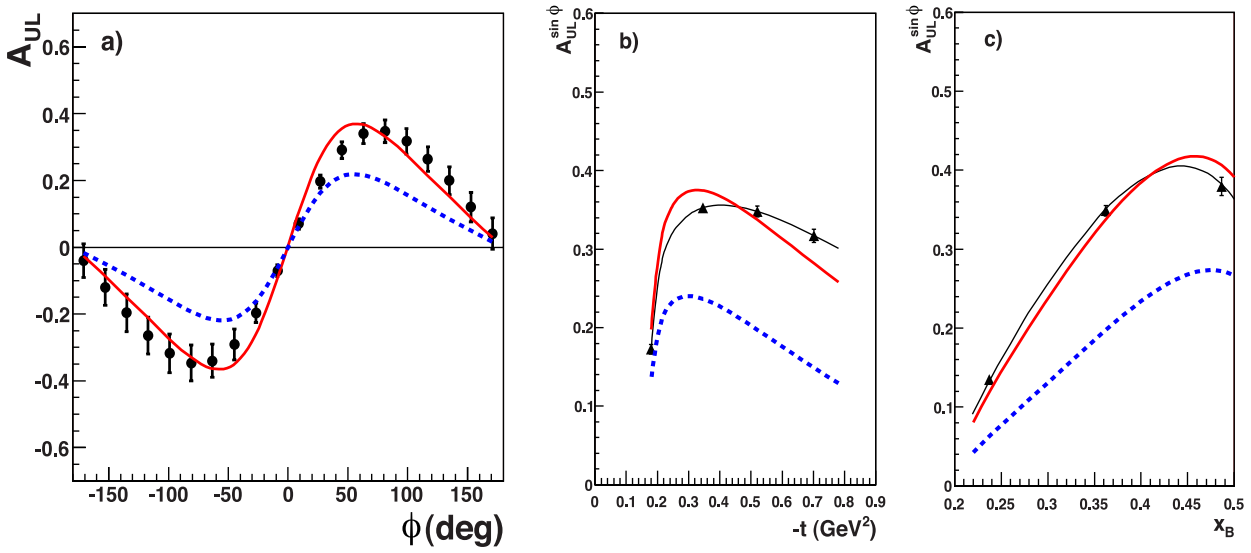

FIG. 47: Projected target spin asymmetry versus ϕ for $Q^2 = 4.1$ GeV^2, $x_B = 0.36$ and $-t = 0.52$ GeV^2 (a). The black points show the values from [57] using CTEQ6 PDFs with the estimated errors from the proposed measurement. The red solid curve is using MRST02 PDFs with $E = \widetilde{E} = 0$, and for the blue dashed curve $\widetilde{H}$ is also set to zero. $\sin\varphi$ moments of the target spin asymmetry versus $-t$ at $Q^2 = 4.1$ GeV^2 and $x_B = 0.36$ (b), and versus x_B at $Q^2 = 4.1$ GeV^2 and $-t = 0.52$ GeV^2 (c). The projected error bars represent the statistical uncertainties only.

continue the analogy with DIS, theorists cannot predict when the Q^2 is high enough in order to warrant an unbiased extraction of PDFs. However, all the structure function data down to 1 GeV^2 have been sucessfully analyzed in terms of PDFs using a NLO or NNLO QCD analysis through the DGLAP evolution formalism, as shown on Figure 48, taken from Ref. [67].

First of all, let us discuss the implications of the first DVCS asymmetries measured by CLAS (confirmed by HERMES) in 2000, described in section III A and shown on Figure 9. The important finding of this experiment was that the photon electroproduction asymmetry $A_{\rm LU}(\phi)$ was compatible with a $(a\sin\phi + b\sin 2\phi)$ behavior with b compatible with 0. This seems to indicate that an helicity conserving amplitude, which is actually the case with the leading twist handbag diagram, is sizeable, compared to twist-3 contributions. However, this is not an actual proof of the handbag dominance. For instance, the $\sin 2\phi$ contribution

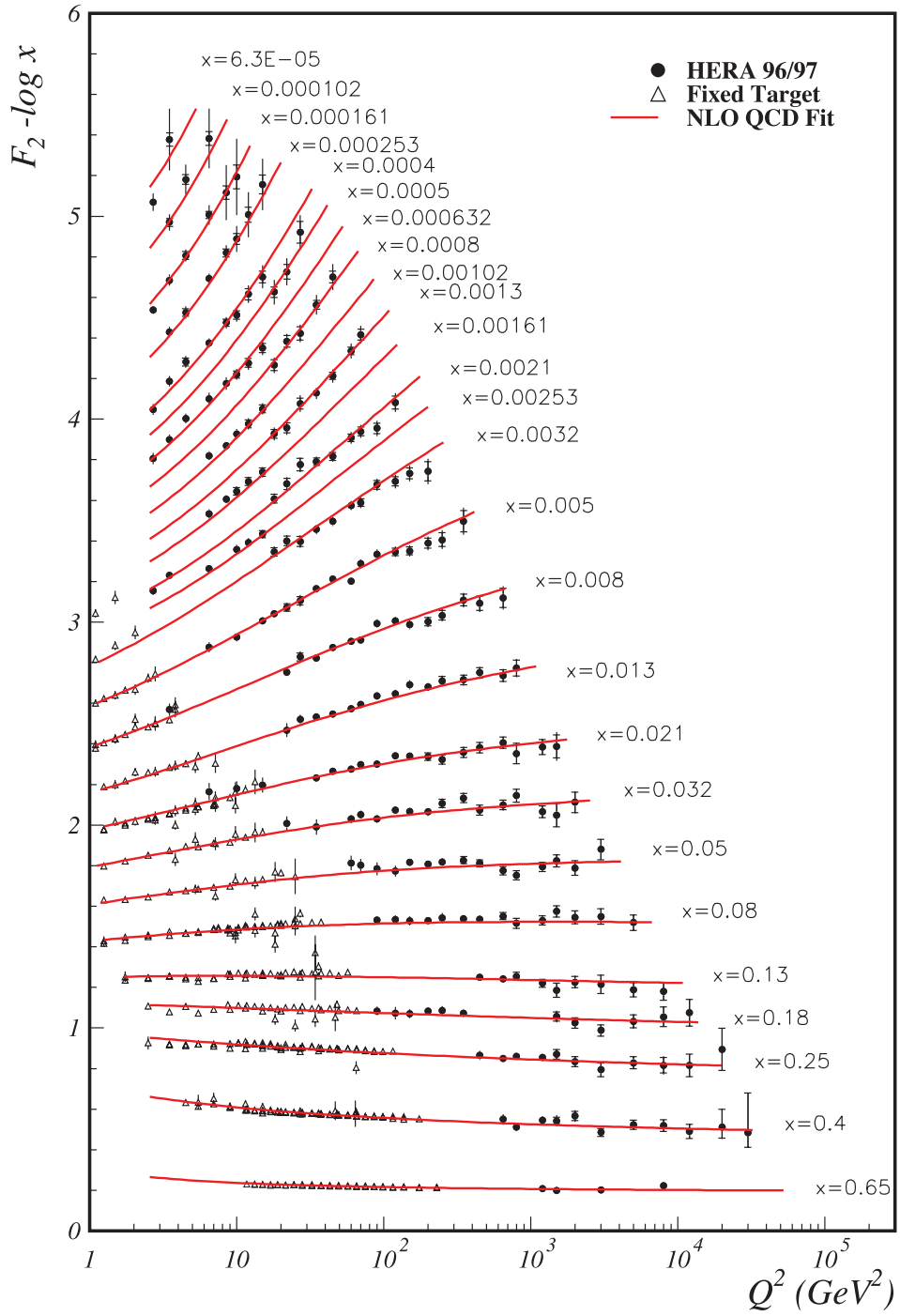

FIG. 48: Structure function F_2 data from various experiment along with NLO fit from QCD analysis, taken from [67], with fitted functions extended to Q^2=1 GeV^2 to compare with low Q^2 data.

should vanish not only in the Bjorken limit but also at $Q^2 \to 0$ limit as pointed out in [68]. The only way to actually prove that the leading twist contribution is dominant is to test the Q^2 dependence of the different amplitudes, or equivalently, of the a and b coefficients, with the caveat that in the asymmetry, there are unknowns both in the numerator and the denominator and the interference terms cannot be separated perfectly. In addition, the propagators in the numerator and denominator actually do not cancel out perfectly since they are integrated separately. It is therefore entirely possible to have extra contributions or cancellations happening between the numerator and denominator, which may give a "fake" indication of handbag dominance. The main conclusion from the first asymmetry data was that there is a strong hint of handbag dominance in the interference term at very moderate energy, and that this needed to be checked thoroughly with a measurement of the Q^2 behavior of the measured coefficients or helicity amplitudes. The VGG Double Distribution model is also shown on Figure 9 and over-estimates the data by a significant amount. This remark still remains after including some twist-3 effect estimated within the Wandzura-Wilczek (WW) approximation [19]. This is not unexpected considering such models have a large number of assumptions and parameters and that there are potentially larger power corrections which need to be applied. This "feature" of double distribution models, that they overestimate the interference-type DVCS observables, will remain for all data samples as we will see later on.

The Hall A experiment E00-110 measured the Q^2 dependences of the $\sin\phi$ and $\sin 2\phi$ contributions to the cross section difference for opposite electron helicities. As was said before, this is the only good way to check for the leading-twist dominance. As explained in III B, this measurement was carried out at "fixed" $x_B = 0.36$ for three values of Q^2=1.5, 1.9 and 2.3 GeV^2. As shown on Figure 19, there is no observed Q^2 dependence of the $\sin\phi$ and $\sin 2\phi$ coefficients once their expected Q^2 dependences in the BMK formulation have been removed. It is a further indication that the handbag diagram giving the leading twist contribution is dominant when looking at the interference term only. Once again, as for all such studies, the proof is not free of loopholes : Firstly, the kinematics are averaged over some acceptance as for any experimental determination, as shown on Figure 49. Even though the cross section extraction is done in a correct manner to integrate this acceptance, one may still have effects due to the x_B dependence of the observable within the acceptance. This is definitely not a unique issue for this experiment, and it actually has the most precise

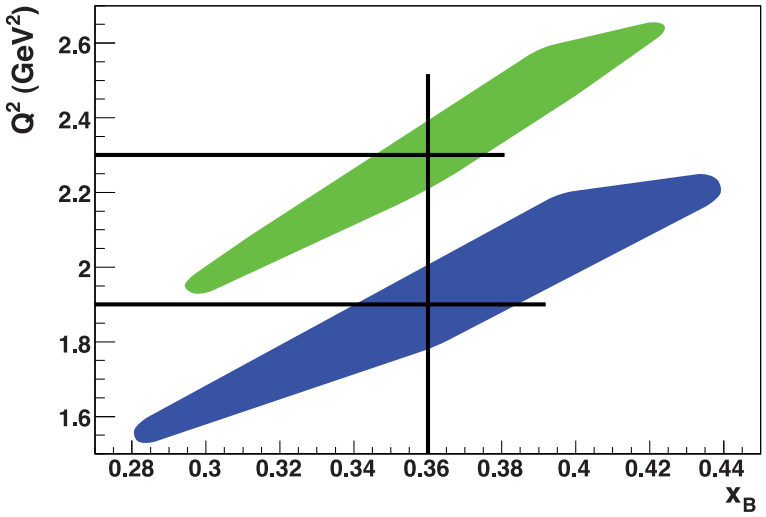

FIG. 49: Q^2 versus x_B acceptance for the two highest Q^2 settings of the Hall A E00-110 experiment. The average kinematic point is shown with the thick black lines.

kinematic settings of all the measurements on DVCS done at this point, but some unwanted systematic error may still sneak in. Secondly, the smaller Q^2 kinematic point has about half of its events under the usual DIS cut $W^2 > 4$ GeV^2. This is not a feature of the experiment but rather a consequence of the very small kinematical range which can be probed with a 6 GeV electron beam while retaining some lever arm in Q^2. In other words, there was no choice but to have this kinematical setting slightly in the uncomfortable zone. This Q^2 setting has its events always at $W^2 > 2.5$ GeV^2. However, as shown on Figure 50, at $Q^2 > 1$ GeV^2, the effect of resonances on the structure function F_1 is relatively limited and we would not expect a large effect for DVCS either.

Lastly, as pointed out before, the unambiguous extraction of the $s^I_{1,unp} = y(2-y)\mathrm{Im}\mathcal{C}^I$ coefficient in front of the $\sin\phi$ term in the cross section difference relies on the BMK formalism [19]. It was pointed out later that even though these complete analytic calculations performed for photon leptoproduction cross section were limited to twist-three accuracy, it also implied that only terms suppressed by a single power of the hard photon virtuality were kept in all analytical expressions, corresponding both to leptonic and hadronic parts of amplitudes [20]. This approximation is certainly reasonable for HERA kinematics but certainly not for fixed target experiments which all have average Q^2 in the few GeV^2 range

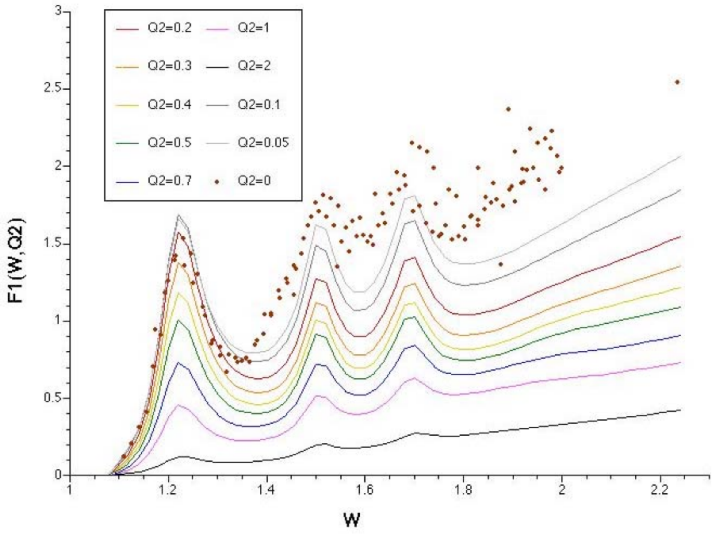

FIG. 50: Structure function F_1 as a function of W for different Q^2 settings. The resonance region is washed out by going to $Q^2 > 1$ GeV^2, which is where the lowest Q^2 setting of the Hall A E00-110 experiment is located.

at best. Some estimates were done to study the effect of these approximations at Jefferson Lab kinematics and they change the extracted CFF coefficient Im($\mathcal{C}^I$) by about 20%, which is larger than the size of the combined statistical and systematic error bar, as shown on Figure 51 [69]. The good news is however that the Q^2 lever arm being so small and x_B remaining the same, the same 20% increase in $\mathcal{C}^I$ applies for all three Q^2 settings and the conclusion on the handbag dominance remains.

Turning to newer results on DVCS asymmetries from CLAS described in section III D, we reach the same conclusions as for the older CLAS results already commented in this section : the $\sin\phi$ contribution seems to dominate the asymmetry everywhere, even though a sizeable contribution from $\cos\phi$ has been observed at high t, most likely coming from the Bethe-Heitler, but this asymmetry analysis does not allow one to disentangle the different contributions entering this observable. These data do not add much to the discussion about scaling, besides comforting the older CLAS asymmetry results on the matter. Even though the kinematical range and statistics allow a thinner binning than for the old experiment, the range in Q^2 at fixed x_B is very limited because of the beam energy limitation. Moreover, to have enough statistics, the data have to be binned into rather large x_B, t and Q^2 bins,

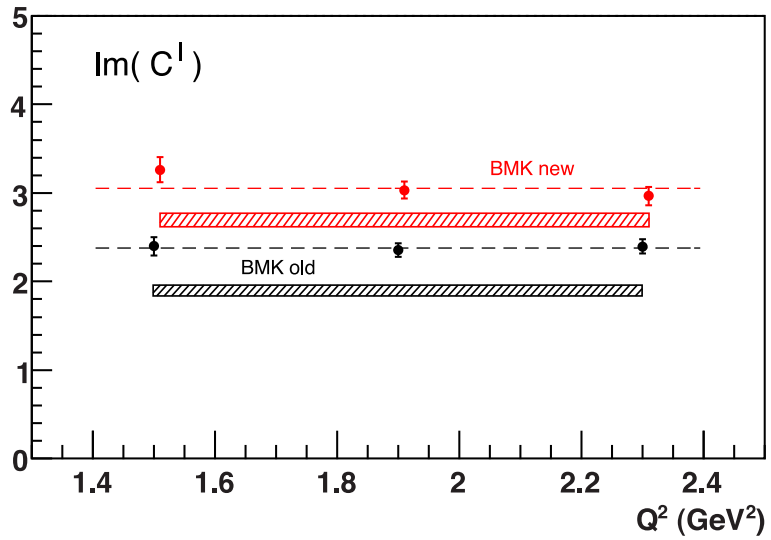

FIG. 51: Effect of the BMK hotfix described in [20] on the $\sin\phi$ coefficient $\mathrm{Im}(\mathcal{C}^I)$ as measured by the Jefferson Lab Hall A E00-110 experiment. The shaded bands represent the systematic error. The dashed lines represent the coefficient averaged over the three Q^2 bins.

which makes it even more difficult when trying to study Q^2 dependences as the rest remains fixed, similarly to the Hall A experiment.

Overall, it appears that for observables particularily sensitive to the imaginary part of the interference term between DVCS and BH, the handbag contribution seems dominant. However, as long as the Q^2 dependence of the various extracted coefficients are not studied with a larger lever arm in Q^2 than the Hall A experiment, some reasonable doubt will remain with respect to this. As for the contribution of the handbag diagram to the unpolarized DVCS cross section, there is absolutely no proof whatsoever that it is dominant and that a leading twist analysis of this observable would allow for a reliable extraction of integrals of GPDs. Future experiments in Hall A and B are planned (see Refs. [22, 70] and section IV) and will give some very interesting inputs to that long-standing problem.

B. Can we reliably extract Generalized Parton Distributions from 6 GeV data?

Generalized Parton Distributions are complicated functions of $(x, \xi, t; Q^2)$ where only the Q^2 dependence is governed by a set of evolution equations known to NLO and be-

yond [17, 18]. In addition, GPDs enter the at Leading Order DVCS amplitude through the so-called Compton Form Factors, which are integrals in x of the GPDs weighted by the quark propagators. Consequently, extracting GPDs from data is a much more involved task than extracting parton densities from inclusive Deep Inelastic Scattering experiments. As described in section II, there is however much more contraints to GPDs than to PDFs :

- In the forward limit of $\xi = t = 0$, H and $\widetilde{H}$ reduce to the usual polarized and unpolarized PDFs, which are very well known from years of DIS experiments in a wide kinematic range.
- The x-integral of the GPDs give their Form Factor counterparts.
- The x^n-moments or Mellin moments of the GPDs are polynomials in ξ of order $n+1$, which is a consequence of Lorentz invariance.
- The terms with highest power ξ^{n+1} are equal and opposite for H and E and they lead to the so-called D-term.
- There are some positivity constraints to GPDs at Leading Order of α_S but they are always ignored so far because they mix various GPDs in a non-trivial way [71, 72] and they are therefore difficult to incorporate into parametrizations. Moreover, at Next-to-Leading Order, the positivity constraint is dependent on the factorization scheme.

In addition, due to the interference between Bethe-Heitler and DVCS, it is possible to gain information on DVCS at the amplitude level. For instance, the imaginary part of the interference term itself is simply the BH amplitude multiplied by the imaginary part of the DVCS amplitude, which selects the GPDs at the particular line $x = \xi$ instead of the full x-integral of the GPDs. Most of the low-energy information available from Jefferson Lab (or HERMES) concerns the imaginary part of the DVCS amplitude, since it is very likely, as we stated in the last section, that the leading-twist amplitude dominates the imaginary part of the interference, and that we can indeed extract some information about GPDs from asymmetry or cross section difference observables. The asymmetry also contains the unpolarized cross section in the denominator, which complicates the analysis with respect to the cross section difference.

There are in principle two ways to extract GPD information from data :

- If one is in a kinematical regime where the BMK formalism and its approximations is valid (large Q^2), there is a one-to-one correspondance between the extracted $\sin\phi$ moment of the cross section difference and the imaginary part of a linear combination of CFF contained in the $s^I_{1,unp}$ as written in Eq. 23. It is the method used in the Hall A paper [47]. However, as explained before, the Hall A experiment has Q^2 values way too low in order to apply the BMK formalism, leading to errors of the order 20%. HERMES or CLAS has some data at larger Q^2 but they only measure asymmetries, for which that analysis may only be done with other approximations which lead to systematic errors of the same size. It seems unlikely that we will be able to use that method in a precise and reliable way in the near future. Even after the Jefferson Lab upgrade, Q^2 will not be high enough. However there have been recent attempts to do so [23, 24] using theoretical tools with less approximations than BMK [73] but again, it required other (non-kinematical) approximations which lead to large systematic errors. Moreover, these methods used "local fit", meaning that the fits are performed separately for each kinematic point the experiences published. The results would then need to be compared to models anyway so that they can be used in other kinematic regions, which will be needed when trying to draw conclusions on the nucleon structure.

- If one has a parametrized GPD model, a fit to data will give information about the GPDs. The clear advantage of this method is that a global fit with all the available data on exclusive processes accessing GPDs could be used in order to constrain the fit. This fit would give parametrized GPDs and one would be able to directly derive Ji's sum rule and tomographic pictures of the nucleon for instance. The important drawback is that it would be partly model dependent, which would show up when extrapolations to unexplored kinematical domains would be needed. This method is similar to the extraction of PDFs from DIS data. The use of different assumptions for PDF parametrization offers a way to estimate the systematic errors. This may prove more difficult for GPDs since their parametrization is much more constrained.

It is clear that, similarly to the PDF extraction case, only a global fit will yield the necessary information about GPDs in order to uncover the three dimensional structure of the nucleon, as advertised by experimentalists for 10 years. Theorists have barely started working on models which may be used for global fitting. The Dual Model described in section

II D 2 was used in a few articles trying to understand the experimental data [24, 39, 74]. A more complicated model based on the Mellin-Barnes representation [25, 34, 35] seems more promising even though the authors admit that a lot of work is still required.

We will describe in the following a few findings concerning models and available data which help in understanding the current status of GPD phenomenology.

1. Data versus Double Distribution and minimalist Dual models

These first two classes of model have been used in order to compare with data, rather than to fit data. The Double Distribution model, described in section II D 1 has a few parameters but they have a relatively small influence on the main features of data. We used the classic VGG Double Distribution model [36] for the comparison. The minimalist dual model, described in section II D 2, only retains the forward generating function $Q_0(x,t)$ in order to gain a parameter-free description of the data. Of course, it also means that it will lack all the genuine non-forward effects since only the knowledge of the standard PDFs is required to build such a model.

The comparison of the polarized cross section data from Hall A E00-110 and the CLAS asymmetries with both models is shown on Figure 52, which has been adapted from Polyakov and Vanderhaeghen's unpublished study [74].

As stated in the experimental section of this document, the VGG model tends to overestimate all these observables by 20 to 30% whereas the minimalist dual model does an impressive work at reproducing the polarized cross section data from Hall A but clearly does not do such a good job for asymmetries. As expected, when compared with the Hall A unpolarized cross section data, the minimalist dual model is off by up to 30% where the BH contribution is the smallest compared to DVCS ($\phi = 180°$), showing that the unpolarized cross section requires a lot more than the simplistic forward generating function $Q_0(x,t)$. I would like to stress that this last conclusion would not have been possible without at least one collaboration trying to measure cross sections rather than asymmetries. Even though the difficulty in the design and analysis of cross section experiments is tremendous compared to asymmetries, the fact that all the information is mixed up in the asymmetry, with an obvious non-trivial denominator, speaks obviously in favor of measuring cross sections.

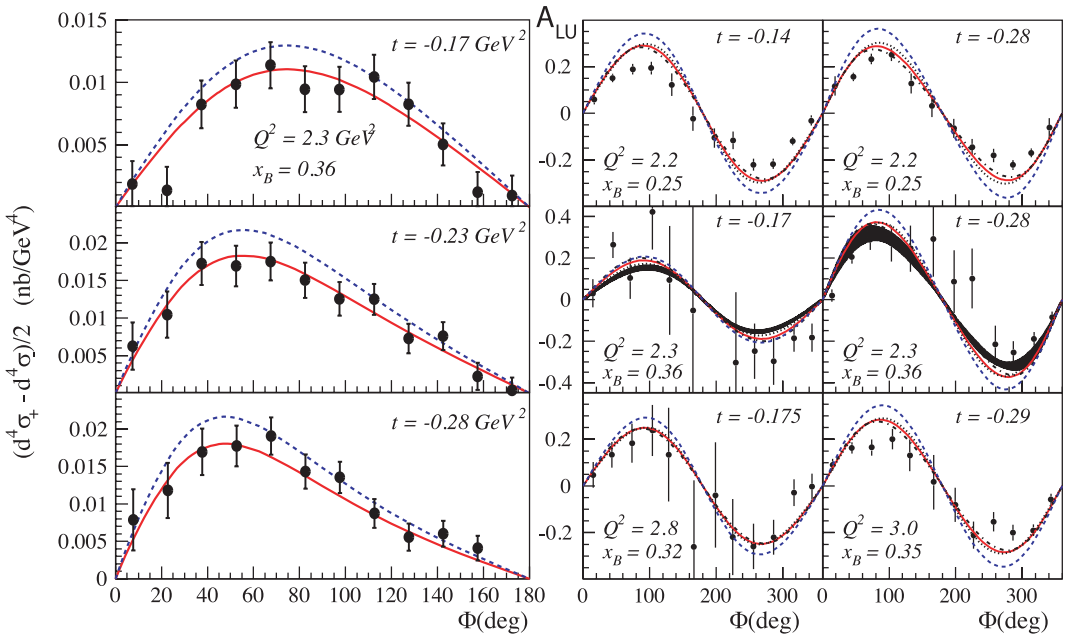

FIG. 52: (Left) Hall A data on the difference of cross sections for opposite electron helicities with the standard VGG model [36] (blue dashed line) and the minimalist dual model [74] (red line). (Right) CLAS data on the Beam Spin Asymmetry with the same models. The Hall A data turned into asymmetries for the middle two bins have been represented as black bands and show perfect compatibility with the CLAS data.

2. *Data versus local fits*

There has been recent efforts to try and gain model-independent information about Compton Form Factors. Moutarde in Ref. [24] tried to fit the Hall A and CLAS data assuming only the GPD H contributes. Guidal did the same effort but with no assumption on the dominance of a certain GPD [23]. In both cases, the fit is local, which means that each experimental kinematic point has its own fitting procedure and the result is an estimation of CFF at that particular kinematics with no link to the others. These evaluations of the CFF can only be compared to models if one wants to gain insights on the structure of the nucleon, since the interesting features of the GPD lie in their (x, ξ, t) dependence. Figure 53 shows examples of such local fits from Moutarde and the extracted values for Im($\mathcal{H}$) and Re($\mathcal{H}$). The results from Guidal are compatible but exhibit much larger error bars as a

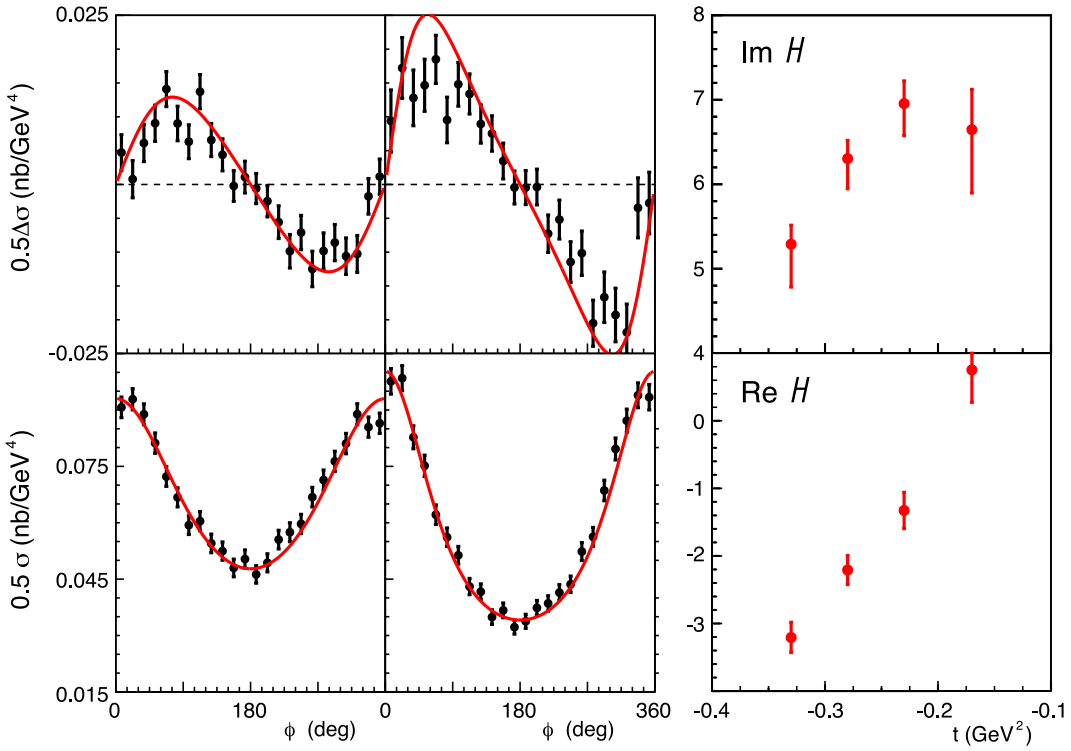

FIG. 53: (Left 4 plots) Hall A E00-110 data on photon electroproduction cross section difference for opposite electron helicities for two t bins (top) and unpolarized cross section for the same t bins (bottom) along with Moutarde local fit in red. (Right 2 plots) Results of the local fit for the imaginary part (top) and real part(bottom) of the CFF $\mathcal{H}$. Figure adapted from Ref. [24].

consequence of fitting more CFFs at the same time. It is obviously a major drawback from such local fits: unless different experiments have exactly the same kinematics *and* the same bin size in all variables, only one observable can be fit at a time and fitting more than one CFF seems tricky.

3. Data versus global fits

Two groups have made attempts to perform global fits with a GPD parametrization. Moutarde in Ref. [24] used a dual model approach with a simple 2-parameter form for the Generalized Form Factors $B_{nl}(t)$ (see section II D 2 for definitions) and truncated the infinite series at 4 Gegenbauer polynomials at most, which corresponds to a maximum of 28 free

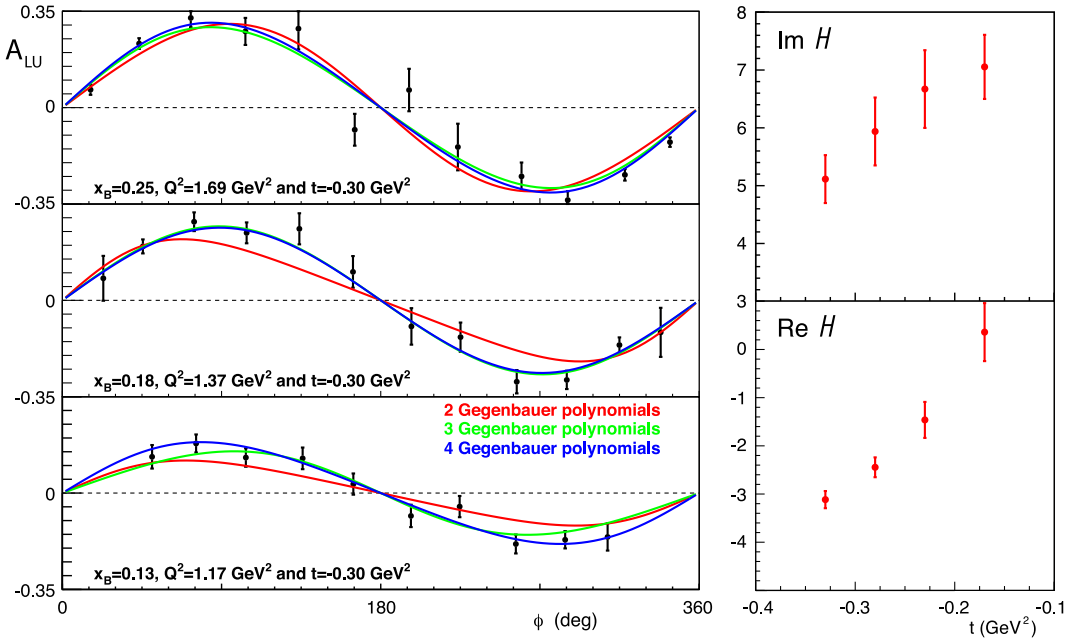

FIG. 54: (Left 3 plots) CLAS Beam Spin Asymmetry data on photon electroproduction for three bins along with Moutarde global fits with 2, 3 or 4 Gegenbauer polynomials. (Right 2 plots) Results of the global fit for the imaginary part (top) and real part(bottom) of the CFF $\mathcal{H}$. Figure adapted from Ref. [24].

parameters to describe all the $B_{nl}(t)$. The CLAS asymmetries are used in Figure 54 to illustrate the quality of the fit depending on the number of Gegenbauer polynomials. Note that all published Jefferson Lab Hall A and CLAS (except for high-($|t|/Q^2$) or high-x_B) data described in this document are used in this fit, and that the fit assumes that only the GPD H contributes to these observables.

Kumericki and Mueller [25] model GPDs in a rather elaborate way, using a conformal SL(2,$\mathbf{R}$) partial wave expansion, written as a Mellin-Barnes integral [75]. The precise description of this involved fit procedure is beyond the scope of this document. However, the Mueller group seems to be especially advanced in terms of creating a proper fitting procedure to the DVCS data and extracting twist-2 GPD information. The result of their fit can be seen on Figure 55, for which the sea parameters are fixed by small-x_B fits to HERA data, but probably have little influence in the valence region. Similarly to Moutarde's fit, the main version of this procedure is done with the hypothesis that the GPD H is dominant

(green symbols and curves in Fig. 55). It is clearly satisfactory for HERMES, CLAS and the polarized Hall A cross section, but misses the Hall A unpolarized cross section data by a large amount, especially around $\phi = 180°$, similarly to the minimalist dual model we presented before. In order to be able to fit the Hall A total cross section, Mueller and Kumericki had to add the GPD $\widetilde{H}$, which tends to take rather large values (blue symbols and curves in Fig. 55). This was also a conclusion from a recent paper [76] which tried to fit the HERMES data sensitive to $\widetilde{H}$, that this GPD is usually largely under-estimated by models (VGG for instance). Note that it is counter-intuitive with the fact that at small-t, $\widetilde{H}$ should be close to a polarized PDF and take small values (smaller than the corresponding unpolarized PDF or H in any case because of the positivity argument). A large caveat from all these fitting procedures are that they heavily rely on a twist-2 dominance: if large twist-3 contribution comes into play, which might very well be the case for the total cross section, these conclusions might be quite different.

C. Did we gain insights on how to best measure DVCS experimentally?

Even though the current status of GPD extraction from experimental data is far from satisfactory, there is little doubt that theorists will find the right fitting procedure shortly. They will be able to give us a very much needed piece of information: what type of observable should be measured and with what accuracy in order to extract GPDs within some systematic and statistical errors, and what would be the outcome in terms of our knowledge of the 3D-structure of the nucleon. It is obvious that more accurate data in a larger kinematical range will be needed in the near future to feed these new fitting procedures. Let us recall that it took nearly 40 years of deep inelastic electron scattering, from the early SLAC experiments to the last electron proton collisions at HERA to have a thorough understanding of the parton densities in a large enough range of x_B and Q^2. During that time, a significant fraction of QCD theorists were at work, trying to explain, interpret, and finally fit the data up to NNLO accuracy. Even after all these years of data taking, there is still work to be done in the high-x_B region and, using semi-inclusive deep inelastic scattering, trying to finally reach a good understanding of the influence of the strange quark in the nucleon partonic structure, not to mention the gluon contribution to the nucleon spin. Considering that the GPD are at least an order of magnitude more complicated than PDFs,

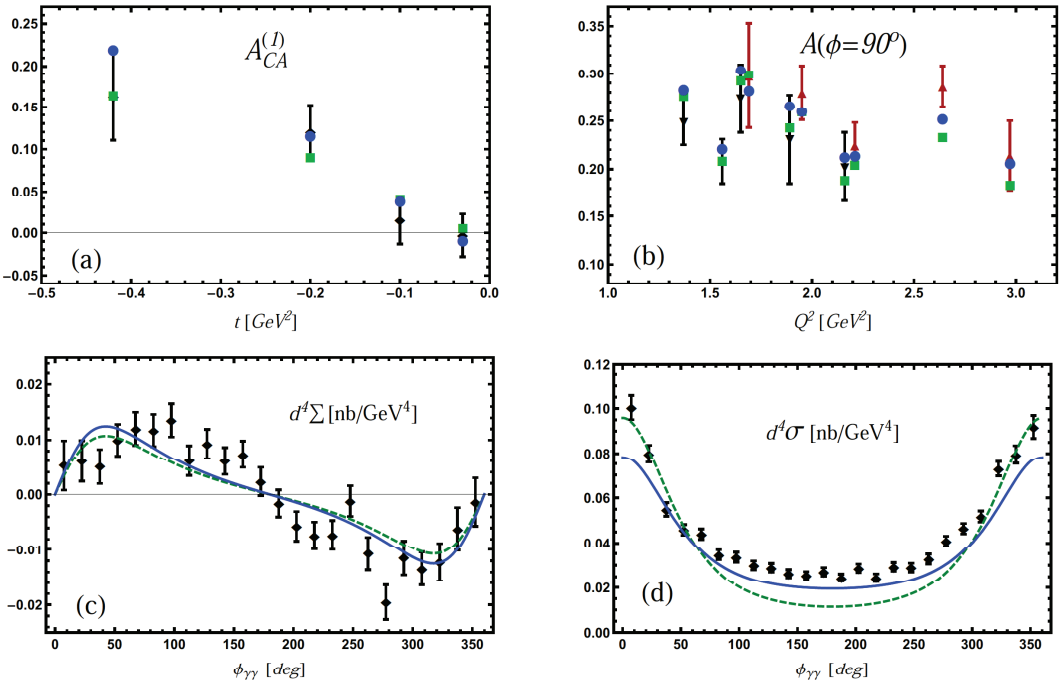

FIG. 55: World data in the valence region from HERMES, CLAS and Hall A versus Mueller and Kumericki's GPD fit. In all plots, the green squares or dashed line represents a fit to the valence parameters of the fit using CLAS and HERMES data alone, whereas the blue circles or solid lines represent a fit including the Hall A data, both unpolarized and polarized cross sections. The top left quadrant shows HERMES Beam Charge Asymmetry as black diamonds. The top right quadrant shows the CLAS BSA at $\phi = 90°$ for two different t bins as black and red triangles. The bottom left quadrant shows the Hall A difference of cross sections for opposite electron helicity as black diamonds. Finally, the bottom right quadrant shows the Hall A total cross section as black diamonds as well. Figure from [25].

both theory-wise and experimentally, we still have a long road ahead of us before we are satisfied with our findings on GPDs and finally obtain tomographic images of the nucleon at all longitudinal momentum fractions.

Since many more Deep Exclusive experiments will be designed in the future, it is important to check whether some feedback from the few first experiments may help the next ones. Here follows a non-exhaustive list of findings and thoughts on this matter:

- One of the main difficulties of performing DVCS measurements is the low cross section.

In order to have a reasonable counting rate in the detectors, one has to do one or both of the following: have a large luminosity and/or have a large detector acceptance. The luminosity is often an accelerator parameter, considering the target size may be limited depending on its type, polarized or not. This clearly advantages Jefferson Lab since DVCS experiments with luminosities up to $10^{37}\text{cm}^{-2}\text{s}^{-1}$ have already run successfully. Detectors with large acceptances have also been used, in Jefferson Lab with CLAS and elsewhere, but with luminosities limited to a few $10^{34}\text{cm}^{-2}\text{s}^{-1}$ in the case of CLAS. The next generation 12-GeV experiments at Jefferson Lab have the same parameters, with an upgraded CLAS12 detector allowing for luminosities to reach $10^{35}\text{cm}^{-2}\text{s}^{-1}$.

- The polarized cross section and the beam spin asymmetries seem rather well parametrized or even modelled already, as seen in the previous section. However, the fact that the minimalist dual model with no genuine non-forward contribution reproduces the Hall A polarized cross section data so well also means that the bulk of it is somewhat "trivial" : it is simply explained using only PDFs. Assuming the genuine non-forward contribution to this observable is about 10%, it will require even more accurate data in order to gain some new information about the proton structure. This remark is also true for the total cross section for a completely different reason : since experimentally we measure the coherent sum of DVCS and Bethe-Heitler, and that the $|\text{BH}|^2$ dominates the cross section (especially at ϕ close to 0) and needs to be subtracted, the interesting part of the total cross section is much smaller and again, requires a very good accuracy to be effectively analyzed in terms of GPDs since it contains many contributions (interference and $|\text{DVCS}|^2$, twist-2 and up). This need for excellent data accuracy amplifies the necessity to use facilities and detectors with high luminosity and/or high acceptance.

- Deeply Virtual Compton Scattering and photon electroproduction in general is an exclusive process with a three-particle final state. As said above, the measurement accuracy is critical in order to extract reliable information on GPDs. The ability of experimentalists to extract exclusive final states is therefore of the utmost importance: if the exclusivity is average and many π^0 electroproduction events sneak in the data sample, large corrections will be needed and increase the systematic error. For instance, exclusivity has been achieved in the CLAS asymmetry measurements

(described in section III D) by requiring a complete three-particle final state, but it is unfortunately not enough since the detector is not hermetic : A set of exclusivity cuts requiring the kinematic completeness of the photon electroproduction process are imposed to the data. Even then, the resulting missing energy is wide enough to allow extra photons or pions to contaminate the data sample : A π^0 subtraction procedure was necessary, and induced the largest contribution to the systematic error. When designing new experiments, it will be necessary to limit the contamination of our data sample in order to reduce this systematic uncertainty. This can be done by having a more hermetic detector, but somewhat more easily, by improving the resolution of the detectors.

- The total cross section measured by Hall A is a challenge to many groups who try to fit the data. It is however not surprising since all fits use severe restrictions such as twist-2 and H dominances. It is absolutely necessary to have more *accurate* cross section data in a larger kinematic range in order to help theorists understand the content of this observable and force them to go beyond their simple assumptions and fit these data with hopefully more successful procedures. Fortunately, CLAS will hopefully release cross section data soon, and a new Hall A experiment is taking data in the fall of 2010 [22]. Even more cross section data are expected after the Jefferson Lab 12 GeV upgrade.

- Almost all measurements done so far at Jefferson Lab were especially sensitive to the GPDs H and $\widetilde{H}$, with the exception of the neutron DVCS experiment in Hall A. These two GPDs are easier to access but also easier to parametrize since they reduce in the forward case to the usual parton densities q and Δq. However, it is especially important to gain knowledge in the GPD E since it enters on equal footings as H in Ji's sum rule (see Eq. 7). Moreover, it is often the magnetic and electric combinations of H and E which come out of GPD models. The best way to access E is through transversely polarized target measurements, and we described in section III E a 6 GeV proposal with CLAS in Hall B which proposes to measure observables sensitive to E.

- We have not given many details about radiative corrections so far but they are approximated in the current analysis of photon electroproduction. Depending on the exclusivity of the event, the radiative corrections may have a large impact in cross

section observables (not as much on asymmetries since they cancel to first order). In order to reduce the potential systematic error induced by an approximate treatment of such corrections, it seems important to work out the most adequate way of including radiative corrections in the experimental analysis.

VI. CONCLUSION AND OUTLOOK

This document is by no means an exhaustive review of Deeply Virtual Compton Scattering experiments worldwide. I purposely focused on the experiments I either promoted (the initial 6 GeV Hall A program, the 6 GeV transverse target and the 12 GeV proposals in Hall B) or actively participated in (the 6 GeV unpolarized target program in Hall B). In all cases, this physics program would not have been possible without the active collaborations supporting these studies in Halls A and B and my theory colleagues for their invaluable guidance. With all this help, we managed to design successful experiments which pioneered the study of Generalized Parton Distributions through DVCS measurements. For a first set of experiments, the conclusions are impressive: we are confident that the imaginary part of the DVCS amplitude is dominated by the handbag diagram already at 6 GeV, and that we therefore measured for the first time linear combinations of GPDs at $x = \xi$. We made accurate measurements in a large kinematical range which constrain models and constitute the starting point for theorists to build the most adequate fitting procedures needed to unravel the 3D structure of the nucleon. These last 10 years of experimental and theory scrutiny have been extremely productive. This can be compared to the time it took for the study of nucleon structure through parton densities to take off and yield accurate and stable results.

The next phase of experiments will be decisive: with the help of higher energy at Jefferson Lab, experiments in Halls A and B will give even more accurate results in a larger kinematical domain. New observables will also be measured using transversely polarized target experiments at 6 GeV and surely at 11 GeV, which will be yet another set of constraints to GPD models and parametrizations. I would like to mention that Deeply Virtual Compton Scattering, even if it is without a doubt the most convenient process to study GPDs at low energy due to a likely early scaling situation similar to the DIS case, is definitely not the only process sensitive to GPDs. Indeed, the electroproduction of mesons in the deep virtual regime (DVMP) can be factorized into a hard scattering kernel and the non-perturbative content of the nucleon parametrized by GPDs, similarly to DVCS. However, scaling for DVMP is expected at larger Q^2 and so far, data are not in agreement with GPD models at low energy [77–79]. Similar data with higher beam energy will be of particular interest, especially if the handbag diagram contribution becomes sizeable and can be isolated. It is

worth mentionning that in a similar time frame as JLab12, COMPASS-II will take DVCS and DVMP data using a 160 GeV naturally polarized muon beam on a hydrogen target and reach x_B values down to 10^{-2} with Q^2 up to 10 GeV^2 or so. Their range in x_B, complementary to CLAS12, will allow one to gain information on the sea quark GPDs through the measurement of mixed beam charge and spin asymetries or cross section differences.

As mentioned in the introduction, DVCS is only sensitive to chiral-even GPDs but another set of four chiral-odd GPDs exist, also known as transversity GPDs. These GPDs can be linked to the transversity quark distributions usually measured in semi inclusive DIS, which opens yet another way of studying the nucleon structure [80]. The photoproduction of $\pi\rho_T$ pairs at large invariant mass is sensitive to the transversity GPDs [81] and this type of measurement can surely be performed with Jefferson Lab at 12 GeV.

Finally, for the long term future (2020-2030+), the hadronic physics community has decided to start working on the design of an electron-ion collider called EIC in its US version [82] or ENC in its EU version [83]. As far as hard exclusive processes are concerned, these projects will open up the available kinematics thanks to the collision kinematics, allowing to reach much higher Q^2 and lower x_B. It is still unclear if these colliders (especially their low luminosity versions) will allow one to make statistically relevant measurements of such exclusive processes and what type of constraints they can bring to GPDs. This is the subject of future studies I plan to be working on in the near future [84].

[1] M. Breidenbach et al., Phys. Rev. Lett. **23**, 935 (1969).

[2] K. Abe et al. (E154), Phys. Lett. **B405**, 180 (1997), arXiv:hep-ph/9705344.

[3] A. V. Radyushkin, Phys. Rev. **D58**, 114008 (1998), arXiv:hep-ph/9803316.

[4] M. Diehl, T. Feldmann, R. Jakob, and P. Kroll, Phys. Lett. **B460**, 204 (1999), arXiv:hep-ph/9903268.

[5] D. Mueller, D. Robaschik, B. Geyer, F. M. Dittes, and J. Horejsi, Fortschr. Phys. **42**, 101 (1994), hep-ph/9812448.

[6] X.-D. Ji, Phys. Rev. **D55**, 7114 (1997), hep-ph/9609381.

[7] X.-D. Ji, Phys. Rev. Lett. **78**, 610 (1997), hep-ph/9603249.

[8] A. V. Radyushkin, Phys. Lett. **B380**, 417 (1996), hep-ph/9604317.

[9] A. V. Radyushkin, Phys. Rev. **D56**, 5524 (1997), hep-ph/9704207.

[10] P. Bertin, C. Hyde-Wright, R. Ransome, F. Sabatié, et al. (Jefferson Lab Hall A), JLab Experiment E00-110 (2000).

[11] P. Bertin, C. Hyde-Wright, F. Sabatié, E. Voutier, et al. (Jefferson Lab Hall A), JLab Experiment E03-116 (2003).

[12] V. Burkert, L. Elouadrhiri, M. Garçon, S. Stepanyan, et al. (CLAS), JLab Experiment E01-113 (2001).

[13] A. Biselli, L. Elouadrhiri, K. Joo, S. Niccolai, et al. (CLAS), JLab Experiment E05-114 (2005).

[14] H. Avakian, M. Guidal, R. Kaiser, F. Sabatié, et al. (CLAS), JLab Experiment E08-021 (2008).

[15] A. Biselli, H. Egiyan, L. Elouadrhiri, M. Holtrop, D. Ireland, W. Kim, F. Sabatié, et al. (CLAS12), JLab Experiment E12-06-119 (2006).

[16] X.-D. Ji, W. Melnitchouk, and X. Song, Phys. Rev. **D56**, 5511 (1997), arXiv:hep-ph/9702379.

[17] D. Mueller, Phys. Lett. **B634**, 227 (2006), arXiv:hep-ph/0510109.

[18] K. Kumericki, D. Mueller, K. Passek-Kumericki, and A. Schafer, Phys. Lett. **B648**, 186 (2007), arXiv:hep-ph/0605237.

[19] A. V. Belitsky, D. Mueller, and A. Kirchner, Nucl. Phys. **B629**, 323 (2002), hep-ph/0112108.

[20] A. V. Belitsky and D. Mueller, Phys. Rev. **D79**, 014017 (2009), arXiv:0809.2890[hep-ph].

[21] A. V. Belitsky and D. Mueller, Phys. Rev. **D82**, 074010 (2010), arXiv:1005.5209[hep-ph].

[22] P. Bertin, C. Hyde, C. Munoz Camacho, J. Roche, et al. (Jefferson Lab Hall A), JLab Experiment E07-007 (2010).

[23] M. Guidal, Eur. Phys. J. **A37**, 319 (2008), arXiv:0807.2355[hep-ph].

[24] H. Moutarde, Phys. Rev. D **79**, 094021 (2009), arXiv:0904.1648[hep-ph].

[25] K. Kumericki and D. Mueller, Nucl. Phys. **B841**, 1 (2010), arXiv:0904.0458[hep-ph].

[26] M. Burkardt, Phys. Rev. **D62**, 071503 (2000), arXiv:hep-ph/0005108.

[27] J. P. Ralston and B. Pire, Phys. Rev. **D66**, 111501 (2002), hep-ph/0110075.

[28] M. Burkardt, Int. J. Mod. Phys. **A18**, 173 (2003), hep-ph/0207047.

[29] M. Diehl, Eur. Phys. J. **C25**, 223 (2002), arXiv:hep-ph/0205208.

[30] A. V. Belitsky, X.-d. Ji, and F. Yuan, Phys. Rev. **D69**, 074014 (2004), arXiv:hep-ph/0307383.

[31] M. Gockeler et al. (QCDSF), Phys. Rev. Lett. **98**, 222001 (2007), arXiv:hep-lat/0612032.

[32] V. Y. Petrov et al., Phys. Rev. **D57**, 4325 (1998), arXiv:hep-ph/9710270.

[33] M. Penttinen, M. V. Polyakov, and K. Goeke, Phys. Rev. **D62**, 014024 (2000), arXiv:hep-ph/9909489.

[34] K. Kumericki, D. Mueller, and K. Passek-Kumericki, Nucl. Phys. **B794**, 244 (2008), arXiv:hep-ph/0703179.

[35] K. Kumericki and D. Mueller (2010), arXiv:1008.2762[hep-ph].

[36] K. Goeke, M. V. Polyakov, and M. Vanderhaeghen, Prog. Part. Nucl. Phys. **47**, 401 (2001), hep-ph/0106012.

[37] M. V. Polyakov and A. G. Shuvaev (2002), arXiv:hep-ph/0207153.

[38] M. Diehl and D. Y. Ivanov (2007), arXiv:0712.3533[hep-ph].

[39] V. Guzey and T. Teckentrup, Phys. Rev. **D74**, 054027 (2006), arXiv:hep-ph/0607099.

[40] M. V. Polyakov, Phys. Lett. **B659**, 542 (2008), arXiv:0707.2509[hep-ph].

[41] S. Stepanyan et al. (CLAS), Phys. Rev. Lett. **87**, 182002 (2001), hep-ex/0107043.

[42] M. Diehl, T. Gousset, B. Pire, and J. P. Ralston, Phys. Lett. **B411**, 193 (1997), hep-ph/9706344.

[43] D. Lachartre and F. Feinstein, Nucl. Instrum. Meth. **A442**, 99 (2000).

[44] F. Druillole et al. (ANTARES), IEEE Trans. Nucl. Sci. **49**, 1122 (2002).

[45] L. W. Mo and Y.-S. Tsai, Rev. Mod. Phys. **41**, 205 (1969).

[46] W. M. Yao et al. (Particle Data Group), J. Phys. **G33**, 1 (2006).

[47] C. Munoz Camacho et al. (Jefferson Lab Hall A), Phys. Rev. Lett. **97**, 262002 (2006), arXiv:nucl-ex/0607029.

[48] E. R. Berger, F. Cano, M. Diehl, and B. Pire, Phys. Rev. Lett. **87**, 142302 (2001), arXiv:hep-ph/0106192.

[49] F. Cano and B. Pire, Eur. Phys. J. **A19**, 423 (2004), arXiv:hep-ph/0307231.

[50] S. Ahmad, H. Honkanen, S. Liuti, and S. K. Taneja, Eur. Phys. J. **C63**, 407 (2009), arXiv:0708.0268[hep-ph].

[51] F. Ellinghaus, W. D. Nowak, A. V. Vinnikov, and Z. Ye, Eur. Phys. J. **C46**, 729 (2006), arXiv:hep-ph/0506264.

[52] M. Gockeler et al. (QCDSF), Phys. Rev. Lett. **92**, 042002 (2004), arXiv:hep-ph/0304249.

[53] P. Hagler et al. (LHPC), Phys. Rev. **D77**, 094502 (2008), arXiv:0705.4295[hep-lat].

[54] F. X. Girod et al. (CLAS), Phys. Rev. Lett. **100**, 162002 (2008), arXiv:0711.4805[hep-ex].

[55] R. De Masi et al. (CLAS), Phys. Rev. **C77**, 042201 (2008), arXiv:0711.4736[hep-ex].

[56] J. M. Laget, Phys. Rev. **C76**, 052201 (2007), arXiv:0708.1250[hep-ph].

[57] M. Vanderhaeghen, P. A. M. Guichon, and M. Guidal, Phys. Rev. **D60**, 094017 (1999), hep-ph/9905372.

[58] A. V. Belitsky and D. Mueller, Phys. Lett. **B513**, 349 (2001), arXiv:hep-ph/0105046.

[59] K. Abe et al. (E143), Phys. Rev. **D58**, 112003 (1998), arXiv:hep-ph/9802357.

[60] F. Klein, A. Sandorfi, et al. (CLAS), JLab Experiment E06-101 (2006).

[61] S. Aune et al., Nucl. Instrum. Meth. **A604**, 53 (2009).

[62] H. Avakian, clas12DVCS computer program for DVCS/BH and single π^0 event simulations, unpublished (2005).

[63] M. Vanderhaeghen, M. Guidal, P. Guichon, and L. Mossé, Computer Codes for DVCS and BH Calculations, Private Communications (2006).

[64] S. Chen, H. Avakian, V. Burkert, and P. Eugenio (the CLAS) (2006), hep-ex/0605012.

[65] J. Pumplin et al., JHEP **07**, 012 (2002), hep-ph/0201195.

[66] A. D. Martin, R. G. Roberts, W. J. Stirling, and R. S. Thorne, Eur. Phys. J. **C28**, 455 (2003), hep-ph/0211080.

[67] S. Chekanov et al. (ZEUS), Eur. Phys. J. **C21**, 443 (2001), arXiv:hep-ex/0105090.

[68] M. Diehl, Phys. Rept. **388**, 41 (2003), hep-ph/0307382.

[69] C. Munoz Camacho, Estimation of the effect of the BMK hotfix, unpublished (2008).

[70] J. Roche, B. Michel, C. Munoz Camacho, C. Hyde, et al. (Jefferson Lab Hall A), JLab Experiment E12-06-114 (2006).

[71] B. Pire, J. Soffer, and O. Teryaev, Eur. Phys. J. **C8**, 103 (1999), arXiv:hep-ph/9804284.

[72] P. V. Pobylitsa, Phys. Rev. **D65**, 114015 (2002), arXiv:hep-ph/0201030.

[73] P. Guichon and M. Vanderhaeghen, Analytic $ee'\gamma$ cross section, private communication (2008).

[74] M. V. Polyakov and M. Vanderhaeghen (2008), arXiv:0803.1271[hep-ph].

[75] D. Mueller and A. Schafer, Nucl. Phys. **B739**, 1 (2006), arXiv:hep-ph/0509204.

[76] M. Guidal, Phys. Lett. **B693**, 17 (2010), arXiv:1005.4922[hep-ph].

[77] L. Morand et al. (CLAS), Eur. Phys. J. **A24**, 445 (2005), arXiv:hep-ex/0504057.

[78] S. A. Morrow et al. (CLAS), Eur. Phys. J. **A39**, 5 (2009), arXiv:0807.3834[hep-ex].

[79] J. P. Santoro et al. (CLAS), Phys. Rev. **C78**, 025210 (2008), arXiv:0803.3537[nucl-ex].

[80] M. Anselmino et al., Phys. Rev. **D75**, 054032 (2007), arXiv:hep-ph/0701006.

[81] M. E. Beiyad, B. Pire, M. Segond, L. Szymanowski, and S. Wallon, Phys. Lett. **B688**, 154 (2010), arXiv:1001.4491[hep-ph].

[82] A. Deshpande (EIC), Nucl. Phys. **A827**, 618c (2009).

[83] D. von Harrach, V. Metag, and A. Schaefer, Nucl. Phys. **A622**, 46c (1997).

[84] H. Moutarde, F. Sabatié, et al., Hard Exclusive Processes with Electron Ion or Electron Nucleus Colliders, work in progress (2010-2011).